Dissertation

Highly-Efficient Nonlinear µFE Modelling of Bones and Bone-Screw Systems

carried out for the purpose of obtaining the degree Doctor of technicae (Dr. techn.), submitted at TU Wien, Faculty of Mechanical and Industrial Engineering, by

Dipl.-Ing. Pia Stefanek, BSc.

Mat.Nr.: 00808550

under the supervision of

Univ. Prof. Dipl.-Ing. Dr. techn. Dieter H. Pahr

Institute of Lightweight Design and Structural Biomechanics, E317

Vienna, March 2025

reviewed by

Sen. Lect. Dr. Pinaki Bhattacharya
Insigneo Institute for In Silico Medicine
The University of Sheffield
Sheffield, UK

PD Dr. Peter Varga
AO Research Institute Davos
Davos, Switzerland

This work was not supported by any funding agency.

I confirm, that going to press of this thesis needs the confirmation of the examination committee.

Affidavit

I declare in lieu of oath, that I wrote this thesis and performed the associated research myself, using only literature cited in this volume. If text passages from
sources are used literally, they are marked as such.
I confirm that this work is original and has not been submitted elsewhere for any examination, nor is it currently under consideration for a thesis elsewhere.

I acknowledge that the submitted work will be checked electronically-technically using suitable and state-of-the-art means (plagiarism detection software). On the one
hand, this ensures that the submitted work was prepared according to the high-
quality standards within the applicable rules to ensure good scientific practice "Code
of Conduct" at the TU Wien. On the other hand, a comparison with other student
theses avoids violations of my personal copyright.

Vienna, March, 2025

_____

Pia Stefanek

Acknowledgements

First and foremost, I would like to express my deepest gratitude to my supervisors, Dieter Pahr and Alexander Synek, for their invaluable scientific expertise and continuous support throughout my research. I greatly appreciate their guidance, which has significantly contributed to this dissertation. I am especially grateful to Alexander Synek for his encouragement and mental support during difficult times.

Furthermore, I would like to sincerely thank Sebastian Bachmann for always being there to assist me with both scientific and IT-related challenges. His willingness to help and share his knowledge has been truly invaluable. I also want to extend my sincere thanks to Katja Haslinger-Vaughan, with whom I have had many insightful professional and personal exchanges. Additionally, I am grateful to all my colleagues at the institute, who have fostered a positive and motivating working atmosphere, which made my time there enjoyable and inspiring.

Finally, I would like to express my deepest appreciation to my parents, my friends, and my partner Andreas. Their unwavering support, belief in me, and encouragement during challenging times have been indispensable throughout this journey.

During the preparation of this thesis, ChatGPT was used in order to improve readability and language. All content was subsequently reviewed and edited, and the author takes full responsibility for the content of the dissertation.

Abstract

Bone fractures are a significant global health concern, necessitating research on bone mechanics, fracture healing, and effective treatment methods such as orthopedic implants. Computational modelling, particularly µFE simulations, has emerged as a powerful tool for analyzing how bone microstructures and implants behave under various loading conditions. By accurately capturing microstructural features, µFE simulations provide valuable insights into microscale deformation fields as well as stress and strain distributions. However, existing µFE solvers must balance computational efficiency with model versatility, often requiring trade-offs between speed and modelling complexity.

This dissertation focuses on advancing the specialized µFE solver ParOSol-NL to improve its predictive capabilities for bone and bone-screw systems. Four key objectives were pursued: (1) validating ParOSol-NL's accuracy at the mesoscale by comparing predicted displacement fields with experimental measurements obtained from digital volume correlation (DVC), (2) developing an efficient and accurate bone-screw contact model, (3) incorporating a pre-damage model to simulate bone damage induced by screw insertion, and (4) evaluating ParOSol-NL's accuracy in predicting bone-screw pull-out forces by comparison to experimental data.

For mesoscale validation, ParOSol-NL's predicted displacement fields were compared to DVC measured displacement fields of human trabecular bone biopsies under compressive loading, demonstrating strong agreement in both the elastic regime as well as at the ultimate load step. To model bone-screw interactions, various simplified interfaces were compared against the general contact algorithm of the commercial FE solver Abaqus/Explicit. Various single-screw bone constructs loaded in pull-out, push-in and shear served as test cases. Using a simplified contact algorithm based on tensionally strained interface element deletion (TED) allowed to predict whole-construct stiffness efficiently yet accurately. A modified variant (TED-M) accounted for contact area changes during loading, providing more accurate maximum force predictions. Both TED and TED-M were designed for seamless integration into ParOSol-NL. Additionally, a simplified pre-damage model was implemented in ParOSol-NL, incorporating a predefined damage zone around the screw to reflect insertion-induced damage. Finally, µFE simulations incorporating both the simplified interface and pre-damage models were used to predict screw pull-out forces in porcine bone biopsies. Quantitative agreement with experimental results was only achieved when carefully integrating contact modelling, material properties, and pre-damage parameters.

This thesis enhances ParOSol-NL as a computationally efficient, nonlinear µFE simulation tool for bones and bone-screw systems. The solver's predictive accuracy at the mesoscale was validated, and simplified contact and pre-damage models were implemented to improve simulations of screw-bone interactions. These advancements enable more efficient and realistic µFE analyses, allowing for accurate biomechanical simulations while maintaining computational efficiency.

Kurzfassung

Knochenfrakturen stellen ein erhebliches globales Gesundheitsproblem dar, weshalb eine umfassende Forschung in den Bereichen Knochenbiomechanik, Frakturheilung sowie operativer Frakturversorgung mittels orthopädischer Implantate von großer Bedeutung ist. Die computergestützte Modellierung, insbesondere Mikro-Finite-Elemente-Simulationen (µFE-Simulationen), hat sich als leistungsstarkes Instrument etabliert, um das Verhalten von Knochenmikrostrukturen und Implantaten unter verschiedenen Belastungsbedingungen zu analysieren. Durch die präzise Erfassung mikrostruktureller Eigenschaften liefern µFE-Simulationen wertvolle Einblicke in Deformationsfelder sowie in die Verteilung von Spannungen und Dehnungen auf der Mikroskala. Bestehende µFE-Löser müssen jedoch eine Balance zwischen rechnerischer Effizienz und Modellkomplexität finden, was häufig einen Kompromiss zwischen Rechengeschwindigkeit und Modellierungsgenauigkeit erfordert.

Ziel dieser Dissertation ist es, den spezialisierten µFE-Löser ParOSol-NL weiterzuentwickeln, um seine Fähigkeit zur Vorhersage des Verhaltens von Knochen- und Knochen-Schrauben-Systemen zu verbessern. Hierbei wurden vier zentrale Forschungsfragen adressiert: (1) die Validierung der Modellgenauigkeit von ParOSol-NL auf der Mesoskala durch den Vergleich zu Verschiebungsfelder aus experimentellen Messungen mittels digitaler Volumenkorrelation (DVC), (2) die Entwicklung eines effizienten und präzisen Kontaktmodells zur Simulation der Knochen-Schrauben-Interaktion, (3) die Implementierung eines Vorschädigungsmodells zur Berücksichtigung von durch die Schraubeninsertion induzierten Knochenschäden sowie (4) die Bewertung der Vorhersagegenauigkeit von ParOSol-NL im Hinblick auf die maximalen Zugkräfte von Knochen-Schrauben Systemen im Vergleich zu experimentellen Daten.

Für die Validierung auf der Mesoskala wurden die durch ParOSol-NL berechneten Verschiebungsfelder mit den mittels DVC erfassten Verschiebungsfeldern humaner trabekulärer Knochenbiopsien unter Druckbelastung verglichen. Dabei zeigte sich eine hohe Übereinstimmung sowohl im elastischen Bereich als auch bei Erreichung der Maximalkraft. Um die Knochen-Schrauben-Interaktion zu simulieren, wurden verschiedene vereinfachte Kontaktmodelle mit dem allgemeinen Kontaktalgorithmus des kommerziellen FE-Lösers Abaqus/Explicit verglichen. Es wurden Knochen-Schrauben-Systeme, die jeweils aus einer einzelnen Knochenbiopsie und einer Schraube bestanden, unter Zug-, Druck- und Scherbelastung getestet. Ein vereinfachter Kontaktalgorithmus, basierend auf der Eliminierung von unter Zugspannung stehenden Elementen an der Knochen-Schraube Schnittstelle (TED), erwies sich als recheneffiziente und zugleich hinreichend genaue Methode zur Vorhersage der Gesamtsteifigkeit des Konstrukts. Eine modifizierte Variante (TED-M), die Änderungen der Kontaktfläche während der Belastung berücksichtigt, verbesserte die Genauigkeit der Maximalkraftvorhersagen. Beide Modelle, TED und TED-M, wurden speziell für die Integration in ParOSol-NL entwickelt. Weiters wurde ein vereinfachtes Vorschädigungsmodell implementiert, das eine vordefinierte geschädigte Zone um die Schraube berücksichtigt, um die durch die Insertion verursachten Knochenschäden adäquat zu erfassen. Abschließend wurden µFE-Simulationen unter Einbeziehung sowohl des vereinfachten Kontaktmodells als auch des Vorschädigungsmodells durchgeführt, um die maximalen Zugkräfte von Knochen-Schrauben-Systemen in porzinen Knochenbiopsien vorherzusagen. Eine quantitative Übereinstimmung mit experimentellen Ergebnissen konnte nur durch eine präzise Abstimmung der Kontaktmodellierung, Materialeigenschaften und Vorschädigungsparameter erreicht werden.

Diese Arbeit erweitert ParOSol-NL zu einem leistungsfähigen, nichtlinearen µFE-Simulationswerkzeug für Knochen- und Knochen-Schrauben-Systeme. Die Vorhersagegenauigkeit des Lösers wurde auf der Mesoskala validiert und vereinfachte Kontakt- und Vorschädigungsmodelle wurden implementiert, um die Simulation der Knochen-Schrauben-Interaktion zu verbessern. Diese Weiterentwicklungen ermöglichen detaillierte und zugleich recheneffiziente µFE-Analysen, wodurch realistische biomechanische Simulationen mit hoher numerischer Effizienz realisiert werden können.

Contents

Chapter 1

Introduction

1.1 Problem Statement

Bone fractures are among the most common injuries worldwide [1–3], affecting people of all ages due to accidents, falls, and various health conditions like osteoporosis [4]. The growing prevalence of fractures has led to a significant demand for effective treatments that can restore function and integrity to the affected bones. A common approach to treating fractures, especially in cases involving complex breaks, involves the use of orthopedic implants—devices such as plates, screws, and rods that are surgically placed to hold bones together as they heal [5,6]. However, while these implants have revolutionized fracture treatment, they come with their own set of complications, including failures and loosening over time, which can require additional surgeries and lead to prolonged recovery or other complications [7,8].

Research in bones and bone-implant systems is crucial, as it helps us understand how bones fracture, heal, and interact with implants [9]. Advanced research allows scientists to develop improved implant designs that integrate better with bone, reducing the risk of complications and improving long-term stability [10]. Through these advancements, patients experience faster recoveries, lower healthcare costs, and better outcomes, especially for those with unique needs like elderly patients or those with osteoporosis [11].

A promising area of innovation in bone and bone-implant research is computational modelling [12–14], which involves using advanced software and algorithms to simulate how bones and implants behave under various conditions. One of the significant advantages of computational modelling over experimental testing is that it allows researchers to explore a wide range of variables and conditions without the cost, time and, ethical constraints of physical testing [12]. Moreover, computational modelling accelerates the design and testing phase of orthopedic implants, as different scenarios, such as varying loading conditions, or implant placement can be easily adapted [12]. This helps to refine designs, and identify potential issues early in the development process, which accelerates the pace that research can translate into faster development of improved implants and ultimately lead to better patient outcomes [12].

Finite Element (FE) modelling [15] is a popular computational technique used for mechanical simulations, where a structure is divided into smaller, manageable elements to analyse stresses, strains, and other mechanical quantities. Micro FE (µFE) models [16–18] are a specialized application of this method, using extremely small elements to capture microstructural features with high accuracy. This allows for detailed simulations that provide valuable insights into local stresses and strains within bones, helping to understand how fractures may initiate and propagate. Especially in bone-implant systems, accuracy in capturing the implant geometry and the surrounding bone microstructure in the peri-implant region has been proven to be crucial for assessing its mechanical competence [19–21].

However, the high level of geometric detail required to perform microscale simulations also comes with trade-offs. The increased number of elements in µFE models leads to higher computational demands, particularly in terms of memory and processing power [22]. The computational costs increase further if nonlinearities, such as nonlinear material behaviour and contact nonlinearities, are included. The incorporation of nonlinearities enhances the realism and accuracy of the model, but also increases the complexity of the simulation. The material's response becomes more difficult to characterize, and solving these models typically requires more computational resources.

To manage the computational demands of µFE models, researchers often rely on specialized solvers [23–25], which can efficiently handle the large amounts of data and computations involved in simulating bones and bone-implant systems. These solvers employ advanced algorithms and parallel processing techniques to distribute calculations across multiple processors, enabling faster computation times even for models with millions of elements.

While specialized µFE solvers significantly improve computational efficiency, they generally lack the ability to include mechanical behaviour beyond linear elasticity, such as nonlinear material behaviours or contact nonlinearities. Linear elastic behaviour is often sufficient to answer research questions in bone biomechanics, such as identification of regions with high stresses and strains. However, it does not allow to study the failure of bone or bone-implant systems in detail.

To address these limitations, general purpose FE solvers like Abaqus and Ansys are frequently employed due to their versatility and ability to incorporate greater model complexity. These solvers typically support a range of advanced features, enabling the inclusion of material nonlinearities and complex contact interactions—both of which are essential for accurately representing the mechanical behaviour of bone and bone-implant systems under realistic conditions. However, this increased versatility comes at a cost: general purpose solvers are generally less computationally efficient, which can present significant challenges when analyzing large or high-resolution models.

While specialized µFE solvers enable efficient computations, their lack of model complexity limits their application in accurately capturing bone's mechanical behaviour. General purpose FE solvers, though versatile, sacrifice computational efficiency. These trade-offs highlight the challenges researchers face in balancing model detail and computational practicality, underscoring the need for continuous advancements in µFE solver technology to achieve both efficiency and realism in bone biomechanics modelling.

Stipsitz et al. [24] addressed this challenge by enhancing the accuracy of efficient µFE simulations in bone biomechanics through the development of ParOSol-NL, an advanced nonlinear version of the specialized solver ParOSol [25]. This nonlinear adaptation allows ParOSol-NL to incorporate nonlinear material properties, a significant improvement over its predecessor, which was confined to linear-elastic analyses. Additionally, Stipsitz et al. [24], [26] calibrated material parameters using trabecular bone biopsy data and conducted verification and validation at the macroscale to ensure that simulations were both reliable and realistic. These enhancements allowed ParOSol-NL to perform efficient nonlinear µFE simulations on bone biopsies and bone segments.

However, several critical milestones still remain unmet. No validation at the mesoscale has yet been performed, leaving the solver's validity at the local level unconfirmed. Furthermore, ParOSol-NL does not yet support contact modelling, significantly restricting its potential for

studying bone-implant systems.

1.2 Goals and Objectives

The overarching aim of this thesis was to further validate and enhance the specialized µFE solver ParOSol-NL to create a powerful tool for µFE simulations that provides both efficiency and accuracy for studying bone and bone-screw systems. The focus on screws as implants was deliberate, as they are a universal and critical component in numerous orthopedic applications, ranging from fracture fixation to prosthetic anchorage.

Figure 1.1 gives an overview of this thesis. To reach the final aim from the starting point, four subgoals needed to be reached. First, ParOSol-NL's predictive accuracy at the mesoscale was assessed to ensure reliable local predictions of bone structures. Mesoscale validation is crucial for accurately modelling the mechanical behaviour of bone-screw systems, which relies on the local interaction between the screw threads and the bone microstructure. It is important to note that the validation was limited to the lowest measurable scale (sub-macroscale, i.e., mesoscale) and to robustly measurable variables (displacement fields) of currently available experimental techniques. Next, for simulating bone-screw systems, an efficient and accurate contact model was developed to capture the interaction between bone and screw. This contact model should enable ParOSol-NL to accurately simulate mechanical interactions between screws and the surrounding bone tissue. Additionally, an efficient pre-damage model that represents the bone damage caused by screw insertion was incorporated into ParOSol-NL. Finally, the capabilities of ParOSol-NL including simplified contact and pre-damage, were evaluated by comparing bone-screw pull-out simulations to experiments.

In line with the four subgoals (see figure 1.1), the objectives of this thesis were as follows:

(1) Validate displacement fields in bone biopsies predicted by ParOSol-NL at the mesoscale.
(2) Develop an efficient and accurate contact model for bone-screw interactions compatible with ParOSol-NL.
(3) Incorporate an efficient pre-damage model to represent bone damage from the screw insertion process.
(4) Evaluate ParOSol-NL simulations with simplified contact and pre-damage by comparing predicted bone-screw pull-out forces with experimental measurements.
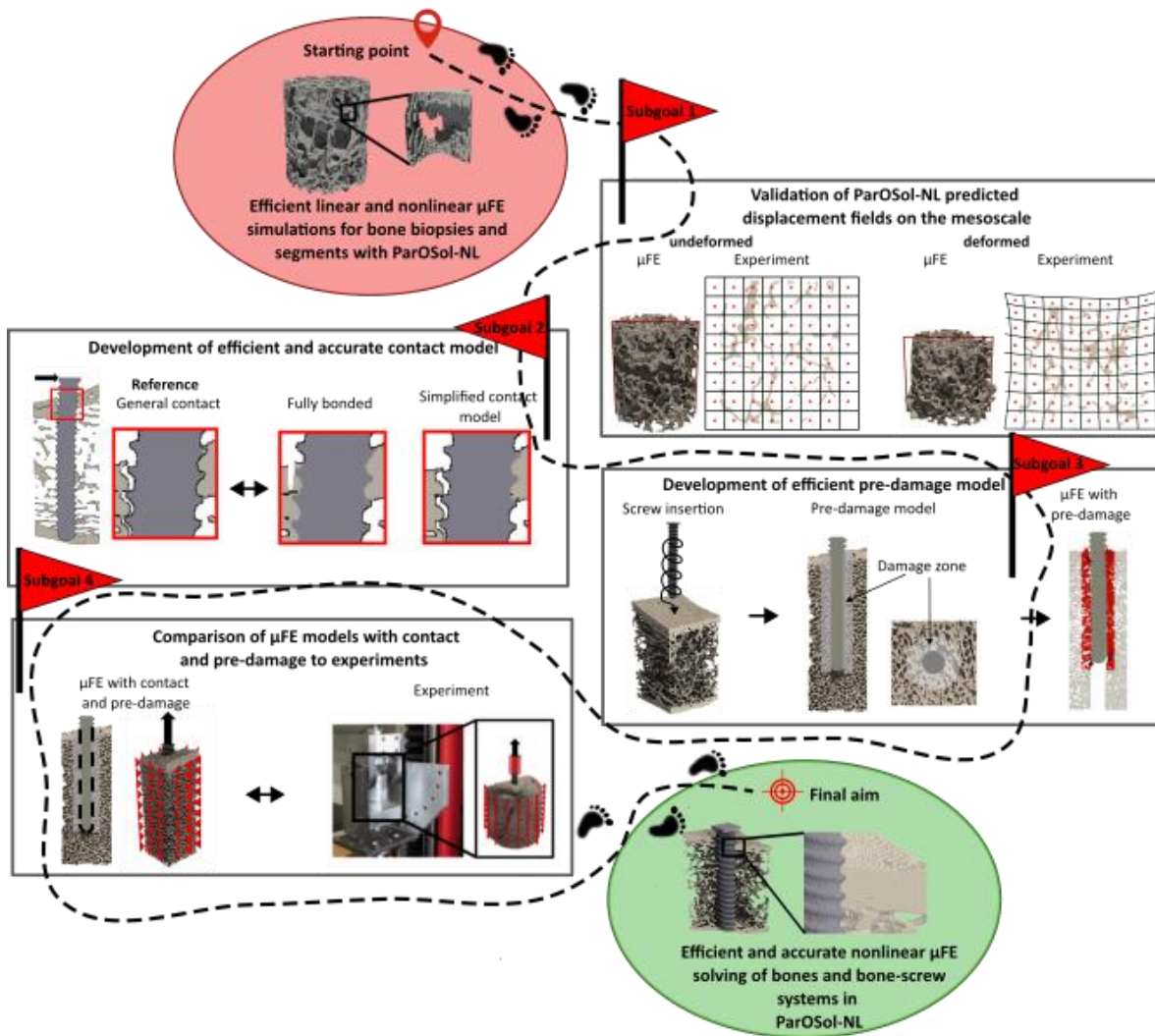
Fig. 1.1 Graphical abstract of this thesis, including starting point, final aim and four subgoals.

1.3 Background

Chapter 1.3 provides background information based on literature, which was required to conduct the scientific studies presented in chapters 2-4. Own contributions are described in chapters 1.4 and 1.5.

1.3.1 Bones and Bone Fracture

This chapter provides a brief introduction to bone structure across different scales, from the macroscopic to the nanoscopic level (see figure 1.2). It specifically explores the mechanical behaviour of bone tissue at the microscale, which is most relevant for µFE simulations. Additionally, the chapter addresses bone fractures as well as their implications. Different bone fracture types are discussed and the various phases of bone healing are explained, offering insights into the complex biological processes involved in recovery.

1.3.1.1 Hierarchical Structure of Bone

Bone tissue exerts important functions in the human body, such as providing structural support, protecting internal organs, and serving as a reservoir for mineral storage [27]. It also exhibits remarkable mechanical properties, including high stiffness, strength, toughness, and lightweight [27]. Its complex hierarchical structure spans from the macro- to the sub-nanoscale [27]. Knowledge at every level is crucial because each scale contributes to the overall functionality of bone [27].

At the macroscale, bone tissue is composed of two types: cortical (compact) and trabecular (cancellous) bone. Cortical bone forms a dense outer shell with low porosity (5-10%) [28] that primarily functions as a load-bearing structure, providing mechanical strength and protection [29]. Cortical bone surrounds trabecular bone, which is highly porous (50-90%) [28] and located primarily at the ends of long bones [29]. Its porous structure plays a key role in energy absorption and load distribution [29].

At the microscale, trabecular bone consists of an intricate network of interconnected struts and plates, known as trabeculae [29]. The orientation of the trabeculae is adaptive, aligning primarily along the directions of greatest stress, optimizing the bone's structural integrity to withstand repetitive and multidirectional forces [30]. The microstructure of cortical bone is dominated by osteons [31]. Osteons, or haversian systems, are cylindrical units, each surrounding a central Haversian canal [31]. These canals house blood vessels and nerves, which are crucial for maintaining bone health by supplying nutrients and oxygen while removing waste products [31]. The spaces between osteons are filled with interstitial bone, made up of remnants of old osteons [31]. Both cortical and trabecular bone share a fundamental building block: lamellae [28]. Lamellae are thin layers of bone tissue, made from mineralized collagen fibril bundles arranged in a highly organized manner [28]. In trabecular bone, lamellae are primarily aligned along the long axis of the trabeculae to optimize load-bearing efficiency [28]. In cortical bone, the lamellae alternate in orientation between adjacent layers, which enhances strength and resistance to fracture under multidirectional forces [28].

At the nanoscale, mineralized collagen fibril bundles decompose into single mineralized collagen fibrils, which represent the fundamental structural units of bone [29]. These fibrils are composed of three key components: an organic matrix, minerals, and water [29]. The organic matrix predominantly contains type I collagen, which provides flexibility and tensile strength [32]. The mineral component, primarily hydroxyapatite, lends bone its stiffness and ability to withstand compressive forces [32].
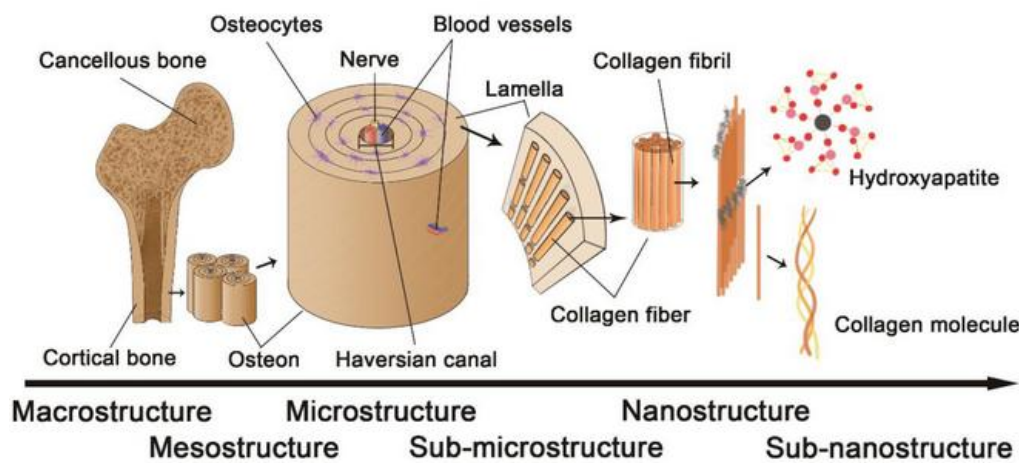
Fig. 1.2 The hierarchical structure of bone from the macro- to the sub-nanoscale [33].

1.3.1.2 Mechanical Behaviour of Bone

Bone tissue mechanical behaviour exhibits significant natural variation due to several biological and environmental factors as species, age, anatomic site, hydration state and loading direction [34]. Moreover, the hierarchical structure of bone, composed of multiple levels of organization from the molecular to the macroscopic scale, results in a wide range of mechanical properties that are highly dependent on the scale being considered [27]. At each level—whether molecular, microstructural, or macrostructural —the mechanical behaviour of bone varies significantly due to the organization of its components [27]. The chapter focusses on the mechanical behaviour of bone at the microscale as material models for μFE simulations have to represent tissue mechanics at this scale.

Bone properties at the microscale are influenced by factors such as collagen orientation, the crosslinking profile of collagen, the degree of mineralization, and the presence of bound water within the bone matrix [35]. When subjected to mechanical loading, bone tissue initially responds with linear-elastic behaviour, where deformation is reversible. However, as the strain reaches around 0.4-2.5% [36,37], the tissue reaches its yield point, marking the transition from elastic to plastic deformation, leading to a permanent change in structure that will not recover once the load is removed. After yielding, bone shows a quasi-brittle behaviour [38]. This means that although the tissue hardens and can continue to bear additional loads, it also begins to accumulate microdamage in the form of microcracks [39]. This damage accumulates and can lead to a reduction in the bone's apparent elastic modulus, as the microstructure deteriorates [40]. Despite this quasi-brittle behaviour, bone retains a degree of toughness [39], which refers to its ability to absorb energy before fracturing. This toughness is largely derived from its plasticity, where the ability to undergo permanent deformation before failure enables bone to dissipate energy and delay catastrophic fracture [41]. Both cortical and trabecular bone tissues exhibit anisotropic behaviour at the microscale, as their mechanical properties vary based on the orientation of the mineralized collagen fibers [42]. Both types of bone are stronger in compression than in tension [43,44] and hence show a tension-compression yield strength asymmetry [36]. Although cortical and trabecular bone tissues share a similar composition—both are made up of a matrix of collagen fibers embedded with hydroxyapatite mineral—there are subtle differences in their mechanical properties, largely due to differences in porosity and structure. It is reported that trabecular bone has a slightly reduced elastic modulus, lower yield strain, and lower strength compared to cortical bone [36].

1.3.1.3 Bone Fracture

From a clinical point of view, bone fractures can be defined as an interruption of the continuity

of bone [45]. It occurs when a bone breaks or cracks due to high-impact force, pressure, or stress beyond its strength [46]. Fractures generally result from falls, accidents, sports injuries, or direct blows to the body [46]. Medical conditions like osteoporosis and certain cancers can also weaken bones, making them more susceptible to fractures from even minor stress [46].

Fractures are classified based on their appearance, severity, and how the bone is affected [47]. Based on the fracture morphology, one discriminates some common fracture types:

- **Complete fracture:** The bone is broken into two or more pieces. Generally, complete fractures displace the bone fragments which are no longer aligned [46].
- **Incomplete fracture:** The bone cracks but does not break all the way through [46].
- **Comminuted fracture:** The bone shatters into three or more pieces, common in high-impact traumas like car accidents [46].
- **Intra-articular fracture:** Intra-articular fractures extend into the joint space, meaning that the fracture line crosses the articular surface [47].
- **Extra-articular fracture:** Extra-articular fractures occur outside of the joint space and do not extend into the articular surface of the bone [47].

The fracture pattern and morphology gives an indication on the optimal selection of fracture treatment [48]. By assessing the characteristics of a fracture, treatments to ensure optimal healing, alignment, and function can be tailored. Simple, stable fractures often need only immobilization, while complex or unstable fractures, especially those prone to displacement, may require surgical fixation [48].

1.3.1.4 Bone Fracture Healing

Bone fracture healing is a complex biological process that aims at complete restoration of the damaged bone tissue [49]. The process involves a series of events, with various cellular and biomechanical factors working together [49].

One can discriminate two main types of bone healing: primary (direct) and secondary (indirect) bone healing [50]. Primary bone healing occurs when the bone fragments are closely aligned and rigidly stabilized, typically through surgical fixation [51]. New bone tissue forms directly across the fracture site, bypassing the formation of inflammation and callus [51]. Secondary bone healing is more common and occurs when there is some movement or gap between the bone fragments [50]. It involves a multi-stage process, including inflammation, soft callus, hard callus, and remodelling [50]. During inflammation, a hematoma forms at the fracture site, attracting immune cells to clear debris and activate bone-forming cells [52]. The hematoma is then replaced by a soft callus, a fibrous tissue that stabilizes the fracture but lacks load-bearing capacity [53]. Next, hard callus develops as osteoblasts create woven bone through enchondral and intramembranous ossification, enhancing mechanical stability [53]. Finally, during remodelling, the woven bone transitions into stronger, organized lamellar bone, restoring the bone's original structure [53].

1.3.2 Bone Fracture Treatment

This chapter provides an overview of contemporary methods for the treatment of bone fractures. It begins by distinguishing between conservative approaches and surgical interventions. The discussion transitions to internal fixation devices, with a particular focus on bone plates and screws. The chapter discusses conventional plates and locking plates, and finally describes the specifics of locking screws. Their design and functional role as a critical element for fracture fixation are analysed.

1.3.2.1 Conservative and Surgical Approaches

Bone fractures generally requires medical intervention to ensure the bone heals properly and regains its structural integrity and biomechanical properties [6]. The treatment depends on the type and severity of the fracture. Minor, non-displaced fractures can be treated conservatively, for example, by immobilizing the affected area with a splint or cast [54]. For more complex fractures, surgical interventions of the bone, known as osteosynthesis, are required to reposition the fractured fragments into their normal alignment and immobilize them by either internal or external fixation. External fracture fixation offers low soft tissue damage and is accomplished using pins and wires which are inserted percutaneously [6]. In contrast, internal fixation is achieved with surgical implantation of different orthopedic devices as for example plates, screws, and nails [6].

The choice of method depends on the type of fracture, location, cause, and severity [46]. A commonly used fracture fixation device is the bone plate. The plates are affixed to the surface of the bone using screws, and act as an internal splint to maintain proper alignment while the bone heals [6]. In general, one can discriminate between conventional, unlocked plates and locked plates which rely on different mechanical principles.

1.3.2.2 Conventional Plates

Conventional bone plates aim to provide absolute stability [55]. The tightening of the screws (see figure 1.3 (left)) results in normal force between bone and plate and compresses the plate on the bone [55]. A reactionary friction force between bone and the undersurface of the plate develops and provides support to the plate [55].

Conventional plates encourage primary fracture healing by providing rigid fixation with little to no movement at the fracture site [56]. The absolute stability they offer prevents micromotion at the fracture, allowing the bone to heal through intramembranous ossification, where new bone is formed directly across the fracture without the formation of a callus [56]. Primary bone healing is particularly preferred for intra-articular fractures, where callus formation might impair joint function [56].

However, conventional plates have several drawbacks that can complicate fracture stabilization and bone healing. While increasing screw torque can enhance load-bearing capacity by raising friction, it also heightens the risk of screw failure, particularly in osteoporotic or comminuted bone, where sufficient torque without loosening is often unachievable [57]. Additionally, load distribution in conventional plates is uneven, with screws nearest or farthest from the fracture site bearing the majority of stress [55]. The failure of one screw can trigger a domino effect, leading to sequential loosening and pull-out of others [55]. Mechanical adjustments to improve mechanical competence may also cause biological issues, such as impaired blood circulation due to higher compression forces, increasing the risk of necrosis and porosis [58]. Furthermore, the rigidity of conventional plates contributes to stress shielding, reducing mechanical stress on the bone, which can result in bone resorption and weakening over time [58].
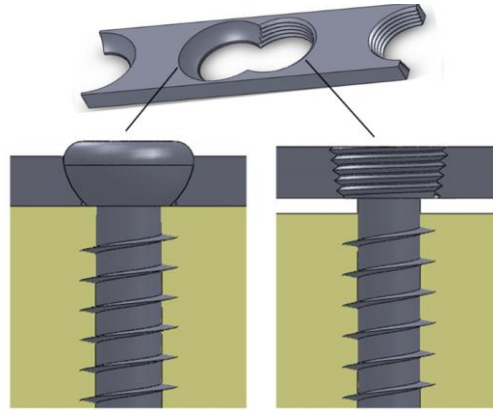
Fig. 1.3 Illustration of a conventional screw/plate system
(left) and a locking screw/plate system (right) [59].

1.3.2.3 Locking Plates

Locking plates (see figure 1.4) stabilize bone fragments through a rigid, fixed-angle coupling between the screw and the plate [55]. The locking screws, which are used together with locking plates, have threads not only along the shaft but also on the lateral surface of the head [55]. To create the locking mechanism, the head of the screw locks into the threaded hole of the plate and creates an axially and angularly stable connection between the screw and the plate itself [55].

In comparison to conventional plates, the compressive forces between bone and plate are highly reduced in locking plates as the intimate contact between bone and plate is no longer required [60]. These conditions are ideal for secondary bone healing with callus formation, which leads to faster healing and improves the mechanical performance of the healed bone tissue [60]. Furthermore, the periosteal blood supply can be preserved which prevents excessive bone resorption [60].

The specific design of the locking plate increases fixation of the fracture [55]. The plate, which acts as a surrogate cortex, can carry a large portion of load [55]. Together with the locked screws, the fixator allows to distribute forces evenly across the entire bone-plate construct, relieving stressed parts at the bone-screw interface [55]. Furthermore, the locking mechanism increases failure resistance, as the screws cannot toggle to align with the applied force but act together with the plate as a unit [55]. The strength of the fixator is composed of the strength of all bone-screw interfaces included in the construct [55]. In consequence, the fixation is less dependent on the local bone quality in the anchoring region and the risk for screw loosening or bone failure especially in bone with poor quality can be reduced [55].

The decision whether to use a locking plate should involve several factors including the anatomical region of the fracture, the fracture pattern, and the bone quality. Especially fractures that have a high risk of non-union or loss of stability, as osteoporotic, peri-articular, and comminuted fractures should be treated with locking plates [61].

Due to the frequent usage of locking plates for the fixations of certain fractures types [62], this thesis is focused on locking screws, which are specially designed to work together with locking plates.

Fig. 1.4 Volar locking plate fixation of a distal radius fracture.

1.3.2.4 Locking Screws

Locking screws (see figure 1.3 (right)) are designed to work in combination with locking plates, creating a rigid fixation system. They include threads at the lateral surface of the screw head which engage with the corresponding threads in the plate when the screw is tightened [55]. Because of the rigid plate-screw connection, the locking screws must handle complex, multiaxial forces that arise from different movements and loads on the bone [63].

The locking screw tip can be either self-drilling (see figure 1.5 (A)) or self-tapping (see figure 1.5 (B)). The self-tapping tip includes a so-called "flute", which serves as the thread-cutting device and enables the screw to cut its own threads into the material as it is driven in [55]. Self-tapping screws require a pre-drilled pilot hole prior to screw insertion. The pilot hole, matching the screw's core diameter, ensures proper guidance and reduces insertion stress [64]. Improper pilot hole sizing can increase insertion torque, risking screw breakage, or reduce pull-out strength [64]. However, drilling generates heat and friction, potentially causing thermal bone damage and microcracks near the hole [65–68]. A self-drilling tip combines both a drill and a tap section. This design allows the screw to simultaneously drill a hole and cut the exact profile of the screw threads directly into the material [55,69]. Self-drilling screws don't need a pre-drilled hole and can be inserted directly. This simplifies instrumentation and minimizes bone debris and thermal damage compared to self-tapping screws [70,71]. However, the required insertion torque was reported to be higher which could on the one side cause negative effects as microdamage but also leads to higher primary stability [72].
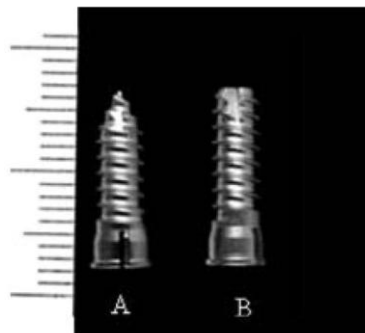
Fig. 1.5 Self-drilling (A) and self-tapping screw (B) [73].

1.3.3 Research in Bones and Bone-Screw Systems

This chapter discusses different approaches to conduct research on bone tissue and bone-screw systems. The research is usually conducted to enhance our understanding of its mechanical behaviour or to improve screw designs and surgical techniques to avoid fracture fixation failure.

1.3.3.1 Experiments

Experimental tests can be broadly categorized into in vivo [74–76] and in vitro [77–80] methodologies. In vitro tests are typically conducted on cadaveric specimens or synthetic bones and are used to simulate mechanical behaviour under controlled conditions. Conversely, in vivo tests are essential for understanding the biological and mechanical behaviour of bones and bone-screw systems within living organisms. These tests capture the effects of real physiological conditions, including the interaction between biological and mechanical factors, such as bone remodelling and, healing.

For in vitro and in vivo experimental testing, standard mechanical tests are commonly used to evaluate bone and bone-screw mechanical properties and their response to loading conditions. These tests are performed using mechanical testing machines, which apply loads typically at a force- or displacement-controlled constant loading rate [81]. Internal (e.g., load cells) or external (e.g., extensometers) sensors measure the occurring displacements and loads [82]. These data are generally used to generate load-displacement curves, which provide key mechanical parameters such as the ultimate strength and elastic modulus. Standard mechanical tests of bone include uniaxial tension and compression tests, bending and torsion tests. In bone-screw systems, push-out and pull-out tests, are commonly used to measure the strength and stiffness of implant anchorage in bone [81].

For more local measurements, bone surface strain is often measured using strain gauges. Small, sensitive electrical devices are directly attached to the surface of a bone, which are able to measure the experienced strain via electric resistance variations [83]. So-called strain gauge rosettes are able to measure both the direction and the magnitude of principal stain. The method is commonly used both in in vitro [84] and in vivo studies [85,86], where it enables measurement of strain under physiological loading conditions, providing critical insights into bone behaviour in living organisms.

Imaging techniques, such as micro-computed tomography (micro-CT), are used to visualize internal structures and assess bone quality, screw fixation, and screw-bone interface interactions [87,88]. To study local displacements and strains, digital image correlation (DIC) or digital volume correlation (DVC) methods can be used. The DIC technique relies on applying a random speckle pattern to the bone surface [89]. This pattern serves as a unique reference, enabling the DIC software to track and match specific features between images before and after deformation, to calculate surface deformations [89]. DVC, an extension to DIC, works on 3D volume data. It compares 3D images of the bone before and after deformation and can capture the internal deformation within the bone (see section 1.3.4.4) [89].

1.3.3.2 Computational Modelling

Computational modelling revolutionized engineering by enabling numerical simulations of complex problems that cannot be solved analytically. Numerical methods allow the transformation of partial differential equations, commonly used to describe the mechanical behaviour of complex engineering systems, into algebraic equations that can be solved computationally [15]. Among these methods, the FE method stands out as one of the most prominent due to its effectiveness and versatility (see section 1.3.4) [15]. The method is

nowadays widely employed to simulate the mechanical behaviour of bone and bone-screw systems [13,18].

FE simulations offer distinct advantages over experimental methods, providing a non-destructive and highly versatile approach for studying bone mechanics [12]. Unlike experiments, FE models overcome ethical and practical limitations, enabling detailed simulations without the need for actual samples [12]. Additionally, FE models are time- and cost-effective, allowing for repeated simulations under varying conditions without the need for additional samples [12]. Researchers can easily adjust parameters, such as material properties or loading conditions, and instantly observe the effects, making it easier to explore a wide range of scenarios quickly and efficiently [12].

Two main types of FE models have emerged over the years in bone and bone-screw construct research: homogenized FE (hFE) models and µFE models. hFE modelling simplifies the mechanical analysis of complex materials and structures by representing them as continua, leveraging averaged material properties derived from homogenization techniques [90]. This approach enables the efficient modelling of structures at macroscopic scales, with element sizes typically in the millimeter range [90]. Input geometries for hFE models are often derived from imaging techniques such as CT or magnetic resonance imaging (MRI), which provide sufficient resolution to capture the overall shape and volume of the structure without requiring detailed microstructural data [90]. As a result, hFE is computationally efficient [91] and particularly applied for scenarios where capturing the global mechanical behaviour is sufficient [92,93].

µFE models [16–18] use elements with sizes at the microscale, enabling them to accurately capture the intricate structure of trabecular bone. These models provide detailed insights into local stress and strain distributions and uncover potential failure mechanisms that are challenging to observe with experimental methods. Especially in bone-screw studies, this fine resolution is essential, as the precise geometry of both the screw and peri-screw region significantly affects the system's mechanical stability, making µFE models indispensable for accurate simulation of bone-implant interactions [19–21]. Due to these reasons, µFE models have become the gold standard in computational modelling of bone and bone-screw biomechanics [94].

1.3.4 µFE Modelling of Bones and Bone-Screw Systems

In this chapter, the fundamentals of the FE method are introduced, with a particular focus on its application at the microscale: the µFE method. The chapter explores the application of µFE modelling in the analysis of bone structures and bone-screw systems. Key aspects of modelling are examined in detail, beginning with an overview of various material modelling approaches and the specific challenges associated with bone-screw contact mechanics. The chapter also addresses the challenges involved in simulating damage resulting from the screw insertion process. Additionally, it reviews different types of µFE solvers, emphasizing their capabilities and limitations when handling µFE problems.

1.3.4.1 Basics of the FE Method

The FE method is a powerful computational technique used to approximate the behaviour of complex systems by subdividing a continuous domain into a finite number of smaller, simpler subdomains, called elements, connected by nodes [95]. The unknown variables — such as displacement or stress fields — are approximated over each element [95]. These local approximations are then assembled into a global system of equations, which is solved numerically to yield an approximation of the true solution [95].

FE simulations can be categorized based on various criteria, such as system behaviour or time dependence. When the system experiences only small deformations and linear stress-strain relation, a linear FE simulation is typically used, where the system is modeled using linear partial differential equations [96]. However, many engineering problems require more complex models that cannot be adequately described by linear equations. In these cases, nonlinear FE simulations are necessary. Nonlinear behaviour can arise from several sources, including geometric nonlinearity (large displacements and rotations), material nonlinearity (nonlinear stress strain relation), nonlinear boundary conditions (contact between two bodies), bifurcation of equilibria (buckling) [96]. When considering time dependence, finite element analyses can be further classified as static or dynamic. In static analyses, the load is either constant or changes slowly over time, and the system remains in an equilibrium state where time and inertial effects are negligible [97]. In contrast, dynamic analyses deal with loads that vary over time, causing the system's response to change. In this case, inertial and damping effects must be considered [97].

The governing equation that needs to be solved in static, linear finite element simulations is stated as follows [15]:

$$\underline{\underline{K}}\,\underline{U} = \underline{F}_{\text{ext}} \tag{1.1}$$

$\underline{\underline{K}}$ denotes the global stiffness matrix of the domain, $\underline{U}$ denotes the nodal point displacements of the total assembly, and $\underline{F}_{\text{ext}}$ represents the vector of nodal forces due to applied loads. In nonlinear problems [98], the relationship between forces and displacements is no longer linear. Hence, an incremental formulation is needed, where information about the known equilibrium condition ($t = t^{(m)}$) is used to derive the unknown equilibrium condition ($t = t^{(m+1)}$). At $t^{(m)}$ the nonlinear system is linearized. The governing nonlinear finite element equation can be expressed as [98]:

$$\underline{\underline{K}}^{(m)}\,\underline{\Delta U} = \underline{F}_{\text{ext}}^{(m+1)} - \underline{F}_{\text{int}}^{(m)} \tag{1.2}$$
$$\underline{U}^{(m+1)}\text{-}\underline{U}^{(m)} \tag{1.3}$$

14

$\underline{\underline{K}}^{(m)}$ is the global tangential stiffness matrix in configuration m and $\underline{F}_{int}^{(m)}$ denotes the vector of internal forces in configuration m. $\underline{U}^{(m)}$ and $\underline{U}^{(m+1)}$ refer to the nodal displacement vectors for all nodes at time $t = t^{(m)}$ and $t = t^{(m+1)}$.

Linear system of equations are typically solved using direct (e.g. Gaussian elimination) or iterative (e.g. Conjugate Gradient (CG)) solution methods. Direct methods provide exact solutions in a finite number of arithmetic steps, while iterative methods start with an initial guess and refine the solution through successive iterations [99]. Since assembling and storing the actual stiffness matrix is not efficient especially for large systems, a matrix-free approach is often employed. Instead of forming and storing the global stiffness matrix, matrix-vector products are computed directly at the element level using an element-by-element strategy, which reduces memory usage and computational time [100]. For nonlinear systems, incremental-iterative methods (e.g. Newton-Raphson and modified Newton-Raphson) are the standard approach. Due to the nonlinear nature of these problems, the equilibrium path cannot be directly solved, so the load is applied incrementally in small steps [101]. At each step, the nonlinear system is linearized around the current state and the equilibrium path of the system is followed through a sequence of small tangential linear steps [101].

When solving FE problems, one discriminates two different time integration strategies, namely implicit and explicit. Implicit methods involve solving the equilibrium equations for the entire system at each time step, requiring the assembly of the global stiffness matrix [102]. This process can be computationally intensive especially for nonlinear, large-sized models but provides unconditional stability for larger time steps, making it well-suited for simulations of static or quasi-static problems [103]. In contrast, explicit methods advance the solution based on the system behaviour at the current state, without forming or solving a global system [103]. This eliminates the need for global stiffness matrix assembly, making explicit methods computationally efficient per step and ideal for analyses with large nonlinearities or changing contact conditions [103].

When dealing with highly nonlinear problems, implicit time integration often encounters convergence challenges. To address this, the problem can be reformulated as a quasi-static process and solved using explicit time integration [104]. However, performing a quasi-static analysis on its true time scale is generally impractical due to the excessive runtime required. To reduce computational time, two common strategies can be employed: time scaling and mass scaling [104]. Time scaling involves increasing the loading rate until inertial effects become negligible, while mass scaling artificially increases the mass of the model to allow for larger time increments, while maintaining stability [104]. To ensure the simulation remains quasi-static and avoids introducing unrealistic dynamic effects, it is crucial to minimize the influence of inertial forces on the mechanical response. This can be achieved by maintaining the ratio of kinetic energy to total internal strain energy below 5% to 10% [105].

1.3.4.2 Basics of μFE Modelling

μFE modelling (see figure 1.6 (A) and (B)) enables to capture the mechanical behaviour of materials and structures at the microstructural level. While standard FE typically deals with elements sizes in the millimeter range, μFE operates at much smaller scales, with element sizes typically in the micrometer range. As a result, μFE models can only be generated from highly detailed geometries obtained from imaging techniques like micro-CT, and demand high computational power due to the high number of elements involved [16]. The μFE approach is becoming increasingly important in the biomechanics field, where microscale behaviour significantly influences overall system performance [16]. Some common practices in μFE

modelling have evolved over time and are outlined in the following.
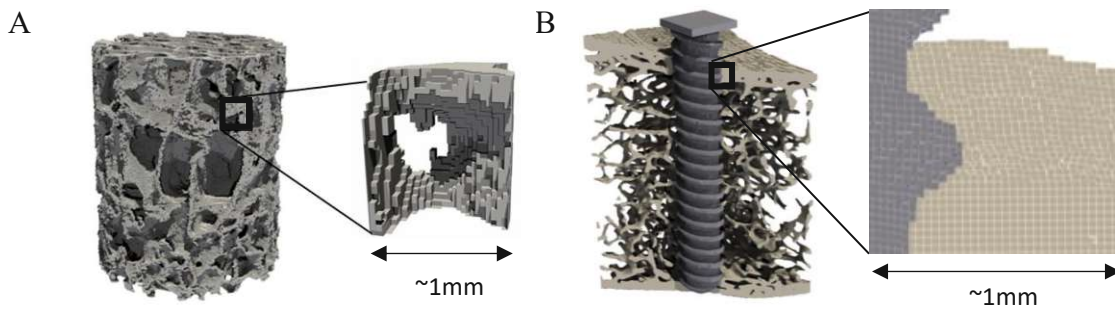
Fig. 1.6 µFE models showing a bone biopsy (element size: 36µm) (A) and a bone-screw system (element size: 32.8µm) (B).

The main steps to perform a µFE analysis are similar to conventional FE analysis and include mesh generation, material properties, and boundary conditions and loading conditions [106].

The starting point of a µFE analysis is the extraction of a surface mesh from a highly-resolved micro-CT image, that expresses the geometry of the object of interest. Typically, the µFE mesh is directly generated from the segmented image using voxel to element conversion [107,108]. This means that each voxel in the 3D image is converted into a corresponding hexahedral finite element. The elements are equal in shape, size, and orientation, enabling reduced storage of the data structure [100]. Another automated meshing technique utilizes the marching cubes algorithm [109,110], which converts voxels into tetrahedral elements of varying sizes. This approach allows for the creation of models with smooth trabecular surfaces, enhancing geometric accuracy. However, the increased smoothness comes at the cost of higher computational effort [17].

Each element in the mesh must be assigned appropriate material properties. The material model needs to be chosen based on the specific research question, e.g., an elastic model when the load remains within the elastic range, and a nonlinear model when the material undergoes large, permanent deformations [106]. Additionally, the selection of material properties must consider resolution, as bone shows different mechanical behaviours at different scales [27]. At the tissue level, bone properties are typically assumed to be isotropic and homogeneous, meaning that the same material properties are assigned in all directions. This assumption has been shown to be sufficient for predicting mechanical properties at the apparent level [107,108], as the anisotropy of bone is mainly determined by the trabecular architecture, which is captured at microscale mesh resolutions [111]. Furthermore, studies have demonstrated that mineralization heterogeneity has little effect on apparent material properties, supporting the simplifying assumption of material homogeneity [112]. However, studies investigating the similarity of trabecular and cortical bone tissue properties at the microstructural level have produced conflicting results, making it uncertain whether these two types of bone can be modeled in the same manner [113,114].

Finally, proper boundary conditions and loading scenarios need to be assigned to ensure accurate simulations. If the µFE results are to be compared with experimental data, it is essential that the boundary and loading conditions closely replicate the actual testing conditions [106]. In µFE analyses, boundary conditions are typically simple, involving the application or restriction of displacements at specific nodes or surfaces, such as compression, stretching, or full fixation [24,115–117].

1.3.4.3 Challenges in µFE Modelling

In addition to their numerous benefits, µFE modelling of bones and bone-screw systems presents several challenges that can affect the accuracy, reliability, and feasibility of the simulations. The major challenges include:

- **Dealing with large model sizes:** The high resolution of µFE models increases the number of elements, often reaching several hundred million, which raises computational demands. This necessitated the need for efficient µFE solvers, designed to handle large µFE problems within a reasonable timeframe.

- **Bone material modelling:** Bone exhibits nonlinear behaviour beyond its yield point, meaning that modelling failure in bone or bone-implant systems requires incorporating nonlinearities into the constitutive model, which inevitably increases the computational demands of the solution process.

- **Bone-screw interface modelling:** Appropriate interface modelling is essential for accurate simulations of the interaction between bone and screw. Nevertheless, contact algorithms can be computationally demanding.

- **Modelling of damage due to screw insertion and pre-drilling in bone-screw systems:** The pre-drilling and screw insertion process can induce damage in the bone, impacting the mechanical stability and long-term performance of the bone-screw system. However, accurately modelling this damage remains a challenging task.

Additionally, the identification of key modelling parameters (e.g., material properties, friction coefficients, and damage from screw insertion) poses a ubiquitous challenge in µFE modelling. However, these aspects will not be further addressed here, as they are equally present in conventional FE modelling of biological tissues. The following sections explain the above-mentioned challenges in more detail, how they have been dealt with in literature, and which challenges remain to be solved.

1.3.4.4 Bone Material Modelling in µFE Models

To perform µFE simulations of bones and bone-screw systems, a constitutive model of bone is required to describe the material behaviour through a stress-strain relationship [118]. This model is essential for accurately simulating the mechanical response of the system. In µFE, the material law and properties are applied locally at a resolution in the micrometer range, necessitating consideration of bone tissue behaviour at the microscale [118]. This chapter deals with commonly used constitutive laws generated to simulate bone behaviour with µFE models. The majority of models seek to balance intricacy and simplicity to achieve accurate yet computationally efficient simulations.

Linear-Elastic Material Models

Linear-elastic material models (see figure 1.7 (A)) are commonly used in µFE bone and bone-screw simulations [116,119,120] due to their simplicity and low computational costs. The models assume a linear stress-strain relationship but cannot capture nonlinear bone behaviour beyond yield, limiting their ability to predict failure loads accurately. A widely used criterion [117,121–124] to estimate failure in linear-elastic simulations was developed by Pistoia et al. [116]. It classifies elements as damaged based on local effective tissue strain. Failure is determined if 2% of elements exceed the critical strain value. As this criterion was initially developed to predict fracture of radii subjected to compression load, its parameters need to be adapted for each individual case [125] and can lead to under- or overestimations in failure load of up to one order of magnitude [121,122].
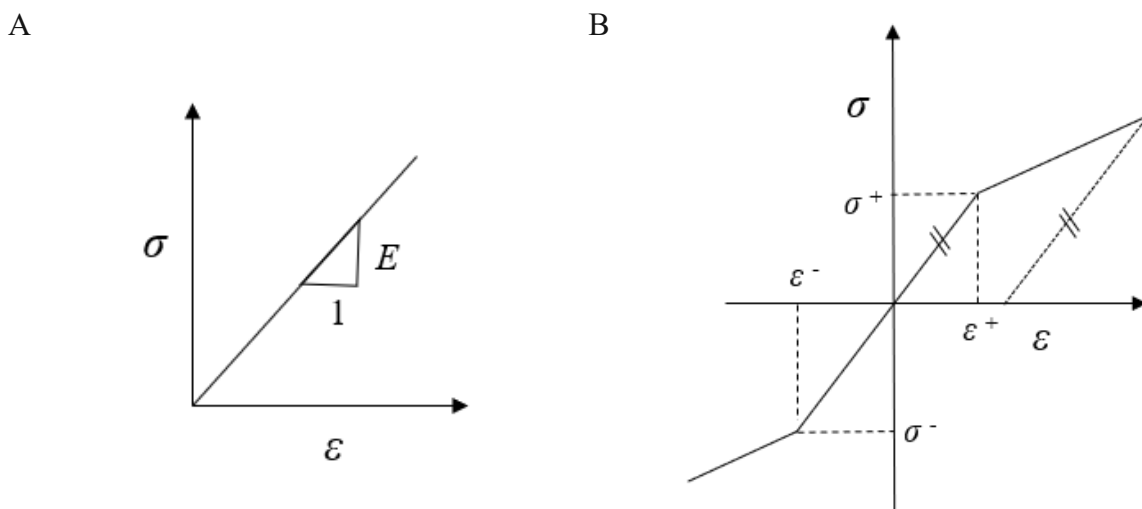
Nonlinear Material Models

When applied strains exceed the elastic limit of bone material, the predictive accuracy of linear-elastic models degrades. To enhance prediction performance, nonlinearities must be included in the selected constitutive law. However, introducing nonlinearities increases the complexity of the material formulation, resulting in higher computational demands. The majority of nonlinear constitutive models generated to model bone material behaviour in μFE models account for plasticity or damage [118].

Elasto-Plastic Material Model

In contrast to linear-elastic models, elasto-plastic material models (see figure 1.7 (B)) include material nonlinearity beyond yield and are able to describe bone as a material that exhibits both elastic and plastic behaviour. The models include a yield criterion corresponding to yield surfaces in 3D, e.g. von Mises [126,127], Drucker-Prager [126], or quadric approximations of the Drucker-Prager [128]. If this criterion is locally exceeded, the material undergoes permanent deformation. As tension-compression asymmetries were reported for bone tissue at the microscale, different yield strains in tension and compression are generally applied. Many elasto-plastic material formulations also account for isotropic hardening in the post-yield region [126,128]. While elasto-plastic models generally do not directly predict failure load [126,129], combining elasto-plastic behaviour with fracture mechanics provides a more comprehensive description, enabling failure load to be determined. Fracture is typically modeled using criteria that identify the onset and progression of material failure. For instance, elements in a FE analysis that exceed a predefined ultimate threshold, such as critical strain or stress, are often deleted from the model to simulate fracture [127].
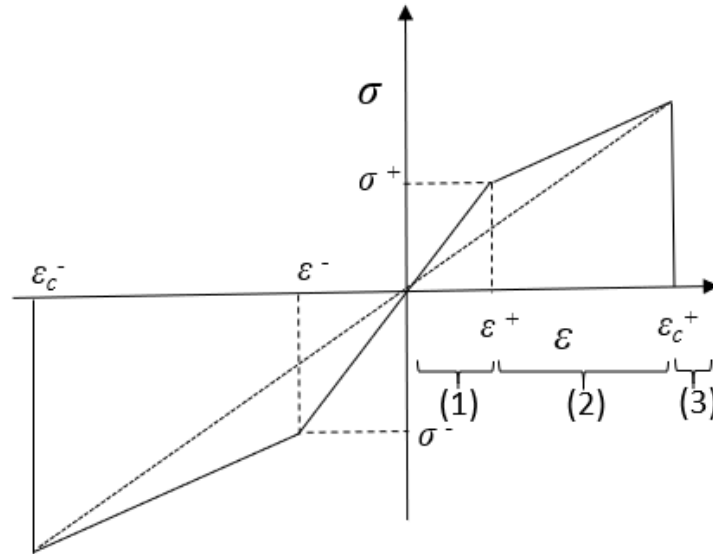
Damaged-Based Material Model

Damage-based material models (see figure 1.7 (C)) for μFE simulations are used to capture the progressive degradation of bone tissue under loading. These models introduce a damage variable that evolves with increasing strain, locally reducing material stiffness to simulate microstructural failure. Damage initiation and progression are typically governed by yield criteria, such as a critical strain threshold, indicating the onset of material degradation [24,130–132]. Some damage-based material models extend to include fracture, enabling the simulation of complete structural failure. Upon reaching a predefined critical threshold, based on variables such as strain, or cumulative damage, elements may either be removed entirely [131,132] or retain a minimal residual stiffness to approximate severely damaged regions [24].

A

B

C

Fig. 1.7 Stress-strain curves of different µFE material models: (A) linear-elastic material model, (B) elasto-plastic material model, and (C) damage-based material model with (1) linear-elastic region, (2) damaged region, and (3) fractured region.

Note: elastic modulus (E), stress (σ), strain (ε), damage onset stress/strain in tension (σ^+/ε^+), damage onset stress/strain in compression (σ^-/ε^-), critical strain in tension/compression ($\varepsilon_c^+/\varepsilon_c^-$).

1.3.4.5 Bone-Screw Interface Modelling in µFE Models

Although the contact interface plays a critical role in the stiffness and strength of the screw and the overall success of the fixation [133], the importance of contact modelling for accurate model prediction in µFE simulations still merits discussions [120]. Bone-screw contact modelling typically involves defining contact surfaces that can simulate friction, sliding, and possible separation between the screw threads and the bone. This chapter provides an overview of commonly used bone-screw interface models in µFE. The models presented vary significantly in terms of their complexity and computational efficiency. It is important to note that contact algorithms in µFE must strike an optimal balance between these two factors to ensure accurate and practical simulations.

Interface Based on Contact Algorithms

General-purpose contact algorithms (see figure 1.8 (A)) are widely regarded as the gold standard in interface modelling due to their ability to replicate physical contact across diverse applications [134]. These algorithms enforce contact conditions by preventing surface penetration and ensuring proper force transmission at the interface. To ensure contact conditions are satisfied, FE solvers rely on methods such as penalty-based enforcement or Lagrange multipliers [135]. The penalty method permits slight overlap between surfaces and applies a force that increases with the extent of penetration to push the objects apart [136]. In contrast, Lagrange multipliers introduce a constraint force that prevents overlap entirely, ensuring more precise contact enforcement but at the cost of greater computational difficulty [136]. For tangential behaviour, Coulomb's law of friction is commonly used [135]. It states that the frictional force is proportional to the normal force and opposes motion, with sliding occurring once the applied force exceeds the maximum static friction [135]. Despite their robustness and flexibility, general-purpose contact algorithms have notable computational demands. They must detect and update potential interactions between surfaces at every iteration, determining which regions are in contact and which are not. For models with large contact areas or multiple interacting bodies, this process can significantly increase computational overhead [135].

Fully Bonded Interface

A computationally efficient approach to address the challenge of bone-screw contact modelling is to assume full bonding (see figure 1.8 (B)) between bone and screw. This means that the µFE elements referring to bone material that are in contact with µFE elements referring to screw material, stay bonded from the start of the simulation until the end. This assumption does not correspond to reality as no direct bonding between bone and screw exists shortly after insertion. Consequently, the fully bonded interface assumption, though frequently used in literature, might lead to overestimations in whole-construct stiffness and strains [20,120,137].

Simplified Interface Models

Another approach for bone-screw contact modelling involves simplified interface models (see figure 1.8 (C)), which aim to strike a balance between computational efficiency and modelling accuracy. One such method, proposed by Steiner et al. [120], starts with a single preliminary simulation with the fully bonded interface, evaluated in the linear-elastic region. During this preliminary analysis, interface elements that experience positive volumetric strain are identified as being in tension and are subsequently removed, based on the assumption that tensile stresses cannot be transferred at the contact interface. In contrast, interface elements experiencing negative volumetric strain are considered to be in compression and are retained, as they are assumed to contribute to stress transfer between the bone and screw. After removing the disconnected elements, the updated interface is used to conduct the final nonlinear simulation, reflecting the modified contact conditions.
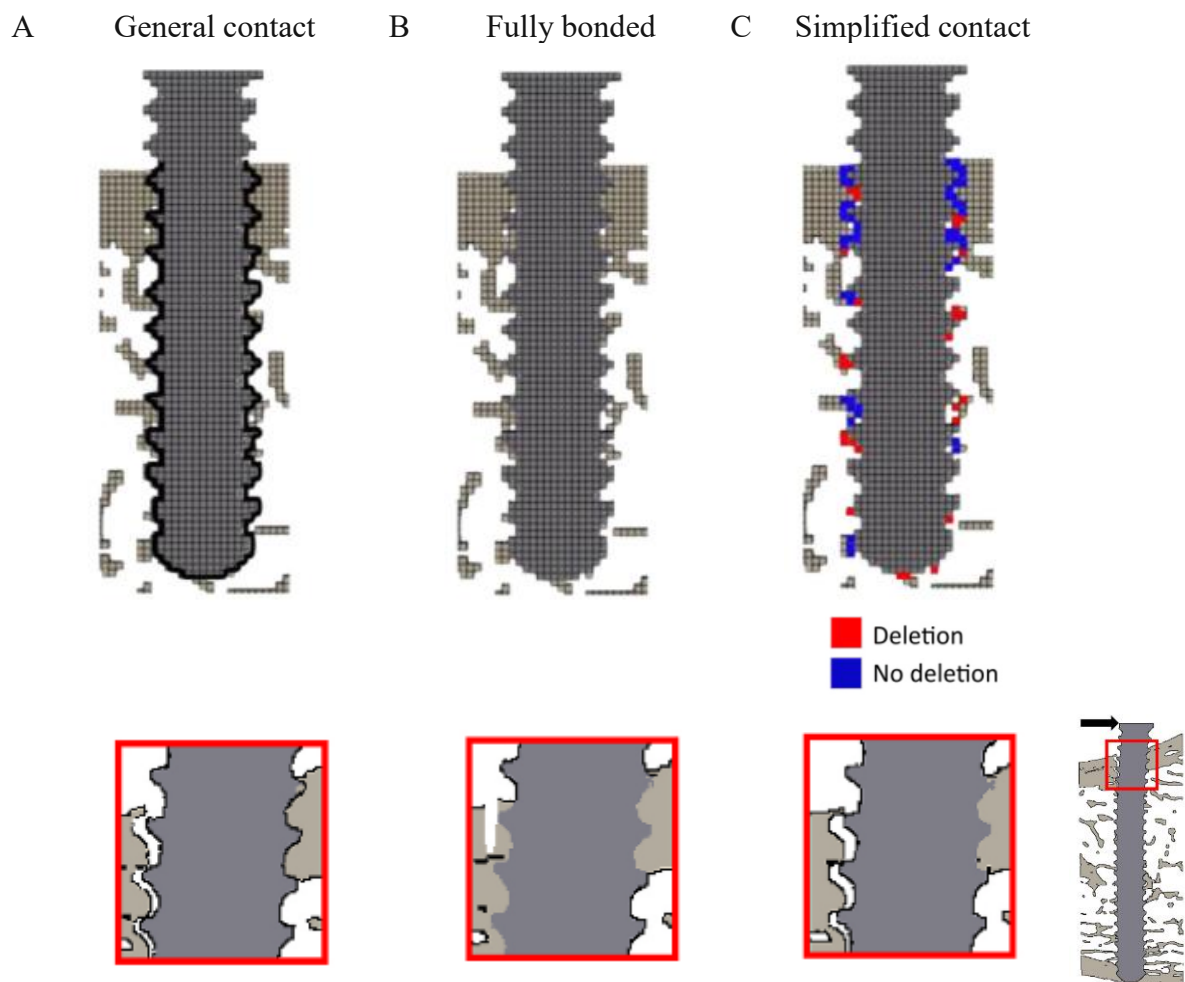
Fig. 1.8 Schematic illustration of different bone-screw contact models: (A) General-purpose contact, (B) fully bonded, and (C) simplified contact by deleting interface elements under positive volumetric strain following Steiner et al. [120].

1.3.4.6 Damage Due to Pre-Drilling and Screw Insertion in μFE Models
The pre-drilling of the pilot hole as well as the screw insertion process induce bone microdamage, as noted in several studies [67,138–141]. This accumulation of microdamage can compromise the primary stability of the screw, potentially resulting in screw loosening [142]. Consequently, accurate modelling is essential for reliable predictions of the mechanical properties of bone-screw systems. Steiner et al. [139] localized and quantified the screw insertion related pre-damage by comparing micro-CT scans of human femoral bone before and after screw insertion. Their findings revealed that the extent of the damaged region depends on the screw thread depth, with the most severe damage in the areas immediately adjacent to the screw. However, microdamage is influenced by multiple additional factors, including screw thread design, insertion technique (e.g. self-tapping vs. self-drilling) [143], and insertion torque [144]. A review of the literature identifies several approaches commonly used to model damage caused by screw insertion in bone-screw μFE models.

Simulation of Screw Insertion
Ovesy et al. [145] and Zhou et al. [146] incorporated the screw insertion process into the pre-drilled pilot hole in their simulations, enabling them to capture the progression of bone damage induced by screw insertion. This approach (see figure 1.9 (A)) allows for a more detailed representation of the mechanical effects at the bone-screw interface. However, it is computationally intensive, making it practical only for small-scale models. Additionally, in case pre-drilling is conducted in the experiments, this process might also need to be modeled in the simulations to achieve a correct estimation of pre-damage.

No Pre-Damage
Ovesy et al. [121] and Panagiotopoulou et al. [122] ignored pre-damage (see figure 1.9 (B)) resulting from screw-insertion in their μFE models. Despite this significant modelling simplification, their simulations demonstrated a strong 1:1 correspondence with experiments. However, even though the mechanical response can be captured with this approach, it is to be expected that the damage in the surrounding bone is not realistically represented.

Simplified Pre-Damage
To maintain computational efficiency, some studies defined damage zones around the screw with a uniformly reduced elastic modulus, effectively simulating the mechanical degradation of bone tissue due to screw insertion [115,120,137] (see figure 1.9 (C)). This approach simplifies the modelling process by avoiding the need to simulate the dynamic process of screw insertion while still accounting for the weakened properties of the bone in the peri-implant region. By adjusting the elastic modulus, researchers try to replicate the decrease in stiffness and load-bearing capacity of the bone near the screw threads. The size of the damage zones and the degree of modulus reduction vary among studies, with thinner zones reflecting localized damage and thicker zones accounting for broader mechanical impact. Similarly, the reductions in elastic modulus range from a few percent [115], representing subtle microdamage, to almost hundred percent [137], simulating severe local damage or a complete loss of structural integrity in the affected bone.

A   Simulation of screw insertion   B   No pre-damage   C   Simplified pre-damage
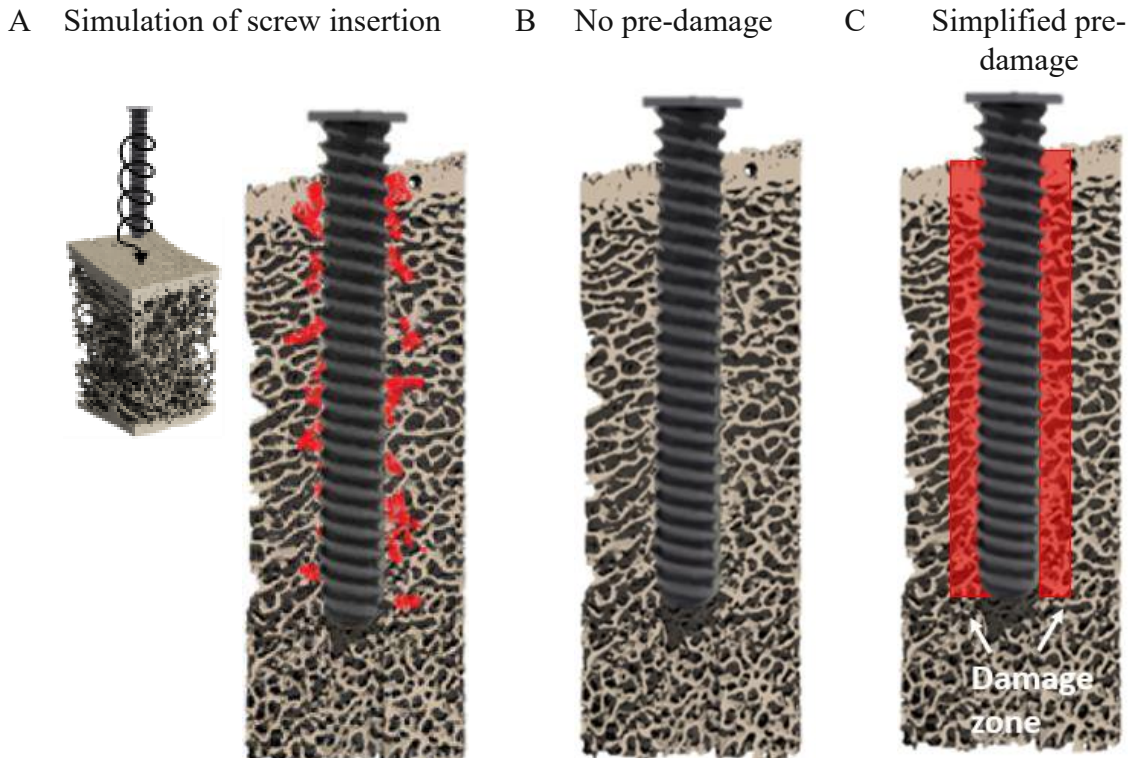
Fig. 1.9 Illustration of different pre-damage models: (A) simulation of screw-insertion and schematic illustration of resulting pre-damage, (B) no pre-damage, and (C) simplified pre-damage.

1.3.4.6 Dealing with Large Model Sizes in μFE Models

Regarding solid mechanics, a large number of μFE solvers exists which can solve μFE problems. They roughly be divided into two types: general purpose solvers (Abaqus (Dassault Systems, Vélizy-Villacoublay, France), Ansys (ANSYS, Inc., https://www.ansys.com/) that are versatile in application but lack computational efficiency, and specialized solvers (FEAP [23], Faim (Numerics88 Solutions Ltd, https://bonelab.github.io/n88/index.html), ParOSol [25], ParOSol-NL [24]) that show improved computational performance but are limited in model complexity. Given that μFE models often involve huge element numbers, selecting the appropriate solver depends critically on the specific requirements of the problem.

General-Purpose Solvers

General-purpose μFE solvers are designed to address a wide range of problems, from simple linear static analyses to complex nonlinear and dynamic simulations. They accommodate various nonlinearities (material, geometric, and contact) and offer extensive libraries of material models and element types [105,147]. Additionally, these solvers feature user-friendly graphical interfaces that simplify model setup and provide robust pre- and post-processing tools [105,147]. General-purpose solvers differ significantly from specialized solvers. In contrast to specialized solvers, they often rely on direct solvers, which can become resource-intensive for very large models [148]. Furthermore, direct solvers typically require the full assembly of the global stiffness matrix before solving, leading to high memory usage, especially in parallel computing environments [148]. A very commonly used general purpose solver for μFE simulations is Abaqus (Dassault Systems, Vélizy-Villacoublay, France) [122,145,146] which is briefly described in the following section.

Abaqus

Abaqus is a versatile general-purpose finite element analysis software that offers the modules Abaqus/Standard and Abaqus/Explicit. They refer to the two primary numerical approaches

offered by the Abaqus software package: implicit analysis (Abaqus/Standard) and explicit analysis (Abaqus/Explicit), each tailored for specific engineering applications [149]. Abaqus/Standard employs the Newton-Raphson method or its variants for solving nonlinear problems, with linear systems solved using a direct solver based on Gaussian elimination [105]. In contrast, Abaqus/Explicit employs an explicit time integration scheme, making it suitable for high-speed dynamics and large deformation applications [105].

The software offers a comprehensive element library, including solids, shells, and beams, and an extensive material library that supports linear and nonlinear elasticity, rubber, plasticity, and more [150]. Additionally, users can extend material capabilities by writing custom behaviour subroutines. Furthermore, it provides advanced tools for modelling contact and interface problems [150].

Specialized Solvers

Specialized large-scale µFE solvers are designed to efficiently handle high-resolution models with mesh sizes reaching several million elements. To achieve this, they typically employ iterative solvers, which significantly reduce memory usage and computational time compared to direct solvers [148]. A critical efficiency-enhancing strategy in these solvers is the use of a matrix-free approach [100]. Matrix-free methods are particularly advantageous for solving large systems due to their scalability [151]. Traditional approaches that assemble the global stiffness matrix often encounter bottlenecks in parallel systems, as they require extensive inter-processor communication [151]. In contrast, the element-level independence of matrix-free methods allows for efficient parallelization, minimizing communication overhead and ensuring better scalability as problem sizes increase [151]. Despite these advantages, the efficiency and scalability of specialized µFE solvers come with trade-offs. They generally support only linear-elastic or simple nonlinear material models, limiting their applicability to scenarios where such simplifications are valid. Additionally, these solvers are often restricted to a single element type to streamline computations and maximize performance. Two widely used specialized solvers FEAP [130,152,153] and ParOSol [120,154,155], will both be briefly introduced in the following sections.

FEAP/Olympus

FEAP (Finite Element Analysis Program) is a computational tool developed by Robert L. Taylor [23] for solving engineering problems using the FE method. Originally written in Fortran, the code is available on open access, making it accessible for adaptation and customization, particularly in research and educational settings [23,156]. It includes different types of elements, material models, and boundary conditions [23,156]. The solver enables to perform materially linear and nonlinear numerical studies, where an elasto-plastic material model is applied [130,152,157].

FEAP is a serial code, meaning it was originally designed to run on a single processor without parallel computing capabilities [158]. In order to improve scalability when handling very large problems, Olympus, a parallel finite element framework, was designed by integrating FEAP into a parallel computing environment [158]. In order to divide the problem into smaller sub-problems that can processed in parallel, Olympus uses a parallel graph partitioner called ParMetis [158]. To integrate FEAP within the parallel framework, Olympus uses an interface layer called pFEAP [158]. pFEAP manages the data exchange between FEAP's local instances and the global system handled by Olympus [158]. Each FEAP instance on a processor only processes the data relevant to its assigned subdomain, while pFEAP coordinates communication between subdomains as needed [158]. To solve the linear system of equations, Olympus uses Prometheus, a parallel algebraic multigrid solver [158].

Within the Olympus framework, FEAP benefits from advanced parallel computing techniques, making it efficient for µFE simulations. Nonetheless, the solver requires huge computational resources, with about 2.2kB memory per degree of freedom (DoF) [158], which is much higher than the memory requirements of the solver ParOSol (0.1kB) that is introduced in the next section [159].

ParOSol

The specialized solver ParOSol (Parallel-Octree-Solver) was initially developed by Flaig and Arbenz [25] is designed to achieve a low memory footprint and high scalability. Its low memory footprint optimizes resource utilization per DoF, while its exceptional scalability enables efficient use of thousands of processors, making it well-suited for large-scale simulations [159].

The low memory footprint can be achieved due to the special octree data structure, which efficiently stores the nodes and elements of the mesh [159]. This data structure allows to avoid to model void spaces, which significantly reduces memory consumption, by focusing computational resources only on regions that contain elements [159]. The octree-like data structure also forms the foundation of a geometric multigrid preconditioner that accelerates the solution process by promoting faster convergence [159]. Load balancing is achieved by dividing the octree into equally sized parts, ensuring that each processor handles an even portion of the computational workload, thus optimizing parallel performance and reducing idle time among processors [159].

The software, written in optimized object-oriented C++, avoids unnecessary memory allocation during all computation stages [159]. Parallelization is implemented using the Message Passing Interface (MPI), enabling efficient communication in distributed systems, while input and output operations rely on HDF5, a format optimized for managing large datasets and ensuring reliable data transfer [159].

While ParOSol excels in performance and scalability, it comes with limitations due to its specialized design. The solver supports only hexahedral elements, simplifying its algorithms but restricting flexibility for complex geometries [159]. The mesh is generated internally, preventing external customization or refinement [159]. Furthermore, all elements must share the same Poisson's ratio, limiting its ability to model materials with varying properties [159]. Additionally, ParOSol supports only linear-elastic material behaviour, reducing its applicability to simulations requiring complex nonlinear responses [159].

ParOSol-NL

ParOSol was initially developed to handle only linear-elastic simulations. Stipsitz et al. [24] enhanced the solver to ParOSol-NL, which enables materially nonlinear simulations. This upgrade allows for more realistic modelling of damage and fracture at the tissue level, providing insights into how materials fail under load. Additionally, it enables the direct determination of the maximum force of a structure [26]. However, the extension does not account for other types of nonlinearities, such as geometric and contact nonlinearity, limiting its applicability to cases where these effects can be neglected [26].

A simple damage-based nonlinear material law was carefully integrated into ParOSol to preserve the efficient parallel properties of the original solver [26]. To achieve good scalability, minimization of inter-process communication was considered in the implementation process [26]. By reducing the need for data exchange, high computational efficiency even when scaling to large numbers of processors were maintained [26].

The solution of materially nonlinear problems is carried out using an incremental-iterative procedure [26]. The external load is applied incrementally, with each load step being solved through iterative applications of the original linear ParOSol solver [26]. Within each iteration, the elastic moduli are held constant, and once the linear problem is resolved, trial stresses are computed for each element [26]. If the calculated stress state falls outside a pre-defined quadric damage onset surface, the solver adapts the elastic modulus and updates the damage variable for each element [26]. This element-wise update simplifies the implementation and helps to maintain the solver's efficiency [26]. Increment convergence is determined when both global and local steady-state conditions are met [26].

1.3.5 Verification and Validation of µFE Models

This chapter presents an overview of the concepts of verification and validation of computational models. It subsequently focuses on the process of experimental validation of µFE models at the macroscale (several millimeters or larger), outlining its key stages. Finally, the chapter discusses the procedure of validating a µFE model using the DVC method, which is currently the most promising method to validate µFE models below the macroscale.

1.3.5.1 Verification and Validation of Computational Models

The verification and validation process provides evidence that a computer model produces results with sufficient accuracy for its intended use [160]. However, it does not guarantee the model's accuracy under all possible conditions [160]. Verification and validation is achieved when the required level of accuracy for the specific scenario is satisfied [160]. Verification ensures that the computational model is mathematically correctly implemented and solves equations accurately [161]. In contrast, validation focuses on determining whether the model accurately represents the real-world phenomena by comparing its results to experimental data and assessing the appropriateness of assumptions and simplifications [161].

The verification and validation plan of the American Society of Mechanical Engineers (ASME) (see figure 1.10) provides a systematic framework for evaluating computational models [161]. The process begins with defining the problem statement, which identifies the objectives, physical phenomena, and boundary conditions to ensure alignment with the intended application [161]. A conceptual model is then developed, simplifying the system into key components and processes, serving as a foundation for the subsequent mathematical and physical models [161]. The mathematical model formalizes the relationships in the conceptual model through equations, which are implemented in algorithms and software to produce the computational model [161]. Code verification ensures the correct implementation of equations, while calculation verification assesses numerical accuracy, stability, and convergence of simulation results [161]. Simultaneously, a physical model is developed alongside an experimental design that defines test variables, conditions, and data collection methods to generate experimental data representing system behaviour [161]. Uncertainty quantification evaluates sources of variability in both simulations and experiments, providing confidence bounds and ensuring reliable comparison [161]. The validation process compares simulation outcomes with experimental data to assess the computational model's fidelity [161]. Acceptable agreement validates the model [161]. Otherwise, the mathematical model, computational implementation, or experimental setup must be refined [161].
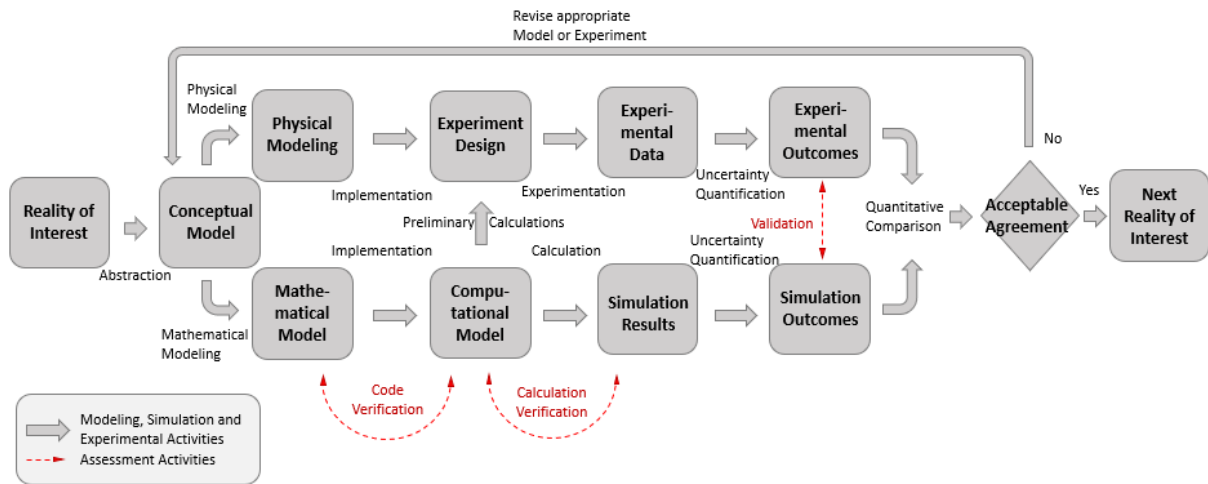
Fig. 1.10 Graphical illustration of the verification and validation activities and outcomes similar to Schwer [161].

1.3.5.2 Verification of µFE Models

The verification process is divided into code verification and calculation verification [160]. Code verification ensures that the software functions as intended by addressing two main areas [160]. First, software quality assurance detects programming errors while ensuring that the code produces consistent results across different hardware, operating systems, and compilers [160]. Second, numerical algorithm verification involves creating test problems with known analytical solutions and comparing these to the outputs of the code to confirm the correctness of the numerical methods [160]. Calculation verification, on the other hand, focuses on quantifying errors in numerical simulations, introduced by discretization [160]. This is typically done through mesh-refinement studies, which analyse how the solution converges as the grid is refined [160].

1.3.5.3 Validation of µFE Models at the Macroscale

Validation of µFE models at the macroscale (several millimeters or larger) is a crucial step to ensure that these models accurately predict the apparent or structural mechanical behaviour of bone biopsies up to whole bones with implants. The typical process of validating µFE models of bones and bone-screw systems at the macroscale involves several key stages. First, a representative set of cadaver bones is selected, carefully prepared, and subjected to high-resolution scanning to capture the bone microstructure [18]. Next, mechanical experiments are performed on these specimens to measure their apparent mechanical properties, such as stiffness and strength, under controlled loading conditions [18]. Simultaneously, µFE simulations are designed based on the previously recorded µCT scans, replicating the experimental setup as closely as possible by incorporating similar boundary conditions, loading scenarios, and material properties [18]. Finally, the outputs of the simulations are compared to the experimental results to assess the model's predictive accuracy, often using statistical metrics like the coefficient of determination (R^2) or mean absolute error (MAE). Successful validation requires a strong correlation between the experimental and simulated data, demonstrating that the µFE model can reliably replicate the mechanical response of bone at the macroscale [18]. Figure 1.11 illustrates a typical validation process of µFE predicted apparent properties of bone-screw systems following the verification and validation plan.
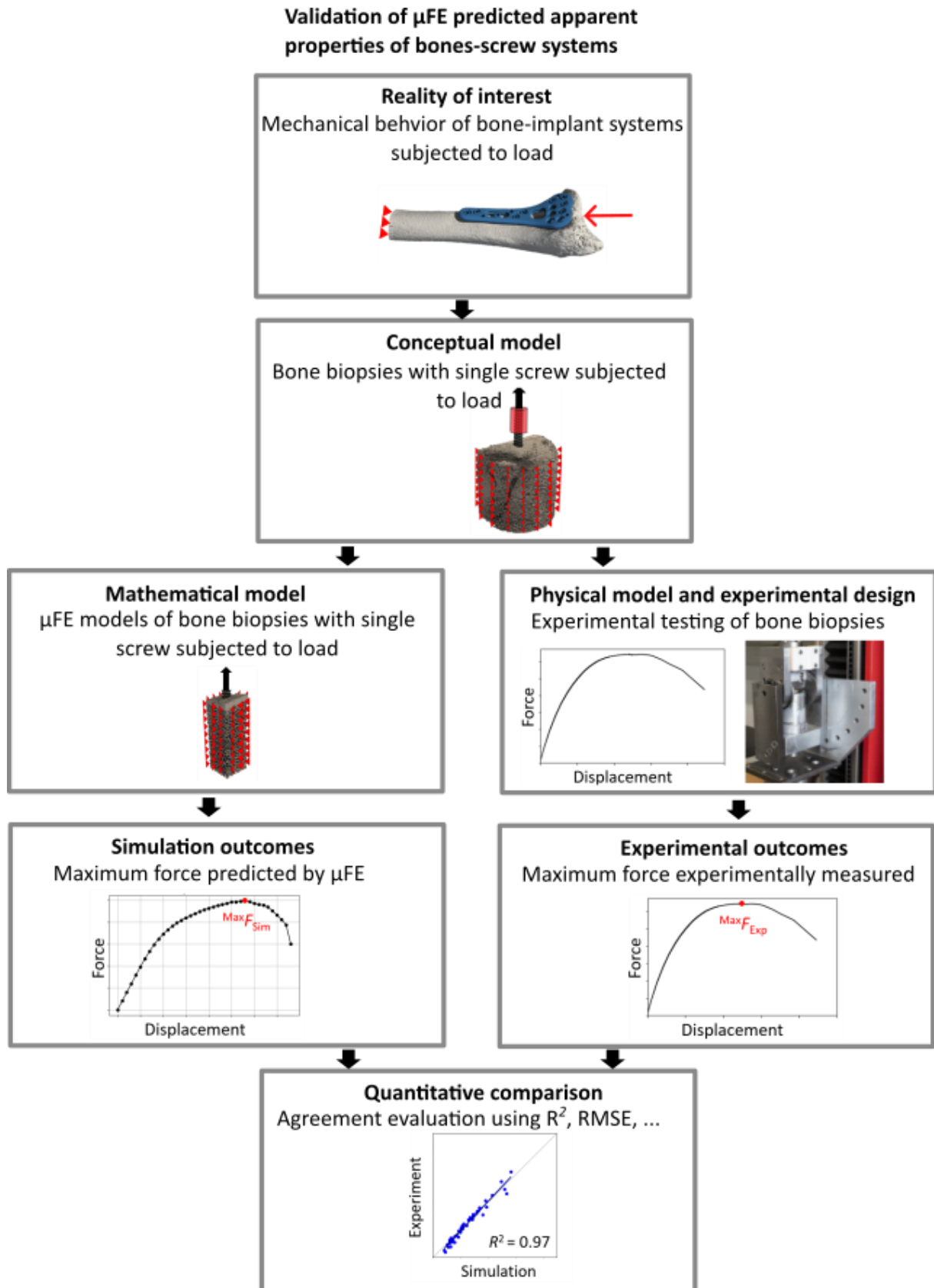
Fig. 1.11 General workflow for a macroscale validation of bone-screw µFE models following the verification and validation plan of ASME [161].

The agreement between µFE outcomes and experimental results is influenced by several factors. An important factor is the appropriate selection of bone material properties, such as the Young's modulus. While there is considerable variation in the values used across different studies, using

a well-calibrated Young's modulus that aligns with the actual bone tissue properties of the physical model can significantly enhance the agreement between µFE and experiment [18]. The experimental setup plays a critical role as well. Controlled experiments, such as those involving the embedding of isolated bone segments [162], allow for better control over boundary conditions, minimizing external variables that can affect results. This approach leads to more reliable µFE predictions, as it closely replicates the conditions under which the bone would experience mechanical loads [18]. However, it is equally important to ensure that the experimental setup remains aligned with the reality of interest [163]. It should not be too far removed from the actual scenario being studied, as this can compromise the model's relevance.

1.3.5.4 Validation of µFE Models at the Mesoscale

Validation of µFE models at the macroscale assesses prediction accuracy of µFE models at the apparent level, but it cannot estimate prediction accuracy of mechanical properties at smaller, localized scales. To address this limitation, DVC, initially introduced by Bay et al. (1999) [164], has emerged as a valuable technique for validating µFE models at mesoscale levels. Shortly, DVC tracks the deformation of internal features by comparing the volumetric images of the undeformed and deformed state and uses this information to compute the local displacements and strains across the entire 3D volume of biological tissues [165]. For image resolutions of about 30µm, the DVC displacement field is typically measured in a regular grid with a spacing of approximately 0.5–2mm [166]. Figure 1.12 illustrates a typical validation process of µFE predicted displacement fields at the mesoscale following the verification and validation plan.

The accuracy and precision of displacement and strain fields calculated by DVC depend on several factors, notably the quality of input images and the tissue's microstructural heterogeneity [167]. Poor image quality, caused by low signal-to-noise ratios or insufficient resolution, hinders the algorithm's ability to track intensity patterns, reducing reliability. Tissue microstructure also plays a critical role as homogeneous structures like cortical bone produce uniform intensity patterns that are harder to track, while the heterogeneity of trabecular bone offers distinct patterns that improve detection [168]. Another critical factor affecting DVC performance is the choice of nodal spacing on the superimposed grid. Increasing nodal spacing generally leads to an increase in accuracy and precision, following a power-law relationship [166].

The DVC method is widely used to validate µFE model predictions, primarily for displacement measurements due to the lower accuracy of strain calculations [107,119,124,169,170]. In these validation studies, DVC employs deformed and undeformed images of bone structures to measure the displacement and strain fields. The undeformed image serves as the basis for generating a µFE model, where the displacement field measured by DVC is applied at the boundaries. Since DVC measures displacements on a coarser grid than the µFE model, different approaches are used for comparison, such as pointwise comparison (interpolating µFE results to DVC points) [107,119] or volume averaging (averaging µFE results for corresponding DVC grid nodes) [171].
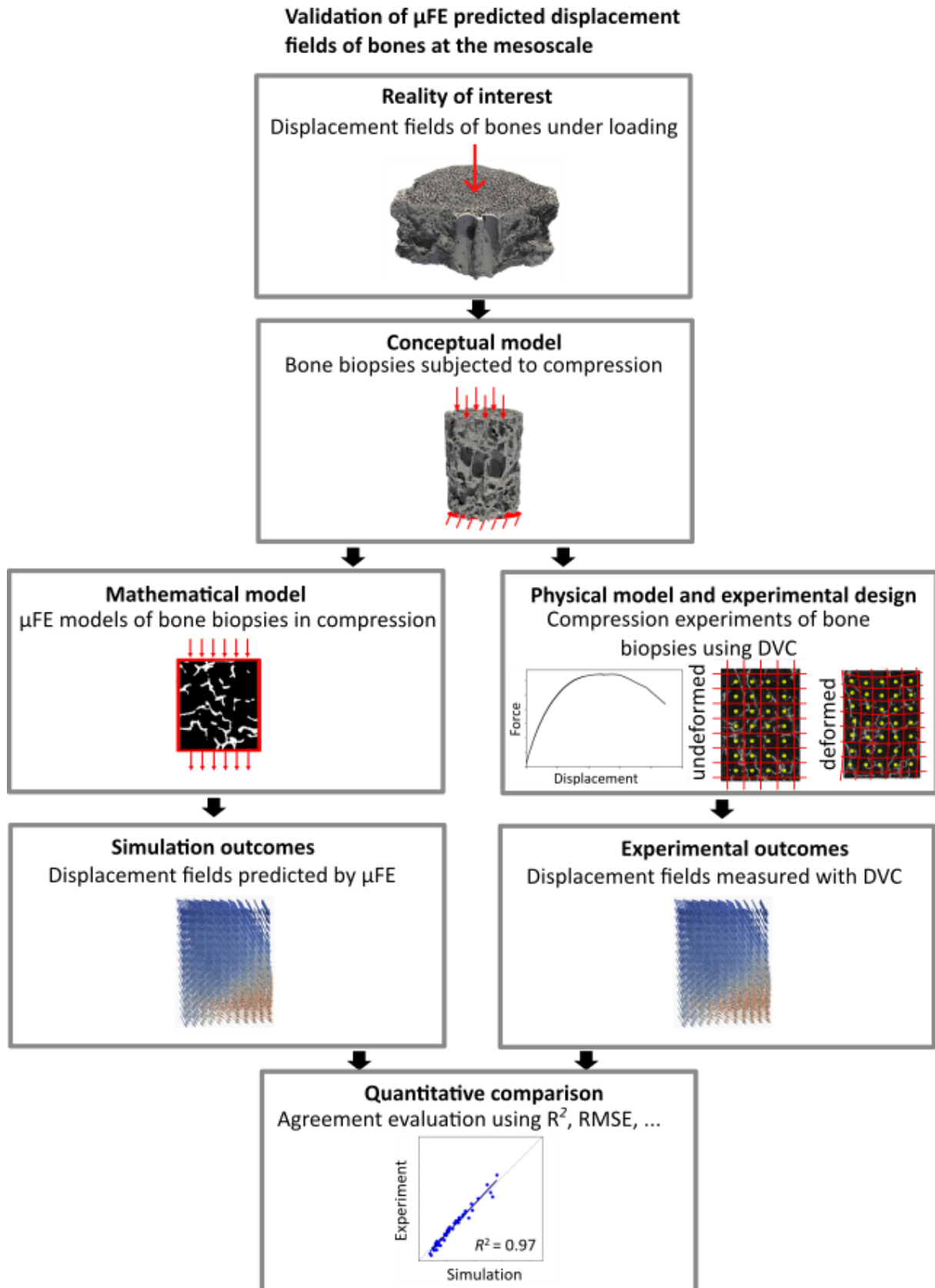
Fig. 1.12 General workflow for a mesoscale validation of bone μFE models following the verification and validation plan of ASME [161].

1.4 Summary of Publications and Contributions

Chapters 2, 3, and 4 present individual research studies that contribute to the overarching aims of this thesis and have been previously published:

Chapter 2:   Stefanek, P., Synek, A., Dall'Ara, E. & Pahr, D. H. (2022). Comparison of linear and nonlinear stepwise µFE displacement predictions to digital volume correlation measurements of trabecular bone biopsies. *Journal Of The Mechanical Behavior Of Biomedical Materials/Journal Of Mechanical Behavior Of Biomedical Materials*, *138*, 105631. https://doi.org/10.1016/j.jmbbm.2022.105631

Chapter 3:   Stefanek, P., Pahr, D. H. & Synek, A. (2024). Comparison of simplified bone-screw interface models in materially nonlinear µFE simulations. *Journal Of The Mechanical Behavior Of Biomedical Materials/Journal Of Mechanical Behavior Of Biomedical Materials*, *157*, 106634. https://doi.org/10.1016/j.jmbbm.2024.106634

Chapter 4:   Stefanek, P., Silva-Henao, J. D., Fiedler, V., Reisinger, A. G., Pahr, D. H., & Synek, A. (2025). Screw pull-out force predictions in porcine radii using efficient nonlinear µFE models including contact and pre-damage. *Frontiers in Bioengineering and Biotechnology*, *13*. https://doi.org/10.3389/fbioe.2025.1524235

The author of this thesis was the first author of all three publications. According to the CRediT taxonomy (https://credit.niso.org/), the first author contributed to these publications by data curation, the investigation, the methodology, the project administration, the visualization, and the writing of the original draft.

Chapter 2 focuses on validating ParOSol-NL at the sub-macroscale level. Chapter 3 introduces the development of an efficient and accurate contact model tailored for bone-screw simulations within ParOSol-NL. Finally, Chapter 4 integrates two subgoals: first, an efficient pre-damage model is implemented to represent bone damage caused by the screw insertion process; second, the enhanced ParOSol-NL solver is applied to bone-screw simulations with simplified contact and pre-damage. These simulations are evaluated by comparing the predicted bone-screw pull-out forces against experimental results. The three publications and their main outcomes are summarized in the following.

1.4.1 Comparison of linear and nonlinear stepwise µFE displacement predictions to digital volume correlation measurements of trabecular bone biopsies

Local displacements from trabecular bone biopsies under stepwise compressive loading predicted with linear and nonlinear µFE models were compared to DVC measurements at a specific load step in the elastic regime as well as at the ultimate load. The µFE models showed good agreement with the DVC measurements, supporting the validation of ParOSol-NL for sub-macroscale displacement predictions (0.864mm x 0.864mm x 0.864mm). At the linear load step, both linear and nonlinear µFE models demonstrated comparable accuracy in predicting displacement fields. At the ultimate load step, nonlinear µFE simulations yielded a slightly more accurate correlation with DVC-measured displacements, but also introduced a substantial increase in computational costs in comparison to linear simulations.

1.4.2 Comparison of simplified bone-screw interface models in materially nonlinear µFE simulations

Three different efficient and simplified bone-screw interface modelling approaches were compared to the general contact algorithm of the general purpose µFE solver Abaqus/Explicit. The simple nonlinear material model of ParOSol-NL was implemented in Abaqus/Explicit to allow a direct comparison of different interfaces. Multiple load cases (push-in/pull-out, shear) and variations of single screw-bone constructs (low/high density human radius bone, different screw insertion depths) were considered. Fully bonded interface models overestimated both whole-construct stiffness and maximum force, and resulted in unrealistic damage patterns. Thus, it was concluded that accurate physical contact modelling is essential for bone-screw µFE modelling if these quantities shall be predicted accurately. Simplified and efficient interface models, based on tensionally strained element deletion (TED) following those developed by Steiner et al. [120] resulted in improved accuracy in predicting mechanical responses of the bone-screw interface in comparison to the fully bonded interface. A modified version of the TED interface, TED-M, was introduced to account for changes in the contact area during the simulation. The original version of TED produced the lowest errors in predicting whole-construct stiffness, while TED-M excelled at accurately estimating maximum force. Both models also offered improved prediction of damage distributions in comparison to the fully bonded interface, providing a more realistic assessment of damage patterns. Since both TED and TED-M enable straightforward implementation in the µFE solver ParOSol-NL, efficient and accurate bone-screw contact models for the specialized solver were found.

1.4.3 Screw pull-out force predictions in porcine radii using efficient nonlinear µFE models including contact and pre-damage

Screw pull-out force predictions of porcine biopsies were conducted using µFE models that included both a simplified bone-screw interface model of the previous study (see chapter 1.4.2) as well as a screw insertion related pre-damage model. Pre-damage was applied in a manner consistent with previous research, by defining a small damage zone around the screw where the damage value was set to a certain predefined value. The damage zone was parametrized by its radial thickness around the screw and the damage values assigned. A plausible set of pre-damage parameters was found by iterative adaptation to match the experimental results. However, the solution was not unique, i.e. multiple parameter sets would provide a good fit with respect to the experimental data. Further refinement of the pre-damage model would necessitate additional experimental data on pre-damage distribution.

Interestingly, good correlations of µFE and experimental screw pull-out force could be achieved even when assuming a fully bonded interface and without integrating pre-damage factors. However, the values obtained were not quantitatively accurate. Achieving quantitatively accurate results depends on the careful integration of various factors: contact modelling, material property selection, and pre-damage parameters. Each of these components plays a critical role in capturing the complex biomechanical interactions and failure modes accurately.

1.5 Scientific Contribution

This thesis constitutes a significant advancement in the biomechanical modelling of bone and bone-screw systems at the microscale using µFE simulations. It introduces computationally efficient methods to address the challenges of bone-screw interface interactions and the effects of pre-damage caused by pre-drilling and screw insertion. These methods achieve a critical balance between predictive accuracy and computational cost, enabling high-fidelity biomechanical analyses with reduced resource demands.

A central outcome is the enhancement of ParOSol-NL as a computationally efficient, materially nonlinear µFE simulation framework. The reliability of ParOSol-NL in accurately predicting displacement fields of bone at the mesoscale was demonstrated, establishing it as a robust tool for analyzing deformation patterns even close to the point of failure. Implementing a simplified screw-contact and pre-damage model extend the applicability of ParOSol-NL to use cases involving bones with screw-anchored implants. Comparison to experimental measurements highlights the accuracy of this approach while maintaining computational efficiency for this new field of application. In summary, ParOSol-NL has emerged as a particularly valuable tool for orthopedic research, offering promising applications in analyzing the mechanical behaviour of bone, conducting preclinical testing of implants, and optimizing implant designs.

This research lays the groundwork for more feasible and accessible large-scale µFE simulations, such as those of entire bones or complete bone-screw systems. These advancements hold the potential to significantly enhance biomechanical analyses, advancing the understanding of bone mechanics, improving orthopedic treatment strategies, and driving innovation in medical device design for better clinical outcomes.

Chapter 2

Paper 1

Comparison of linear and nonlinear stepwise µFE displacement predictions to digital volume correlation measurements of trabecular bone biopsies

Pia Stefanek, Alexander Synek, Enrico Dall'Ara, Dieter H. Pahr

Abstract

Digital volume correlation (DVC) enables to evaluate the ability of µFE models in predicting experimental results on the mesoscale. In this study predicted displacement fields of three different linear and materially nonlinear µFE simulation methods were compared to DVC measured displacement fields at specific load steps in the elastic regime ($Step_{El}$) and after yield ($Step_{Ult}$). Five human trabecular bone biopsies from a previous study were compressed in several displacement steps until failure. At every compression step, µCT images (resolution: 36µm) were recorded. A global DVC algorithm was applied to compute the displacement fields at all loading steps. The unloaded 3D images were then used to generate homogeneous, isotropic, linear and materially nonlinear µFE models. Three different µFE simulation methods were used: linear (L), nonlinear (NL), and nonlinear stepwise (NLS). Regarding L and NL, the boundary conditions were derived from the interpolated displacement fields at $Step_{El}$ and $Step_{Ult}$, while for the NLS method nonlinear changes of the boundary conditions of the experiments were captured using the DVC displacement field of every available load step until $Step_{El}$ and $Step_{Ult}$. The predicted displacement fields of all µFE simulation methods were in good agreement with the DVC measured displacement fields (individual specimens: $R^2 > 0.83$ at $Step_{El}$ and $R^2 > 0.59$ at $Step_{Ult}$; pooled data: $R^2 > 0.97$ at $Step_{El}$ and $R^2 > 0.92$ at $Step_{Ult}$). At $Step_{El}$, all three simulation methods showed similar intercepts, slopes, and coefficients of determination while the nonlinear µFE models improved the prediction of the displacement fields slightly in all Cartesian directions at $Step_{Ult}$ (individual specimens: L: $R^2 > 0.59$ and NL, NLS: $R^2 > 0.68$; pooled data: L: $R^2 > 0.92$ and NL, NLS: $R^2 > 0.94$). Damaged/overstrained elements in L, NL, and NLS occurred at similar locations but the number of overstrained elements was overestimated when using the L simulation method. Considering the increased solving time of the nonlinear µFE models as well as the acceptable performance in displacement prediction of the linear µFE models, one can conclude that for similar use cases linear µFE

models represent the best compromise between computational effort and accuracy of the displacement field predictions.

Keywords: Micro Finite Element Model, Materially Nonlinear Simulation, Digital Volume Correlation, Displacement, Trabecular Bone Biopsies

2.1 Introduction

Bone has a complex, hierarchical structure that spans multiple length scales [27]. Since all scales are contributing to the mechanical behaviour of bone, understanding bone failure still remains challenging. Especially research concerning the link between failure mechanisms of bone acting at different length scales is still incomplete [29].

Over the past 30 years, with the increase of computational power and the improvement of imaging techniques, computational modelling has been established as a popular tool to non-invasively predict the mechanical properties and failure processes of bone [100,172–174]. Due to tremendous improvement in resolution, micro computed tomography (µCT) scanners are nowadays able to capture the bone architecture at the micro scale (~30µm resolution) and even below. For this reason, micro finite element (µFE) models represent a non-invasive addition to lab-experiments to investigate the mechanical behaviour of bone under loading at the microscale. In most micro finite element (µFE) studies so far, bone is modelled using a linear-elastic material law [18,111,175,176]. But such analyses cannot be used to simulate deformations beyond the elastic limit, which occur for example when bone fractures. In order to predict failure behaviour, a nonlinear material law is required.

Since bone exhibits several mechanisms such as plasticity, damage, viscosity, and creep in the post-yield regime, a wide range of different constitutive models have been developed [24,126,128]. Each of these models is formulated for a limited range of applications (e.g. trabecular/cortical bone, whole bone/single trabeculae, small/large strain, etc.) in which it is capable to replicate the real mechanical behaviour with acceptable accuracy [118]. However, a tradeoff between computational efficiency and the complexity of the implemented material model must be found to enable feasible runtimes of the µFE simulations. Most general-purpose FE solvers (e.g. Abaqus, Ansys) are able to account for different types of nonlinearity (geometric [177], material [129] and contact nonlinearity [145] but are only a viable option for model sizes up to a few millions of elements. For example, Ding et al. [178] needed 310 CPU hours to solve a nonlinear simulation of a trabecular bone model with 0.7million elements with Abaqus/Standard. Increasing model sizes further raise computational requirements and make the use of a supercomputer essential. Highly specialized software generated to solve large-scale problems (e.g. FEAP [23], Faim (Numerics88 Solutions Ltd, https://bonelab.github.io/n88/index.html), ParOSol [25], ParOSol-NL [24] have better parallel execution performance but are generally based on linear-elastic or very simple nonlinear material models. For example, ParOSol-NL is able to solve even very large nonlinear models with up to a few hundreds of million elements in approximately 5500 CPU hours [179].

Before their application, the µFE models have to be validated against accurate experimental measurements. For instance, apparent properties (e.g. stiffness, strength) can be compared directly to experimental measurements from standard monotonic mechanical testing [24,123,180,181]. Experimental validation of local predictions was recently made possible by using Digital Volume Correlation (DVC). Given µCT images of the unloaded and the loaded specimens, DVC is able to measure the 3D displacement field, which can be compared to the µFE model predicted displacement field. However, for image resolutions of about 30µm the

DVC displacement field is typically measured in a regular grid with a specific spacing of approximately 0.5 to 2mm [166]. Thus, "local" displacements typically define displacements of volumes of this size which is rather a meso than a micro quantity.

In the last years, DVC was successfully applied multiple times to get more insight into strain distributions [182,183] and fracture patterns [184–186] of bone. Furthermore, several studies evaluated the agreement between FE predicted displacements and DVC measured displacements in the elastic and in the nonlinear regime. Zauel et al. [170] showed an excellent correlation in µFE displacements of cancellous uniaxially loaded bone biopsies only in axial loading direction while other studies reported excellent agreements with DVC data in all directions (R^2>0.86) [107,119]. In a recent study, very good agreement has been found between µFE and DVC displacements for very complex vertebral bodies with induced focal lesions (R^2>0.84) [169]. Oliviero et al. [124] were able to replicate the DVC displacement field in the nonlinear regime using linear µFE models (R^2>0.76). Jackman et al. [184] compared predicted displacements of nonlinear quantitative computed tomography (QCT) based FE models to DVC measured displacements in the nonlinear regime. The correlation results were only moderate with coefficients of determination ranging between 0.06 and 0.77. Madi et al. [187] applied a nonlinear material model to a scaffold implant material made of 85:15 poly(D,L-lactide-co-glycolide) and were able to replicate the displacement field up to 3% strain. To the author's knowledge, only one recent study has yet compared displacements predicted by nonlinear µFE to DVC measured displacements in bone. Peña Fernández et al. [188] successfully replicated the DVC displacement field (R^2>0.79) up to 3% nominal strain. Their µFE models were solved with the commercial solver Abaqus/Standard with the benefit of a complex material law including geometrical nonlinearity and the drawback of low computational efficiency.

The aim of this study was to compare the displacement predictions of three different linear and materially nonlinear µFE simulation methods using the highly efficient µFE solver ParOSol-NL in both pre- and post-yield loading stages. To examine the validity of the predicted displacement fields, their agreement to DVC displacements measured from compressive tests of human trabecular bone biopsies was evaluated.

2.2 Materials and methods

Figure 2.1 shows the outline of this study. In brief, human trabecular bone biopsies from a previous study were compressed in several displacement steps until failure. At every loading step, µCT images were recorded. A non-rigid registration was applied to the images to get the displacement fields at all loading steps until failure. The unloaded 3D images were then used to generate linear and materially nonlinear µFE models. Three different µFE simulation methods were compared: linear (L), nonlinear (NL), and nonlinear stepwise (NLS). Finally, the displacement fields predicted by the µFE models were compared to the DVC displacement fields at a specific load step in the elastic regime and at the ultimate load step.

2.2.1 Experimental data

The study is based on experimental data of five randomly selected human trabecular bone biopsies (see Fig. 2.2) which were used in a previous study [189]. The five selected cylindrical biopsies, which were extracted from the thoracic and lumbar spine, measured about 11mm in height and 8mm in diameter and had a mean relative bone volume fraction (BV/TV) of 14%. Their morphometrics were evaluated with the software Medtool (v4.5, Dr. Pahr Ingenieurs e.U., Pfaffstätten, Austria)(Table 2.1). In the original study, nominal uniaxial compression experiments were performed on each specimen using a custom loading device inside a SCANCO µCT 40 (SCANCO Medical AG, Brüttisellen, Schweiz) machine (see Fig. 2.1A). An

axial load was applied manually using a screw and was measured with a loadcell (HBM Type C9B 2kN). While the samples' bottom surface was fixed using epoxy glue to ensure fully clamped boundary conditions, the top surface of the samples was glued to a uniaxially moving part. Displacement-controlled loading was applied in a stepwise manner (nominal displacement step size: 0.03mm-0.072mm) until failure. The specimens were scanned in the preloaded configuration (1-4N) and at every loading step with a resolution of 36µm. In order to reduce relaxation-effects during the scan, the µCT image acquisition was started approximately 30min after load application. The scanning parameters were: voltage of 70000V, current of 114µA, projection number of 250 and exposure time of 200ms. Compared to the original study, only steps until a drop of force were considered (see Fig. 2.1A $Step_{Ult}$). The number of used loading steps varied between five and seven. At $Step_{Ult}$, the specimens reached loads between 21.6N and 90.48N and were compressed with apparent strain from 1.8% to 3% (see Fig. 2.3). In addition to the gray value images obtained from the µCT scanning also segmented images of every loading step were available from the previous study [189]. They were generated by applying single level thresholding on the smoothed (Gauss filter with $\sigma = 0.8$ and a kernel size of 3x3x3) grey-value images.
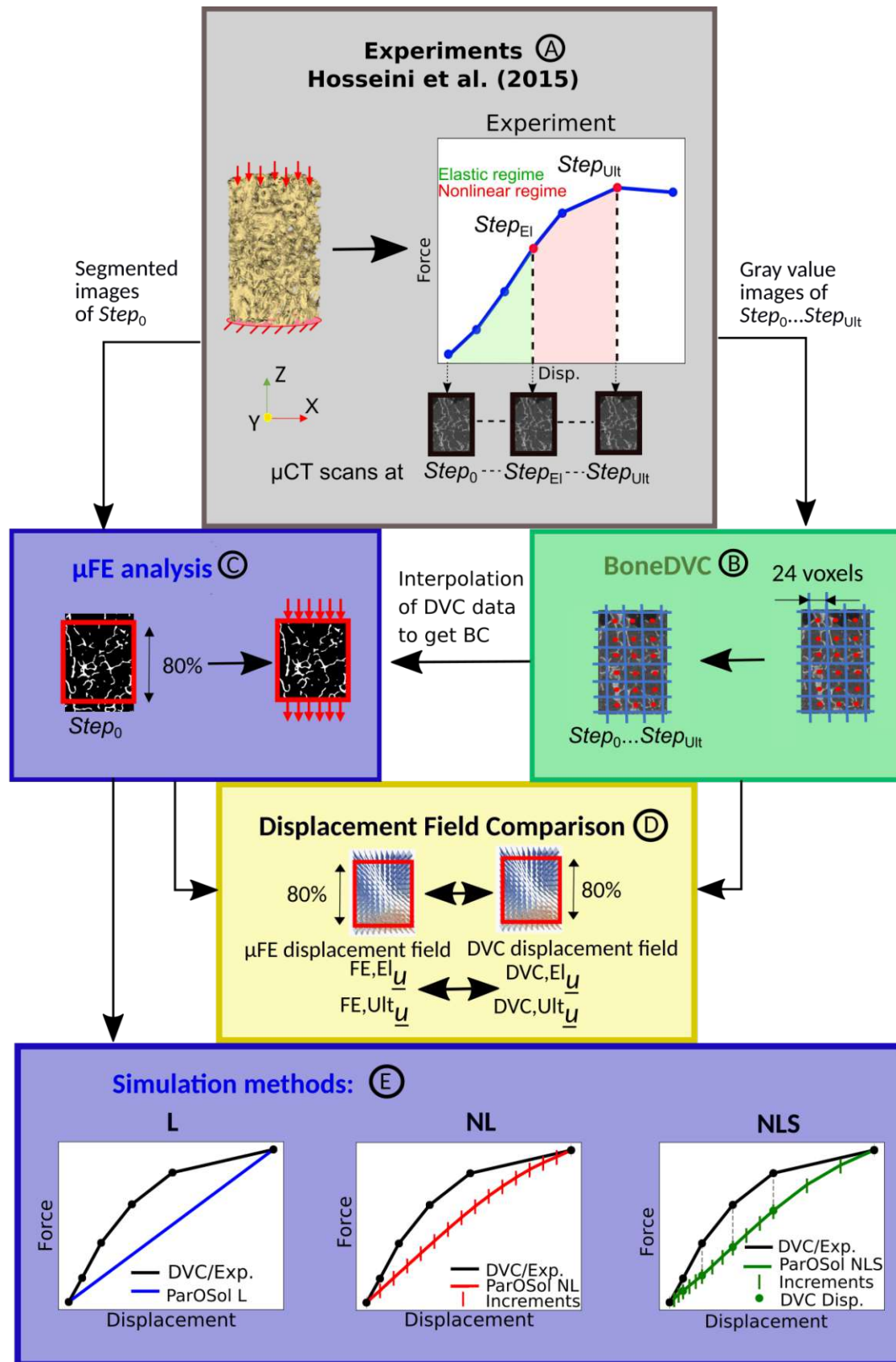
Fig. 2.1 Complete workflow of the study. A. Stepwise compression experiments from Hosseini et al. [189]. B. Application of BoneDVC algorithm on the gray value images. C. µFE analyses of the middle 80% of the preloaded segmented images. D. Displacement field comparison: µFE predicted vs. DVC measured. Only the middle 80% of the µFE models were evaluated corresponding to 64% of the original specimen height. E. Overview of the simulation methods: L, NL, and NLS.

Table 2.1
Dimensions and morphometrics of the five bone specimens (A3-D6) used in this study.

Specimen ID	Diameter in mm	Height in mm	BV/TV in %	Tb.N in 1/mm	Tb.Th* in µm	Tb.Sp* in µm
A3	8.1	11.556	13.6	0.85	181±45	1002±402
D2	8.172	11.88	19.9	1.04	181±51	783±279
D3	8.064	11.592	11.3	0.8	178±45	1067±414
D5	8.064	11.808	8.6	0.68	181±48	1285±511
D6	8.064	11.808	16.7	0.99	174±40	832±306

*mean ± standard deviation

Note: bone volume fraction (BV/TV), trabecular number (Tb.N), trabecular thickness (Tb.Th), trabecular separation (Tb.Sp)

Fig. 2.2 Experimental force-displacement curves of all analysed specimens A3 to D6. The given force values describe the forces after relaxation.

Fig. 2.3 3D representation of the five selected human trabecular bone biopsies A3 to D6.

2.2.2 Digital volume correlation

The DVC displacement field of every loading step was computed over the entire volume using a global DVC algorithm (BoneDVC, https://bonedvc.insigneo.org/dvc/) (see Fig. 2.1B and Fig. 2.4). Details about the algorithm are reported in multiple publications [166,168,190]. Briefly, a cubic grid with a selected grid spacing (GS) (previously referred to as nodal spacing (NS) in Dall'Ara et al. [168] and other literature) is superimposed on the 3D gray value images. Then, elastic registration is applied to the preloaded and deformed images using the Sheffield Image Registration Toolkit (ShIRT). The software solves the registration equations at the nodes of the grid using trilinear interpolation between the nodes. In this study a GS of 24 voxels (0.864mm) was selected following previous studies that used the same global DVC approach on µCT

images of bone with similar scanning resolutions, which reported displacement precision below 2.5μm [191–193]. In order to exclude boundary effects of the experiment only the middle 80% of the DVC displacement field were considered for further processing. Boundary effects arise from artefacts of the experimental setup and could lead to high measurement errors in the regions close to the boundary. Since this effect diminished farther away from the boundary, a general practice is to exclude the edge parts from the experimental evaluation [119,124,169].
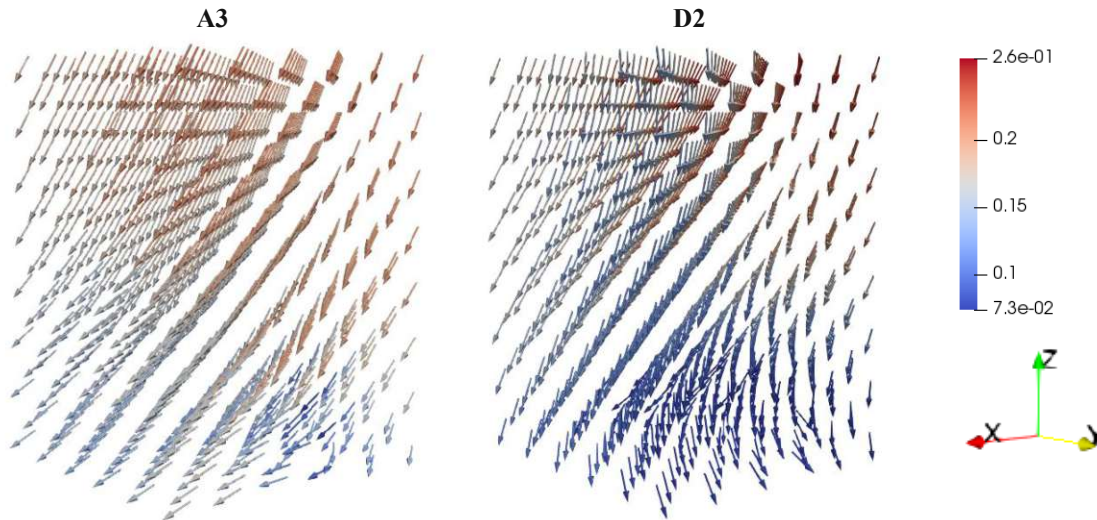
Fig. 2.4 3D representation of the DVC measured displacement field at the ultimate load step of two representative specimens (A3 and D2).

2.2.3 μFE modelling

The segmented μCT images of each specimen were cropped (middle 80% of height) and μFE models were created from the images in the preloaded configuration (see Fig. 2.1C). All voxels were converted into 8-noded hexahedral elements and isotropic, homogeneous material properties were assigned. According to Stipsitz et al. [24] an elastic modulus of E_0=10GPa was selected for the bone voxels but it was reduced to E_0=2GPa in order to account for the stress relaxation during the stepwise loading experiment [189]. Note that the selected value for E_0 is not relevant in this study, since only displacements and not forces are considered. The Poisson's ratio of the bone voxels was selected to be v=0.3 [24,123]. Depending on the simulation method, linear-elastic or damage-based nonlinear material properties were chosen. The used nonlinear material model consists of a linear-elastic region, a damaged region including hardening (hardening modulus E_h=0.05E_0) and a failure region. The material degradation in the damaged region is modelled by reduction of the elastic modulus dependent on the observed damage. An isotropic, quadric damage onset surface models the transition from the linear-elastic to the nonlinear regime (shape parameter ζ_0=0.3, critical damage D_c=0.9) [24,123]. Different damage onset strains in tension and compression (ε_0^+=0.0068, ε_0^-=0.0089) are used to account for the tension-compression asymmetry of bone [24,123]. In order to capture also deformations of the void volume, background voxels were assigned linear-elastic material properties with an elastic modulus of E_0=0.0002GPa and a Poisson's ratio of v=0.3. Displacement boundary conditions were applied to the top and bottom layers of the μFE models. The boundary conditions were obtained by trilinear interpolation of the DVC derived displacement fields at a prior defined elastic load step ($^{DVC, El}\underline{u}$) and at $Step_{Ult}$ ($^{DVC, Ult}\underline{u}$) following the methodology of Chen et al. [107]. In order to define the elastic load step ($Step_{El}$) the 0.1% strain-offset method was used to determine the yield point of the experimental force-displacement curves. The last load step before yield was defined to be $Step_{El}$. For every specimen six different μFE models were created to predict the displacement fields at the elastic and at the ultimate load step for three different simulation methods (see next section).

40

2.2.4 Simulation methods

In this study three different simulation methods were compared (see Fig. 2.1E): linear (L), nonlinear (NL), and nonlinear-stepwise (NLS). For the L method, linear-elastic material properties were assigned to the bone voxels. The boundary conditions were derived from DVC displacement fields $^{DVC, El}\underline{u}$ and $^{DVC, Ult}\underline{u}$. The DVC displacement fields were obtained by single registration of the preloaded to the deformed images at $Step_{El}$/$Step_{Ult}$ without considering any in-between steps. The linear µFE analysis was solved in one increment. For the NL simulation method, damage-based nonlinear material properties were applied and the analysis was solved in several displacement increments of same size i.e. the DVC displacement at the boundary was taken ($^{DVC, El}\underline{u}$, $^{DVC, Ult}\underline{u}$) and linearly scaled in-between (radial load). Regarding the NLS method, the boundary conditions were applied stepwise using the DVC displacement field of every available load step until $Step_{El}$ and $Step_{Ult}$. In order to obtain all of these displacement fields the preloaded images had to be registered to the deformed images of all in-between load steps until $Step_{El}$/$Step_{Ult}$. Note that the NLS method therefore also captures nonlinear changes of the boundary conditions of the experiments (non-radial load), which might affect the damage evolution and hence influence the prediction of the displacements (see Fig. 2.1E).

All µFE models were solved with the µFE solver ParOSol-NL [24] on a cluster using up to 80 CPUs (CPU: AMD Ryzen 7 3700X). The number of elements ranged between 12.9million and 13.6million (see Table 2.2). Furthermore, Table 2.2 lists the CPU hours for all simulation methods and specimens at $Step_{Ult}$.

Table 2.2
Comparison of element number, degrees of freedom and computational costs in CPU hours for all simulation methods and all specimens at $Step_{Ult}$.

Specimen	Element number in million	DoF in million	CPU hours at $Step_{Ult}$		
			L*	NL*	NLS**
A3	13.0	39.5	0.9	60.7	177.4
D2	13.6	41.3	0.7	51.4	193.7
D3	12.9	39.2	1.0	98.5	230.8
D5	13.2	40.0	1.0	91.1	213.4
D6	13.2	40.0	1.1	68.5	182.9

* Usage of 72CPUs
** Usage of 80CPUs

2.2.5 Comparison between µFE and DVC and damage analysis

In order to reduce boundary condition effects, only the middle 80% in height of the µFE models (corresponding to 64% in height of the original specimens) were considered for comparing the predicted and measured displacement fields. The comparison was performed at $Step_{El}$ ($^{FE, El}\underline{u}$ vs. $^{DVC, El}\underline{u}$) and at $Step_{Ult}$ ($^{FE, Ult}\underline{u}$ vs. $^{DVC, Ult}\underline{u}$) (see Fig. 2.1D).

A so-called volume-averaging method, similar to the method used by Fu et al. [171], was applied to compare the displacement fields (see Fig. 2.5 and Appendix A) instead of a pointwise comparison [107,119]. The complete FE mesh was superimposed by the cubic grid used to perform the DVC registration. Hence, every node in the FE mesh was included in a cube of 24x24x24 voxels in size and a DVC point in the middle. All nodes in a specific cube were then

assigned to the corresponding DVC point. The displacements of all nodes inside a specific cube were then averaged (including both bone and void volume) and compared to the corresponding displacement value of the DVC point. DVC points inside a surrounding cubic volume with a relative density lower than 5% were excluded from the displacement field comparison. Furthermore, DVC points located outside of the bone cylinder were not considered.

Linear regressions were used to show the relationship between the measured DVC displacement fields and the µFE predicted displacement fields. For each specimen, for both relevant load steps ($Step_{El}$, $Step_{Ult}$), for all three Cartesian components of the displacement field and for its magnitude, the following parameters were computed: Slope, intercept, coefficient of determination (R^2), residuals, and root mean square error (RMSE). Furthermore, the spatial distribution of the residuals was evaluated qualitatively. For this purpose, all µFE mesh nodes of a specific cube surrounding a DVC point were assigned the corresponding residual value ($^{FE}\underline{u}$ - $^{DVC}\underline{u}$) of that DVC point. Nodes in volumes where the DVC point was excluded were displayed in black colour.

Damage was evaluated at $Step_{Ult.}$ Regarding the L simulation method an element was classified as damaged if the effective strain ε_{eff} exceeded a critical value of $\varepsilon_c = 0.89\%$ [123]. This value was selected since it corresponded to the yield strain in compression of the material model used for NL and NLS.
For the simulation methods NL and NLS an element was defined as damaged if damage D>0. Damage evolution was compared for NL and NLS for the apparent strain value ε of the cropped specimen (80% of original height).

All statistical evaluations were performed using Python 3.8 (https://www.python.org/) and the included library SciPy [194]. All figures showing the spatial distribution of residuals and the distribution of damage were created using Paraview (https://www.paraview.org/).
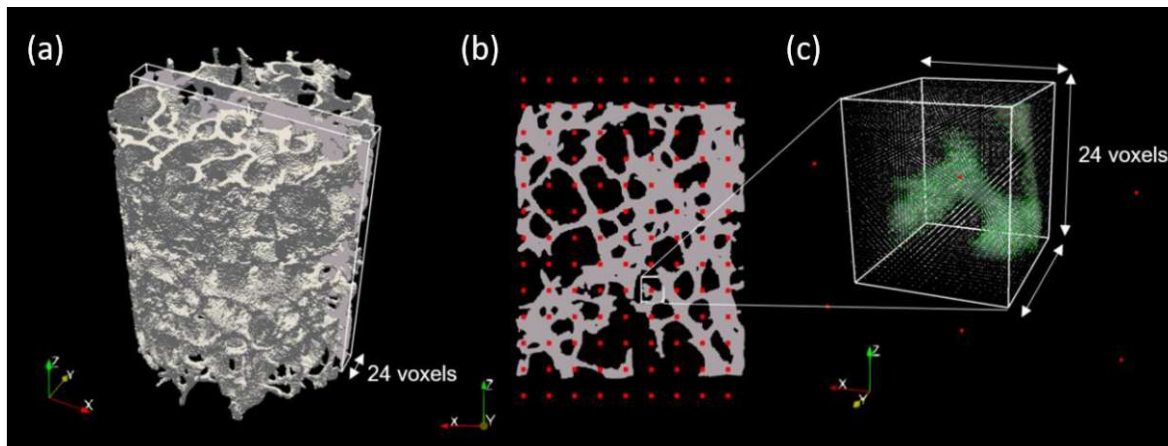
Fig. 2.5 Graphical description of the **v**olume averaging method. (a) shows the whole bone biopsy. A small part in the middle with a thickness of 24 voxels is cut out and shown in (b). In (b) the sliced bone overlaid by the DVC points marked in red is displayed. (c) focusses on a single cube with 24 voxels surrounding one DVC point. The DVC point in the middle of the cube is again marked in red, while µFE mesh nodes corresponding to bone material are displayed in green and µFE mesh nodes corresponding to bone marrow material are visualized in white. To compare the DVC displacement with the µFE predicted displacement the nodal displacements of all nodes within the corresponding 24x24x24 voxel cube were averaged.

2.3 Results
2.3.1 Correlation of displacement fields
The evaluation of displacement fields of all specimens at $Step_{El}$ ($^{FE, El}\underline{u}$ vs. $^{DVC, El}\underline{u}$) showed that µFE model displacements are highly correlated to DVC displacements (R^2 between 0.97 and 1

for pooled data and $R^2{>}0.83$ for individual specimens) (see Fig. 2.6 (a), Table 2.3 (a) and supplementary material). Intercepts were close to zero and slopes close to one for all methods and all Cartesian coordinates and magnitude (Intercept: -0.2µm to 3.2µm; Slope: 0.99 to 1.04 for pooled data). Regarding intercept, slope, and R^2, all three simulation methods showed similar results.

Similar to the results at $Step_{EI}$ the evaluation of displacement fields of all specimens at $Step_{Ult}$ ($^{FE,\,Ult}\underline{u}$ vs. $^{DVC,\,Ult}\underline{u}$) showed a high correlation between µFE model displacements and DVC displacements (see Fig. 2.6 (b), Table 2.3 (b) and supplementary material). For pooled data, intercepts were close to zero (4.4µm to 12µm) and slopes ranged between 0.97 and 1.17. In all spatial directions and for the magnitude, slopes and R^2 values were closer to one for the simulation methods NL and NLS ($R^2{>}0.94$ for pooled data and $R^2{>}0.68$ for individual specimens) compared to L ($R^2{>}0.92$ for pooled data and $R^2{>}0.59$ for individual specimens). Furthermore, the intercept values for NL and NLS were closer to zero and slopes closer to one in comparison to L. No difference was observed between NL and NLS.

Table 2.3
Minimum coefficient of determination (R^2) of all three spatial directions of individual specimens.

$Min(R_x^2, R_y^2, R_z^2)$		A3	D2	D3	D5	D6
(a) $Step_{EI}$	**L**	0.92	0.96	0.89	0.83	0.88
	NL	0.92	0.96	0.89	0.85	0.88
	NLS	0.92	0.96	0.89	0.85	0.88
(b) $Step_{Ult}$	**L**	0.66	0.93	0.89	0.87	0.59
	NL	0.73	0.95	0.92	0.88	0.68
	NLS	0.73	0.95	0.92	0.88	0.68

(a) $Step_{EI}$

(b) *Step*$_\text{Ult}$
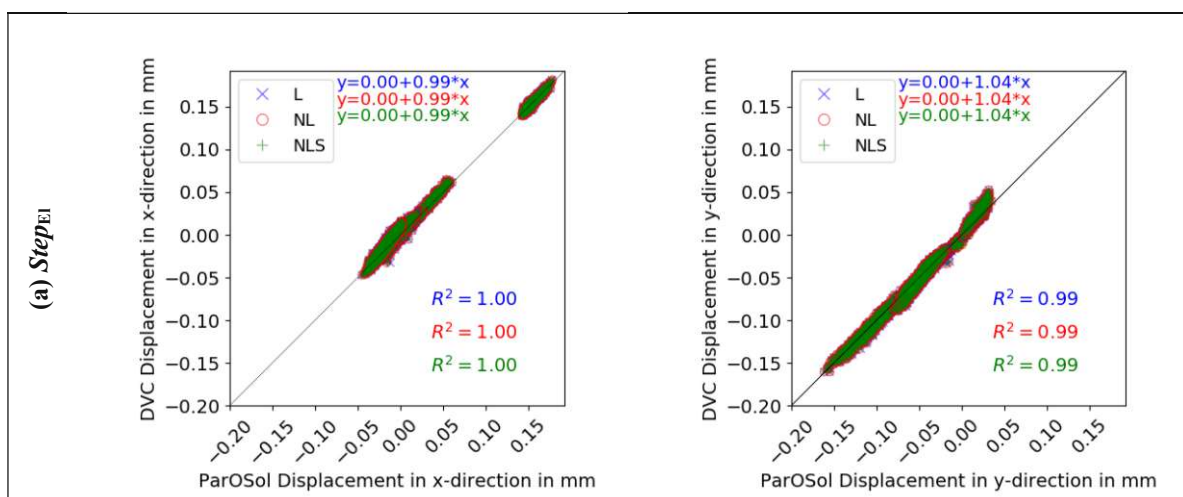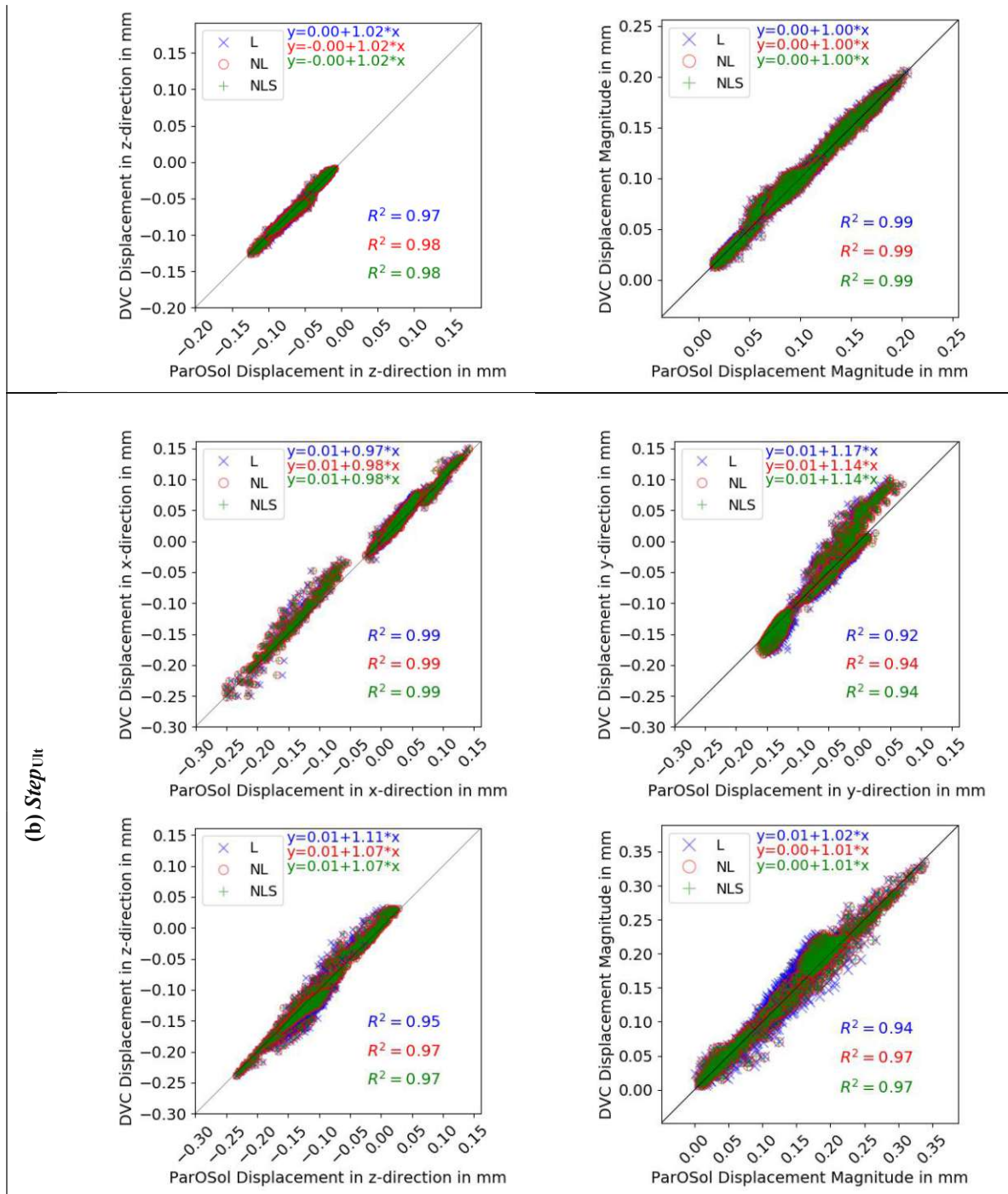
Fig. 2.6 Linear regression analyses of pooled data between the μFE predicted displacements and the DVC measured displacements for all 5 specimens at the elastic (a) and at the ultimate (b) load step.

2.3.2 Residuals

At *Step*$_\text{El}$, the residuals showed similar interquartile range (IQR), medians and residual ranges for all methods (see Fig. 2.7 (a)). When all directions are considered, the residuals ranged from -22μm to 20μm.

At *Step*$_\text{Ult}$, IQR and residual ranges were slightly higher for the simulation method L in all directions and for the magnitude (e.g. z-direction: Residual range of L: -59μm to 46μm; Residual range of NL and NLS: -52μm to 41μm) (see Fig. 2.7 (b)). Furthermore, the median was shifted further from zero for L (e.g. z-direction: Median of L: 6μm; Median of NL and NLS: 4μm). Considering all directions, the residuals ranged between -80μm and 58μm.
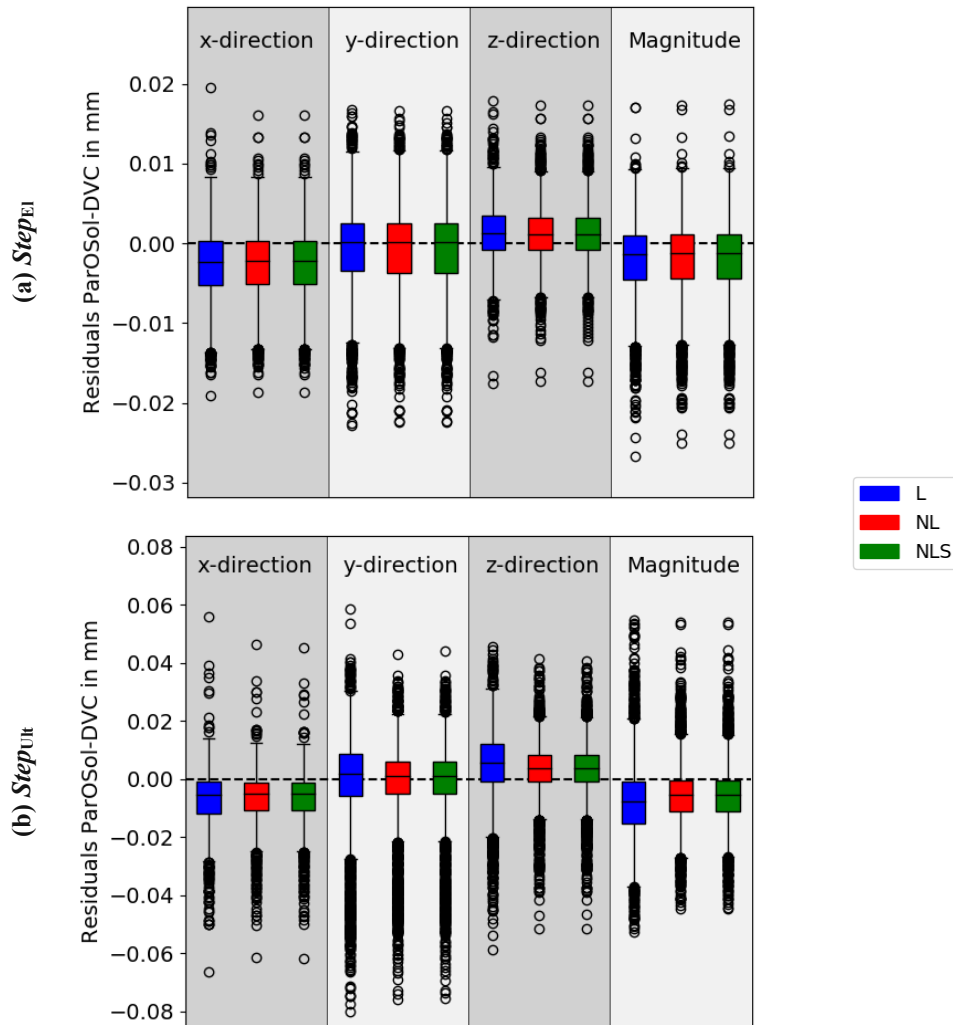
Fig. 2.7 Boxplot of residuals of pooled data of all specimens at the elastic (a) and at the ultimate (b) load step.

2.3.3 Spatial distribution of residuals

At $Step_{El}$, the spatial distribution of the residuals of all three simulation methods was similar and showed concentrated regions of high absolute residuals in all directions and for most specimens (see Fig. 2.8 (a)). At $Step_{Ult}$, the concentrated regions of high absolute errors were similar to those recognized at the elastic load step (see Fig. 2.8 (b)). The simulation method L showed higher maximum absolute residuals than NL and NLS in y- and z-direction (e. g. L in z-direction max. between 46% to 104% of average compression vs. NL in z-direction max. between 29% to 91% of average compression (see Appendix B)). Fig. 2.8 shows the described observations for one representative sample and one displacement field direction. The results were similar for most samples and spatial directions; only the locations of high absolute residuals were different (see supplementary material).
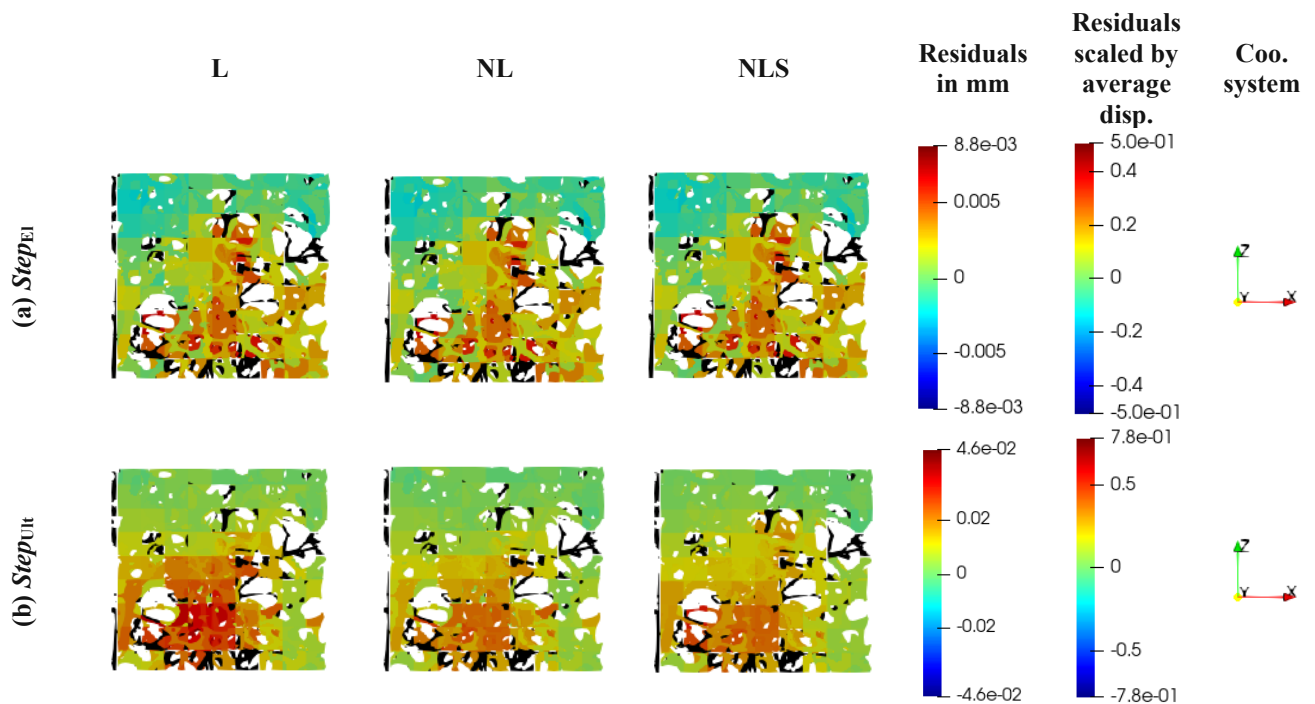
Fig. 2.8 Spatial distribution of residuals at the elastic (a) and at the ultimate (b) load step of one representative specimen (A3) in z-direction. All bone material nodes of a specific volume were assigned to the corresponding residual value of the specific DVC point. Nodes in volumes where the DVC point was excluded were displayed in black colour. Two colour maps were used: One shows the residuals in mm and the other one scales the residual value with the average compression of the specimen (see Appendix B).

2.3.4 RMSE

At $Step_{El}$, RMSE values for all specimens ranged between 2µm and 10µm (mean of all spatial directions: 4.5µm) for all simulation methods and in all directions and for the magnitude (see Fig. 2.9 $Step_{El}$). The RMSE difference between the L and NL simulation method was lower than 0.6µm for all specimens and in all directions and for the magnitude. NL and NLS performed quite similar.

For all three simulation methods the RMSE increased at $Step_{Ult}$, but the increase was more pronounced for the L method (see Fig. 2.9 $Step_{Ult}$). RMSE of L ranged between 11µm and 18µm in z-direction, while the reached RMSE values for the NL and NLS methods were between 8µm and 14µm. In x- and y-direction the difference between the L and NL method at the ultimate load step was less pronounced than in z-direction and for the magnitude.
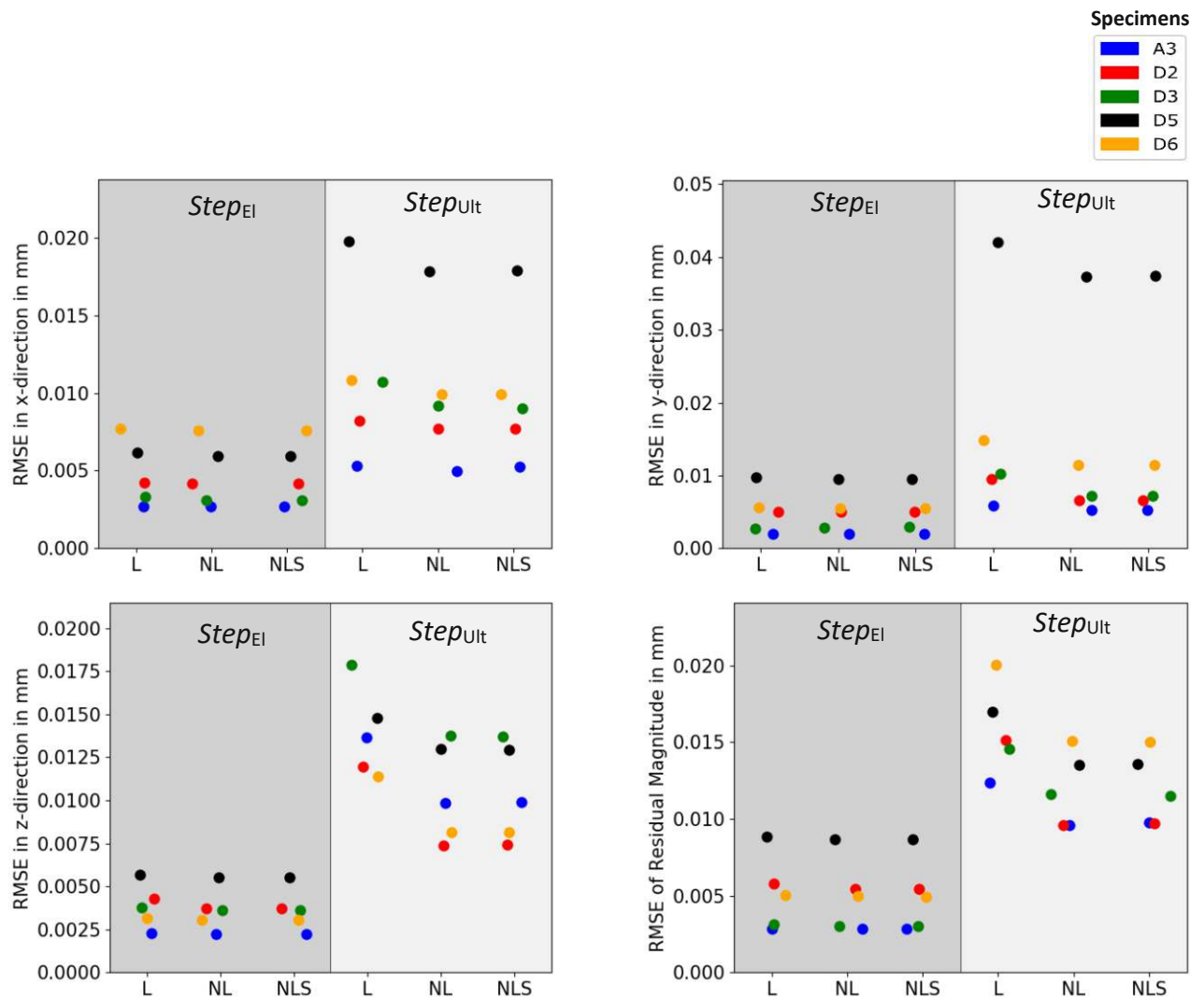
Fig. 2.9 RMSE of all specimens (A3, D2, D3, D5, D6) at the elastic and at the ultimate load step in all directions and for the magnitude.

2.3.5 Damage

At $Step_{Ult}$, the number of damaged elements was highest for the L simulation method (average of 11.3% of total element number). The simulation methods NL and NLS reached a far lower number of damaged elements (average of 7.4% for NL and 8.4% for NLS of total element number) (see Fig. 2.10 (a) and 2.11). Especially specimens D2 and D5 (>12.3% and 11.6% of total element number) had a high number of damaged elements. Figure 2.11 (b) shows the difference in damage between the three simulations methods. The percentage of elements that were classified as damaged in the one simulation method and classified as not damaged in the other one, ranged between 1.4% and 9.8% of the total element number when L was compared to NL or NLS. Between NL and NLS the difference in damage classification was rather low (0.3% to 1.6% of total element number).

The damage distribution was different for all specimens (see Fig. 2.11). The L simulation method overestimated the number of damaged elements, but the location of the damaged elements qualitatively agreed in all methods. The damaged region predicted by the NL method was mostly a subset of the damaged region predicted by the L method. The number of damaged elements predicted exclusively be the NL method were rather low. NL and NLS methods showed almost no differences in the damage distribution (see supplementary material).

The damage evolution (see Fig. 2.12 for specimen A3 and supplementary material for further specimens) shows that the number of damaged elements increases in a similar manner for NL and NLS for all specimens. The number of damaged elements is rather low until a strain value of approximately 0.4% is reached. Then the number of damaged elements increases in a linear manner.

(a)

(b)
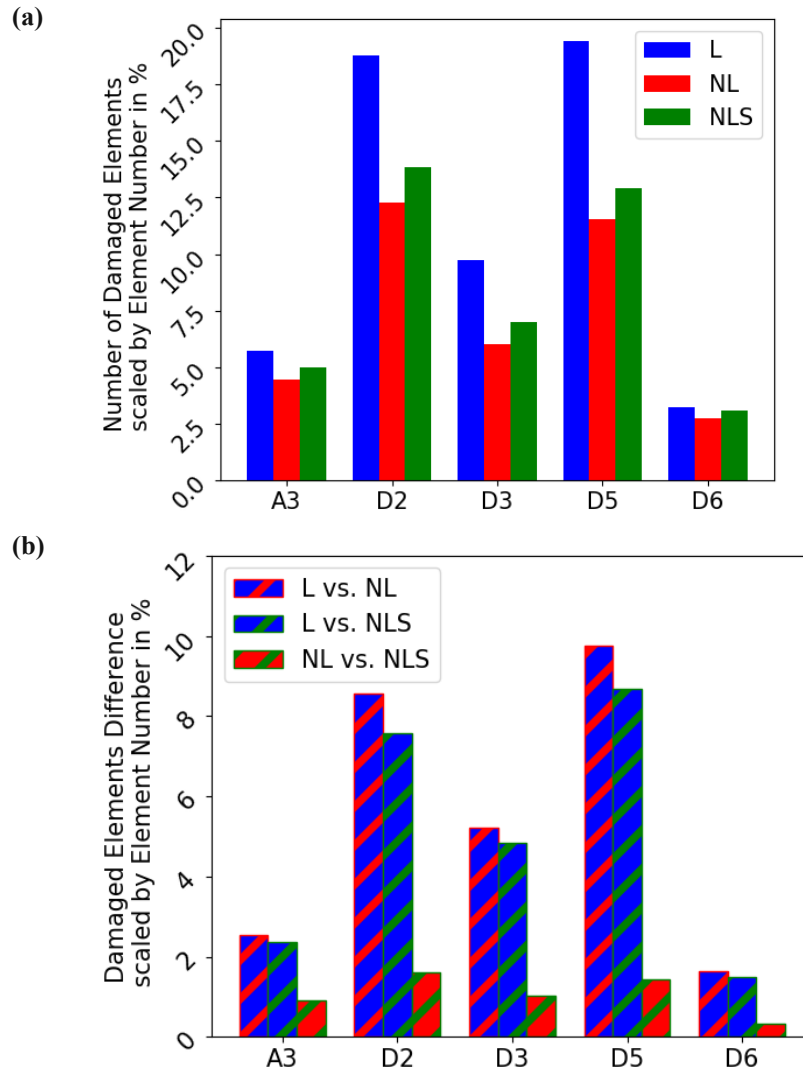
Fig. 2.10 (a) Number of damaged elements for all simulation methods scaled by the element number of bone material of each specimen at $Step_{Ult}$. Regarding L, elements were classified as damaged when $\varepsilon_{eff} > 0.89\%$. For the simulation methods NL and NLS, elements were classified as damaged when $D > 0$. **(b)** Difference in damage scaled by the element number of bone material of each specimen at $Step_{Ult}$. This plot visualizes the number of elements which are classified as damaged in one simulation method and classified as not damaged in the other one.

A3   **D2**

D3   **D5**

D6

L damaged only

Both damaged

NL damaged only
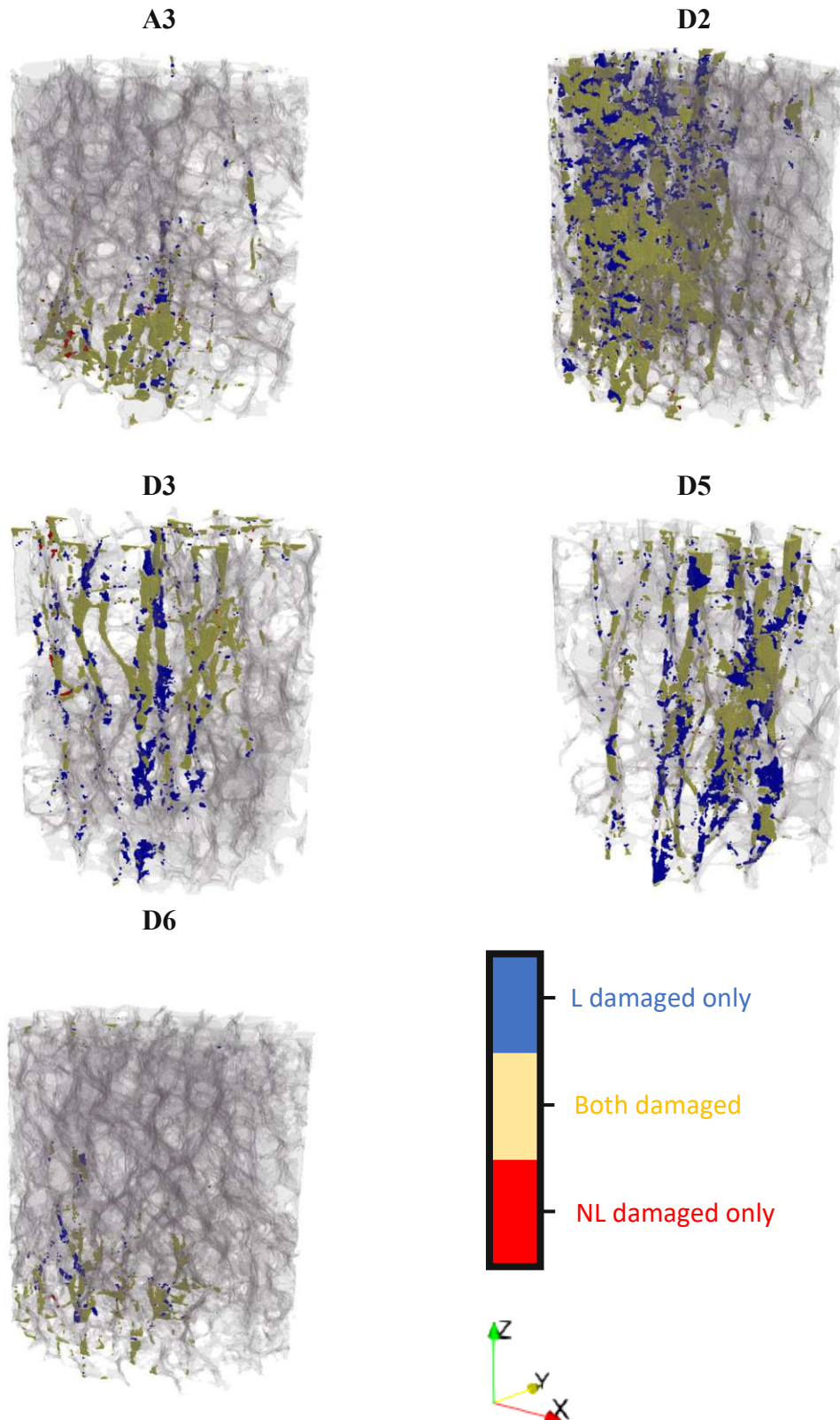
Fig. 2.11 Comparison of damage distribution between the simulation methods L and NL for all specimens at Step$_{\text{Ult}}$. Regarding L, elements were classified as damaged when $\varepsilon_{\text{eff}} > 0.89\%$. For the simulation methods NL and NLS, elements were classified as damaged when $D > 0$. Elements that were marked as damaged in both simulation methods are visualized in yellow, while those that only one simulation method classified as damaged were marked in blue (only L) and red (only NL).
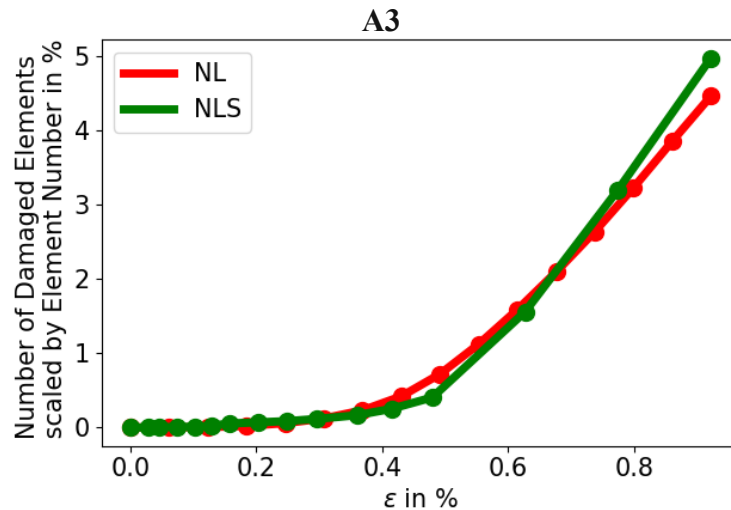
Fig. 2.12 Damage evolution with apparent strain ε in z-direction (for specimen cropped to middle 80% of height) for on representative specimen (A3) for simulation methods NL and NLS. For the simulation methods NL and NLS, elements were classified as damaged when D > 0. The y-axis shows the number of damaged elements scaled by the total element number of bone material.

2.4 Discussion

The aim of this study was to compare the displacement predictions of three µFE simulation methods (L, NL, and NLS) with DVC measurements at the elastic and in the ultimate load step. Therefore, µFE models of human trabecular bone biopsies simulating stepwise compression were analyzed, displacement predictions were averaged and compared to DVC displacement measurements of the same volume.

The results showed that all three simulation methods were able to replicate the averaged displacement field at the elastic as well as at the ultimate load step (see Fig. 2.6 and supplementary material). At the elastic load step, the µFE models were able to predict more than 83% of the displacement variations in all three spatial directions and for the magnitude, for all simulation methods and for all five individual specimens. At the ultimate load step, the coefficients of determination decreased but the predictions were still highly correlated to the DVC measurements.

While all three simulation methods showed similar performance regarding all evaluated parameters at the elastic load step, slight differences became evident when displacement results were evaluated at the ultimate load step. Whereas the simulation method L was able to predict more than 59% of displacement variations in all three Cartesian directions and for the magnitude, the displacements predicted by the simulation methods NL and NLS correlated better (R^2>0.68) with the DVC measured displacements (see Table 2.3 and supplementary material). In all directions and for all specimens the coefficient of determination was lower for the L simulation method. Furthermore, higher IQR, residual ranges, and RMSE values were observed in all directions (see Fig. 2.7 and Fig. 2.9). Similar results were reported by Peña Fernández et al. [188] who showed that nonlinear µFE models could improve the displacement predictions in yielded bone regions. The improved performance in displacement prediction of the NL method at the ultimate load step is compromised by the long solving time in comparison to the L method (maximum CPU hours at $Step_{Ult}$: L: 1.1h vs. NL: 98.5h) (see Table 2.2). Since the L method was still capable to predict the displacement field with acceptable accuracy and precision until the ultimate load, its application seems to be sufficient when evaluating displacement fields and qualitatively evaluating damage locations of similar bone biopsies

under compression. However, note that the damaged regions were found to be at similar locations but generally overestimated in L when compared to the NL or NLS methods (see Fig. 2.10 and 2.11). Thus, caution is warranted if damage is interpreted using linear µFE models at ultimate load. These results are in line with those of Stipsitz et al. [123], where damage of linear and nonlinear µFE model simulations was observed at similar locations in the distal radius and the number of damaged elements was generally overestimated using the linear µFE models. Neither at the elastic load step nor at the ultimate load step, a difference in performance between NL and NLS could be observed. Furthermore, the number and location of damaged elements at the ultimate load step were in good agreement (see Fig. 2.10 and 2.11). In contrast, the simulation time for NLS (maximum CPU hours at $Step_{Ult}$: 230.8h) was much higher than for NL (see Table 2.2). One can assume that in the presented use case (small trabecular biopsy), the nonlinearity of the boundary conditions does not play a crucial role for the accuracy and precision of the local displacement field. This was also confirmed by the damage evolution, which showed only minor differences between NL and NLS (see Fig. 2.12). However, differences between NL and NLS could be more pronounced for different case studies (e.g. larger displacements, larger bone samples, different material models, and different output parameters) which would justify the higher computational effort.

The µFE displacement predictions of all simulation methods were better at the elastic load step. For all specimens and in all directions higher R^2 values (e.g. pooled data of NL method in z-direction: $Step_{El}$: R^2=0.98; $Step_{Ult}$: R^2=0.97), lower IQR, residual ranges (e.g. pooled data of NL method in z-direction: $Step_{El}$: -17µm to 17µm; $Step_{Ult}$: -51µm to 41µm), and RMSE values were observed. Damage analysis at the ultimate load step showed that the damage distribution of most specimens (A3, D2, D6) corresponded to regions of high residual errors (see Fig. 2.11 and supplementary material), indicating difficulties to predict the behaviour of yielding bone. Future studies could try to improve the µFE performance especially at the ultimate load step possibly by implementing a more complex material model to the simple damage-based material model that was used in this study. This suggestion is supported by Peña Fernández et al. [188], who used a linear elastic-viscoplastic damage model including geometrical nonlinearity and only reported minor deterioration in displacement predictions when comparing results at 1% and 3% compression. In consequence, further enhancements in material modelling are important to increase the accuracy of displacement predictions. A further approach to improve the displacement predictions of µFE models seems to be the implementation of tissue heterogeneity. However, since studies from Peña Fernández et al. [188] and Fu et al. [171] only reported negligible difference between homogeneous and heterogeneous models one can conclude that the microstructure dominates the mechanical behaviour of bone tissue.

The study results were generally in line with values reported in literature. At the elastic load step, the results of all evaluated parameters (regression, residuals, and RMSE) were similar to the findings reported by Costa et al. [119] and Chen et al. [107], who conducted similar studies with comparable GS (500µm to 1872µm). They reported agreements of more than 86% between the displacement fields measured with DVC and predicted by linear µFE. In this study, only one specimen (D5) showed a slightly lower coefficient of determination (L: R^2=0.83) in x-direction. The RMSE value range of this study (2µm to 10µm) was similar to that reported by Costa et al. [119] (1µm to 12µm) and Chen et al. [107] (1µm to 11µm). The results at the elastic load step were further compared to the results of Peña Fernández et al. [188] at 1% compression. The nonlinear models showed a weaker correlation (R^2>0.53) but also smaller RMSE values below 1.7µm than this study reported (NL: R^2>0.85; RMSE<9.5µm). The low RMSE value can be attributed to the high resolution of 5µm used in the study of Peña Fernández et al. [188]. The results at the ultimate load step were compared to Oliviero et al. [124], who used a linear-elastic material model to predict the displacement fields in the elastic and in the nonlinear regime.

Coefficients of determination were higher (R^2>0.77) than in this study (R^2>0.59), but RMSE values were in line with the findings of our study (e.g. Oliviero et al. [124] in z-direction: 6µm to 24µm; this study L method in z-direction: 11µm to 18µm). Reasons for the weaker correlation could be that no outliers were removed, whereas in all above mentioned studies Cook's distance was applied for this purpose. In addition, the usage of the volume averaging method leads to an increased number of comparison points, including points in regions with low BV/TV and higher residuals (see Appendix A).

The study is restricted by several limitations. To begin with, the sample size was rather small, but still comparable to similar studies [107,119]. Next, the study only compared averaged displacements of 1mm^3 seized cubic volumes and does not capture local displacements. Furthermore, the displacement precision of the DVC measurements and therefore also the GS size were derived just from literature [191,192,195] and could not be evaluated with a repeated-scan test [168,196] in this study. Although a direct comparison with literature would require the same bone structure and scanning parameters, previous studies evaluating precision showed that displacement errors are rather small in the size of a fraction of a voxel [166,168,190]. Thus, it can be assumed that they did not affect the main outcomes of this study. Nevertheless, the strain precision is much more sensitive to the image quality (signal to noise ratio) due to the fact that the differentiation process amplifies the errors associated to the displacements [166]. Higher resolution images, using Synchrotron tomography [197] would lead to a DVC accuracy high enough to compare DVC and µFE strains. However, in situ mechanical testing combined with Synchrotron tomography has limitations in assessing the local mechanical behaviour of bone tissue due to radiation induced damage [198–200]. In consequence, our study is limited to the sole evaluation of displacements and not strains. Furthermore, radiation-induced material changes or damage due to the multiple scanning of the specimens could have an influence on our study results. Nevertheless, effects of radiation were found only when higher imaging flux, typical of synchrotron µCT imaging were used [198]. Although future studies need to quantify the effect of this limitation, we can assume that it did not severely compromise our study results since the displacement comparison between the µFE model and the experiments showed high correlations. Another limitation is the number of displacement steps and the variable displacement step size, which could influence the performance of the NLS method. Nevertheless, the applied displacement step size appeared sufficient to capture the nonlinearity in the apparent load-displacement curves. Lastly, the application of the highly parallel µFE solver ParOSol comes with the limitation that geometrical nonlinearity and further aspects of the constitutive behaviour of bone material (plasticity, viscosity, poroelasticity) were not considered. However, the usage of ParOSol together with its implemented damage-based material model can be justified since the solver works highly efficient and therefore enables to simulate large bone structures.

2.5 Conclusion

In this study, predicted displacements of linear and nonlinear µFE models were compared to DVC measured displacements at a specific load step in the elastic regime and at the ultimate load step. The predicted displacement fields of all µFE simulation methods were in good agreement with the DVC measured displacement fields. Although the nonlinear µFE models improved the prediction of the displacement fields slightly at the ultimate load step in all spatial directions, the increased simulation times cannot be ignored. Furthermore, damage was evaluated and occurred at similar locations for all linear and nonlinear µFE models. Hence, this study confirms that for similar use cases (displacement and qualitative damage evaluation of compressed trabecular bone biopsies) linear µFE models are sufficient in order to predict

displacement fields in the linear and nonlinear regime as well as to reveal damage locations with acceptable accuracy and very low computational effort.

CRediT authorship contribution statement

Pia Stefanek: Writing – original draft, Project administration, Investigation, Formal analysis.
Alexander Synek: Writing – review & editing, Supervision, Methodology, Conceptualization.
Enrico Dall'Ara: Writing – review & editing, Supervision, Software, Methodology.
Dieter H. Pahr: Writing – review & editing, Supervision, Methodology, Conceptualization.

Declaration of competing interest

The authors declare the following financial interests/personal relationships which may be considered as potential competing interests: DP is CEO of Dr. Pahr Ingenieurs e.U. which develops and distributes the software Medtool. PS, AS and ED have no conflicts of interest to declare.

Data availability

Data will be made available on request.

Acknowledgments

Appendix C. Supplementary data

Supplementary data to this article can be found online at https://doi.org/10.1016/j.jmbbm.2022.105631.

Appendix A

The majority of studies that compared μFE results to DVC measurements used a pointwise validation [107,119,124,169]. The pointwise method only includes DVC points inside the μFE mesh. Since the DVC nodes are by construction located at the center of the μFE elements, the DVC displacement values were compared to the interpolated displacement values of the μFE nodes. Fig. 2.13 compares the two different evaluation methods (volume-averaging vs. pointwise) at $Step_{El}$ and $Step_{Ult}$ for one representative specimen in z-direction for the simulation method L. The results for intercept, slope, and R^2 are quite similar for both methods. A difference between the evaluation methods is the number of comparison points (Volume-averaging method: 476 points; Pointwise method: 83 points).
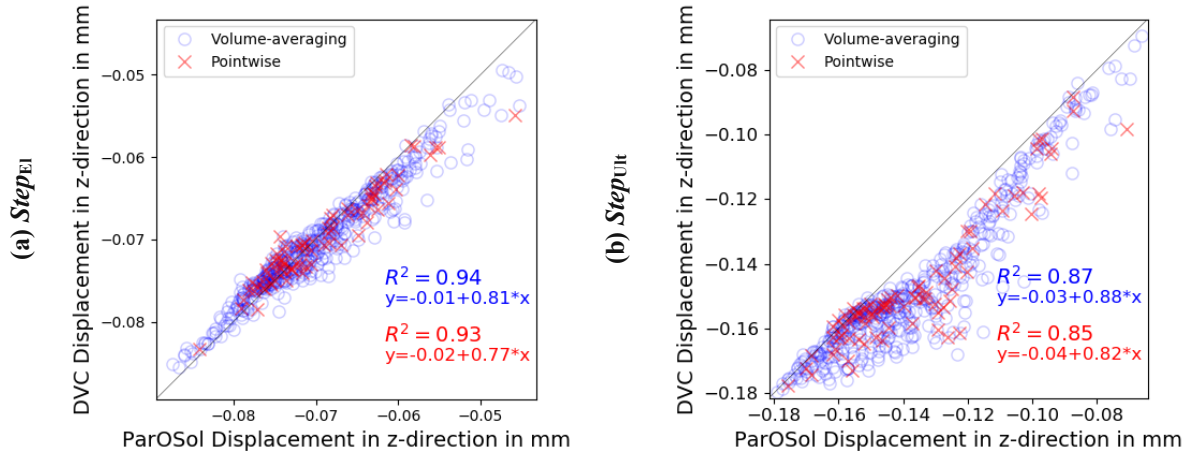
Fig. 2. 13 Comparison of evaluation methods at the elastic (a) and at the ultimate (b) load step for one representative specimen (A3) in z-direction using the linear simulation method.
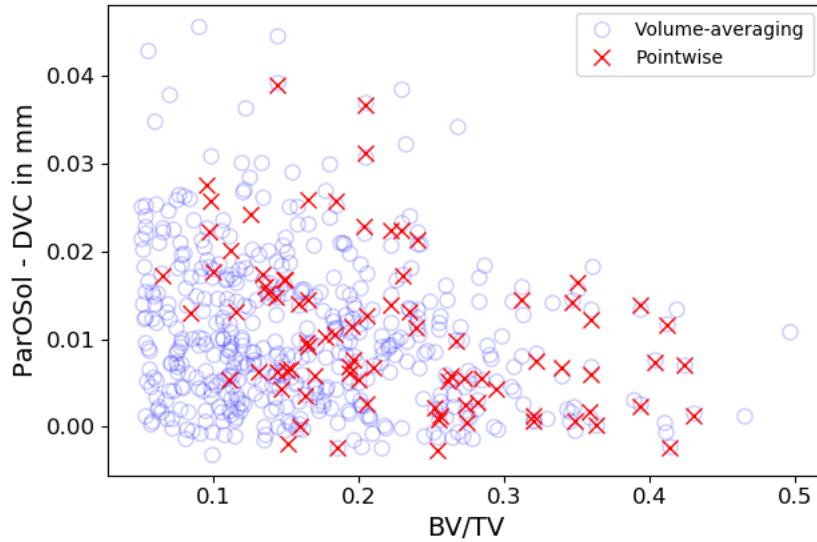
Fig. 2. 14 Comparison points of the evaluation methods regarding BV/TV of the surrounding cubic volume and residual height at $Step_{Ult}$. One representative specimen (A3) was selected and evaluated with the linear simulation method in z-direction.

Furthermore, Fig. 2.14 shows another difference between the evaluation methods. Most comparison points of the pointwise method refer to cubic volumes with a BV/TV of more than 10%. Regarding the volume-averaging method, there are many comparison points that refer to cubic volumes with a low BV/TV between 5 and 10%. Moreover, Fig. 2.14 shows that the residual values are higher in volumes of low BV/TV. The results were similar for all specimens, all simulation methods and in all directions.

Appendix B

Depending on the evaluated load step ($Step_{El}$, $Step_{Ult}$), the average compression of the individual specimens was computed in the following way:

$$\Delta^{DVC}\underline{\overline{u}} = {}^{DVC}\underline{\overline{u}}_{Top} - {}^{DVC}\underline{\overline{u}}_{Bottom} \tag{2.1}$$

54

$^{DVC}\overline{\underline{u}}_{Top}$ describes the average DVC displacement at the top layer of the comparison region (64% of original specimen height). Equally, $^{DVC}\overline{\underline{u}}_{Bottom}$ describes the average DVC displacement at the bottom layer of the comparison region.

Chapter 3

Paper 2

From the manuscript

Comparison of simplified bone-screw interface models in materially nonlinear µFE simulations

Pia Stefanek, Dieter H. Pahr, Alexander Synek

Abstract

Micro finite-element (µFE) simulations serve as a crucial research tool to assist laboratory experiments in the biomechanical assessment of screw anchorage in bone. However, accurately modelling the interface between bone and screw threads at the microscale poses a significant challenge. Currently, the gold-standard approach involves employing computationally intensive physical contact models to simulate this interface. This study compared nonlinear µFE predictions of deformations, whole-construct stiffness, maximum force and damage patterns of three different computationally efficient simplified interface approaches to the general contact interface in Abaqus Explicit, which was defined as gold-standard and reference model. The µCT images (resolution: 32.8µm) of two human radii with varying bone volume fractions were utilized and a screw was virtually inserted up to 50% and 100% of the volar-dorsal cortex distance. Materially nonlinear µFE models were generated and loaded in tension, compression and shear. In a first step, the common simplification of using a fully-bonded interface was compared to the general contact interface, revealing overestimations of whole-construct stiffness (19% on average) and maximum force (26% on average), along with inaccurate damage pattern replications. To enhance predictions, two additional simplified interface models were compared: tensionally strained element deletion (TED) and a novel modification of TED (TED-M). TED deletes interface elements strained in tension based on a linear-elastic simulation before the actual simulation. TED-M extends the remaining contact interface of TED by incorporating neighboring elements to the contact area. Both TED and TED-M reduced the errors in whole-construct stiffness and maximum force and improved the replication of the damage distributions in comparison to the fully-bonded approach. TED was better in predicting whole-construct stiffness (average error of 1%), while TED-M showed lowest errors in maximum force (1% on average). In conclusion, both TED and TED-M offer computationally efficient alternatives to physical contact modelling, although the fully-bonded interface may deliver sufficiently accurate predictions for many applications.

3.1 Introduction

For more than five decades finite element (FE) simulations have served as invaluable tools in bone implant development and evaluation, complementing laboratory experiments [13]. Unlike laboratory experiments, numerical studies are cost- and time-effective and do not rely on tissue samples which can be difficult to obtain. Micro-finite element (µFE) simulations, based on high-resolution computed tomography (CT) scans, currently represent the gold standard, particularly for the challenging task of modelling screw anchorage in trabecular bone. They are able to resolve the bone-screw interface on the microscale and hence capture the screw thread geometry as well as peri-implant bone region in detail, which was reported to be essential for an accurate prediction of the mechanical behavior of the bone-screw system [19–21].

Bone-screw µFE simulations have to overcome two major challenges: bone-screw interface modelling and simulation of pre-damage due to screw insertion. Usually, linear-elastic µFE simulation studies assumed a fully-bonded interface and neglected pre-damage in the peri-implant bone region. They reported overestimations in whole-construct stiffness and strains up to one order of magnitude [117,120,137]. In order to account for the reduction in mechanical competence of the peri-implant bone region [138–140], Steiner et al. [120] and Torcasio et al. [137] implemented a peri-implant damage zone with reduced stiffness in their linear-elastic µFE simulations and were able to reduce the errors in the predicted strain and whole-construct stiffness to about 10% on average. Since the bone-screw failure process as well as the contact mechanics at the bone-screw interface are highly nonlinear, recent studies have turned to nonlinear µFE simulations. Most of them included frictional contact at the bone-screw interface but ignored peri-implant bone damage [121,122]. Nevertheless, they were able to improve the predictions in comparison to the linear-elastic simulations and were able to quantitatively replicate the experimentally measured screw perforation force [122] and screw pull-out force [121].

Nonlinear µFE models are typically solved with general-purpose FE solvers (e.g. Abaqus, Dassault Systems, Vélizy-Villacoublay, France) which can handle different types of nonlinearities (geometric, material and contact) but are computationally demanding. Ovesy et al. [121] reported solving times of 2h on 16 cores for relatively small models, consisting of a single screw with an average model size of 350,000 elements. In consequence, many nonlinear studies needed to reduce the model sizes by either cropping the bone specimens [121] or decreasing the image resolution [122] in order to achieve manageable solving times. The capability to simulate a complete bone-screw implant system, including multiple screws, can only be achieved using specialized solvers designed to solve large-scale problems (e.g. FEAP, [201], Faim (Numerics88 Solutions Ltd, https://bonelab.github.io/n88/index.html), ParOSol [25], ParOSol-NL [24]). These solvers exhibit improved parallel execution performance and can handle nonlinear models with several hundreds of million elements [179]. However, the application of these efficient solvers always comes with the drawback of reduced model complexity, as they typically only incorporate linear-elastic or simple nonlinear material laws and lack bone-screw contact implementations. To address these limitations, some researchers employed simplified interface model approaches that try to avoid the occurrence of artificial tensile strain on the interface elements. For example, Ovesy et al. [121] and Panagiotopoulou et al. [122], removed the bone elements directly below the screw threads specifically for simulated screw pull-out loading cases. Steiner et al. [120] developed a method independent of the loading case: they conducted an initial linear simulation that was used to calculate the volumetric strain of the interface elements. Then they removed all interface elements undergoing positive volumetric strain and performed the simulation with the updated interface again.

Despite these efforts, the necessity of including contact at the bone-screw interface in µFE models is still in question. The available literature on this subject matter is limited as the effects of interface modelling and peri-implant bone damage due to screw insertion overlap and its influences cannot be discriminated in lab experiments. One of the few studies on this topic was conducted by Steiner et al. [120].They only found minimal whole-construct stiffness differences when comparing the fully-bonded interface to a simplified interface model approach using linear-elastic µFE models. To the authors' knowledge no study yet examined the relevance of interface modelling in the nonlinear regime.

The first aim of this study was to investigate the influence of physical contact modelling regarding deformations, whole-construct stiffness, maximum force and damage distribution using nonlinear µFE in Abaqus Explicit. In a second step, the performance of the already existing simplified interface model of Steiner et al. [120] was evaluated and compared to a newly developed interface model that was found based on a qualitative and quantitative analysis of the contact area. In order to concentrate on the effects of interface modelling in an isolated manner, damage due to screw-insertion was excluded. As this cannot be done experimentally, this study was conducted solely numerical using general contact in Abaqus Explicit as gold-standard and reference model. The study design enables direct transfer of the simplified interface models to highly efficient µFE solvers such as ParOSol-NL.
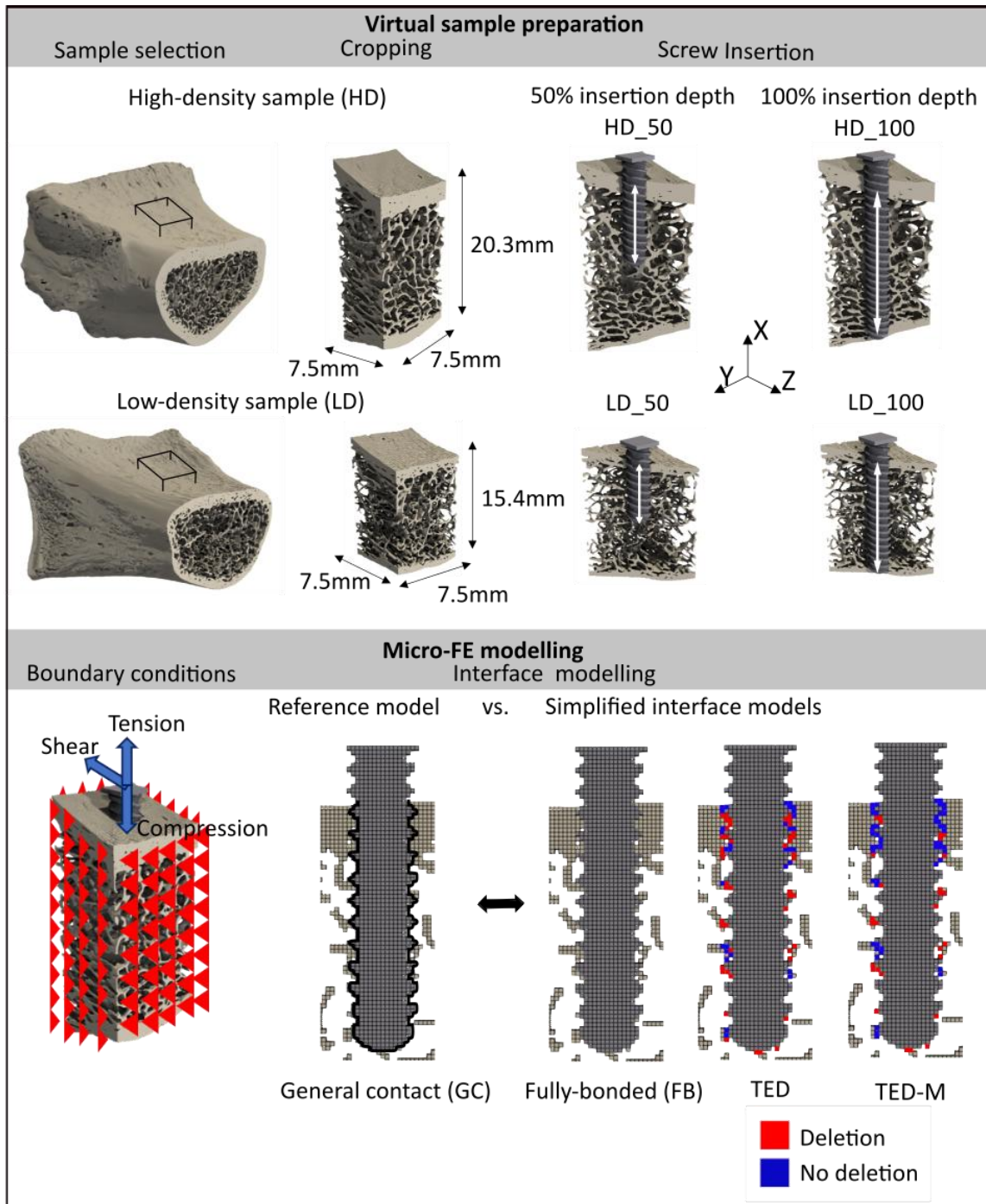
Fig. 3.1 Outline of the study. This figure shows the interface models with lower resolution in order to schematically illustrate the differences at the interface.

3.2 Material and methods

Fig. 3.1 shows the outline of this study. All details can be found below. Shortly, two human radius bone specimens with low and high bone densities were cropped and a screw was virtually inserted. Voxel-based nonlinear µFE models were generated, and three loading cases (tension, compression, and shear) were simulated using Abaqus Explicit. Deformations, whole-construct stiffness, maximum force, and damage distribution within the bone were evaluated. Three different simplified interface models (fully-bonded and "element deletion" models) were compared to a reference model (general contact).

3.2.1 Image processing

Micro-computed tomography (μCT) images of human distal radius sections from previous studies [155,202] were used (see Fig. 3.1). The original scans had a resolution of 16.4μm and were taken by Hosseini et al. [202] using a μCT 100 scanner (SCANCO Medical AG, Brüttisellen, Switzerland). Stipsitz et al. [123] segmented and resampled the images to a resolution of 32.8μm. This resolution was chosen to ensure applicability of the material model of Stipsitz et al. [24] (see section 2.2) which was developed for resolutions around 35μm. From 15 specimens in total, two specimens that differed in their bone volume fraction were selected: a low-density (LD) and high-density specimen (HD). The images were uniformly aligned with respect to the volar surface and a cuboid with a square cross section of 7.5mm side length was cropped from the center of the bones (see Table 3.1). The cuboid size was selected according to Ovesy et al. [121,145] with the intention to reduce simulation time while fully capturing the bone damage around the implant. The μCT image of a locking screw (Medartis A-5750; titanium alloy TiAl6V4), that was part of a distal radius fracture fixation system (A-5750; Medartis, Basel, Switzerland), was taken and resampled to 32.8μm from Synek et al. [155] (Skyscan 1173; Bruker, Bilerica, USA). The screw (outer diameter: 2.5mm) was cut to different lengths and was virtually inserted into the center of the segmented bone images in two configurations: either the screw tip was aligned flushed with the outer surface of the dorsal cortex (hereon denoted as 100% insertion depth), or the screw was inserted to 50% of the volar-dorsal cortex distance (hereon denoted as 50% insertion depth). Hence, four different bone-screw specimens were created: a high-density specimen with 50% (HD_50) and 100% (HD_100) screw insertion depth and a low-density specimen with 50% (LD_50) and 100% (LD_100) screw insertion depth (see Fig. 3.1). All image processing steps were performed with Medtool 4.5 (Dr. Pahr Ingenieurs e.U., Pfaffstätten, Austria).

Table 3.1
Dimensions and CT-based morphometrics of the two prepared bone specimens.

Specimen	Side length in mm	Height in mm	Trabecular bone			Cortical bone
			BV/TV in %	Tb.Th[a] in μm	Tb.Sp[a] in μm	C.Th[a] in μm
LD	7.5	14.5	12.5	194±56	939±315	494±135
HD	7.5	20.3	21.4	228±66	811±247	690±234

Note: bone volume fraction (BV/TV), trabecular thickness (Tb.Th), trabecular separaton (Tb.Sp), volar and dorsal cortical thickness (C.Th), low-density specimen (LD), high-density specimen (HD).
[a] Mean ± standard deviation.

3.2.2 Mesh, material and boundary conditions

Based on the segmented bone images with the implanted screw, μFE models were generated. All voxels were directly converted into eight-noded hexahedral elements (C3D8R) with side length of 32.8μm. Isotropic and homogeneous material properties were assigned. Bone was modelled using a damage-based material model recently introduced for efficient large-scale nonlinear μFE analysis [24]. The material model was implemented as a user material (VUMAT) in Abaqus (Abaqus 2022 Dassault Systems, Vélizy-Villacoublay, France) and included a linear-elastic region ($E_0 = 10$GPa and a Poisson's ratio of $v = 0.3$), a damaged region with hardening (hardening modulus $E_H = 0.05E_0$) and a failure region. In the damaged region, material degradation was expressed via local stiffness reduction based on the observed damage. The yield criterion distinguished between tension and compression behavior (damage onset strain in tension $\varepsilon_0^+ = 0.0068$; damage onset strain in compression $\varepsilon_0^- = 0.0089$) and was modelled using an isotropic, quadric damage onset surface (shape parameter $\zeta_0 = 0.3$) [24,123]. Element

deletion was enabled and elements that exceeded the critical damage D_c ($D_c = 0.915$) [24,123] were deleted. The titanium alloy screw was modelled using linear-elastic material properties with an elastic modulus of $E = 115$GPa and a Poisson's ratio of $\nu = 0.3$ [155].

The bone was fixed at the outer surfaces, except for the volar and dorsal surface (see Fig. 3.1). At the screw top, a displacement of 0.2mm was applied in loading direction, while the movement in other directions was constrained. Three load cases were simulated. In tension and compression, the displacement was applied in volar/dorsal direction. For the shear load case, the screw was displaced in distal direction.

The models were generated using Medtool 4.5 and had an element number between five and ten million.

3.2.3 Interface modelling

Four different interface models were applied: general contact (GC), considered as the gold-standard and reference interface model; fully-bonded (FB), assuming bonding at the bone-screw interface; tensionally-strained element deletion (TED), as proposed by Steiner et al. [120] and a novel modification of TED (TED-M), derived from the findings of the contact area investigation (see section 3.1). For the general contact interface, hard contact with a friction coefficient of 0.7 [121,145] was selected and self-contact was excluded for the screw material. With the element deletion technique activated, all contact surfaces were updated in every iteration in order to account for potential interface changes. TED is an interface model that represents contact in a simplified way [120] (see Appendix A for a detailed explanation). Before the actual simulation, a single preliminary simulation ("pre-simulation") with the fully-bonded interface is conducted and evaluated in the linear-elastic region. Interface elements experiencing positive volumetric strain are identified as being strained in tension and are subsequently removed, under the assumption that no tensile stresses can be transferred at the contact interface. Conversely, interface elements undergoing negative volumetric strain are considered to be strained in compression and are retained in the interface, under the assumption that they contribute to the stress transfer between bone and screw. After the removal of disconnected elements resulting from the deletion process, the final nonlinear simulation with the updated interface is performed. TED-M (see Appendix A for details) is a novel approach similar to TED, derived from the insights gained in section 3.1, which revealed a notable change in the contact area throughout the simulation process. TED may not fully capture these contact interface dynamics, as it relies on a single "pre-simulation". TED-M slightly increases the contact area of TED, in an effort to better capture the interface elements that get into contact throughout the entire simulation up to maximum force. It uses the contact interface detected with TED as starting point, but reincludes those interface elements with positive volumetric strain into the contact interface that share at least one node with the interface elements with negative volumetric strain. This approach derives from observations that contact area changes mainly involve neighboring interface elements (see section 3.1).

3.2.4 Simulation

All models were solved with Abaqus Explicit (Abaqus 2022 Dassault Systems) using 29 cores on a dual AMD EPYX 7452 server with 512GB RAM.

In order to minimize computational costs, a simulation time of $t = 0.0005$s was chosen, with results assessed at intervals of 1e-05s. Furthermore, a smooth loading amplitude was applied and bulk viscosity was assigned using the default parameters of Abaqus Explicit. The simulation ensured quasi-static behavior by confirming that kinetic energy did not exceed 5%

of internal energy, except for the initial phase [203]. Consequently, this initial phase was excluded from the results, with evaluations of all simulations (and "pre-simulations") starting once quasi-static conditions were established.

Additional simulations were performed to ensure that variations of voxel size (32.8µm and 72µm) and specimen size (side length of 7.5mm and 9mm) did not influence the main study outcomes (see Appendix B).

3.2.5 Reference model evaluation and contact area analysis

The contact area was examined using the contact output variable CPRESS in the simulations with the GC interface. CPRESS is evaluated at the element nodes and denotes the magnitude of the net contact normal force per unit area. An element was classified as interface element if it contained at least one interface node. A node was called an interface node, if its coordinates were included both in the bone and in the screw element set. An interface node was defined as contact node, when CPRESS > 0. Contact nodes were categorized as permanent, if they contributed to the contact area in all simulation steps, while temporary contact nodes contributed to the contact area in at least one simulation step. The number of interface nodes, contributing to contact, was analyzed at each simulation step to estimate the size of the contact area. Furthermore, changes in the contact area over the simulation time were tracked by measuring the cumulative number of interface nodes contributing to the contact area in at least one simulation step. The contact area analysis only considered the parts of the simulation where quasi-static conditions (kinetic energy $\leq$ 5% of internal energy) were ensured up to the point of reaching maximum force.

3.2.6 Comparison of interfaces and contact area analysis

Simulations with the interfaces FB, TED and TED-M were compared to the reference interface model GC by analyzing deformations, whole-construct stiffness, maximum force and damage distribution within the bone. Deformation plots were generated at maximum force and analysed in a qualitative manner. Whole-construct stiffness was measured by calculating the tangent slope of two prior defined displacement steps that lay in the quasi-static and elastic regime. Maximum force was defined as the peak force, followed by a force decrease of at least 10N. Linear regressions were performed for whole-construct stiffness and maximum force for each loading case individually. The regression line was constrained to pass through the origin to measure the average error of each specific interface method compared to the GC interface. Additionally, relative errors of all simulations in comparison to the simulation with the GC interface were computed. Damage distributions were evaluated, visualized and compared at maximum force. An element was considered as damaged if damage $D > 0$.

All statistical evaluations were performed with Python 3.8 (https://www.python.org/) and the included library SciPy [194]. All figures showing the distribution of damage were created using Paraview (https://www.paraview.org/).

3.3 Results

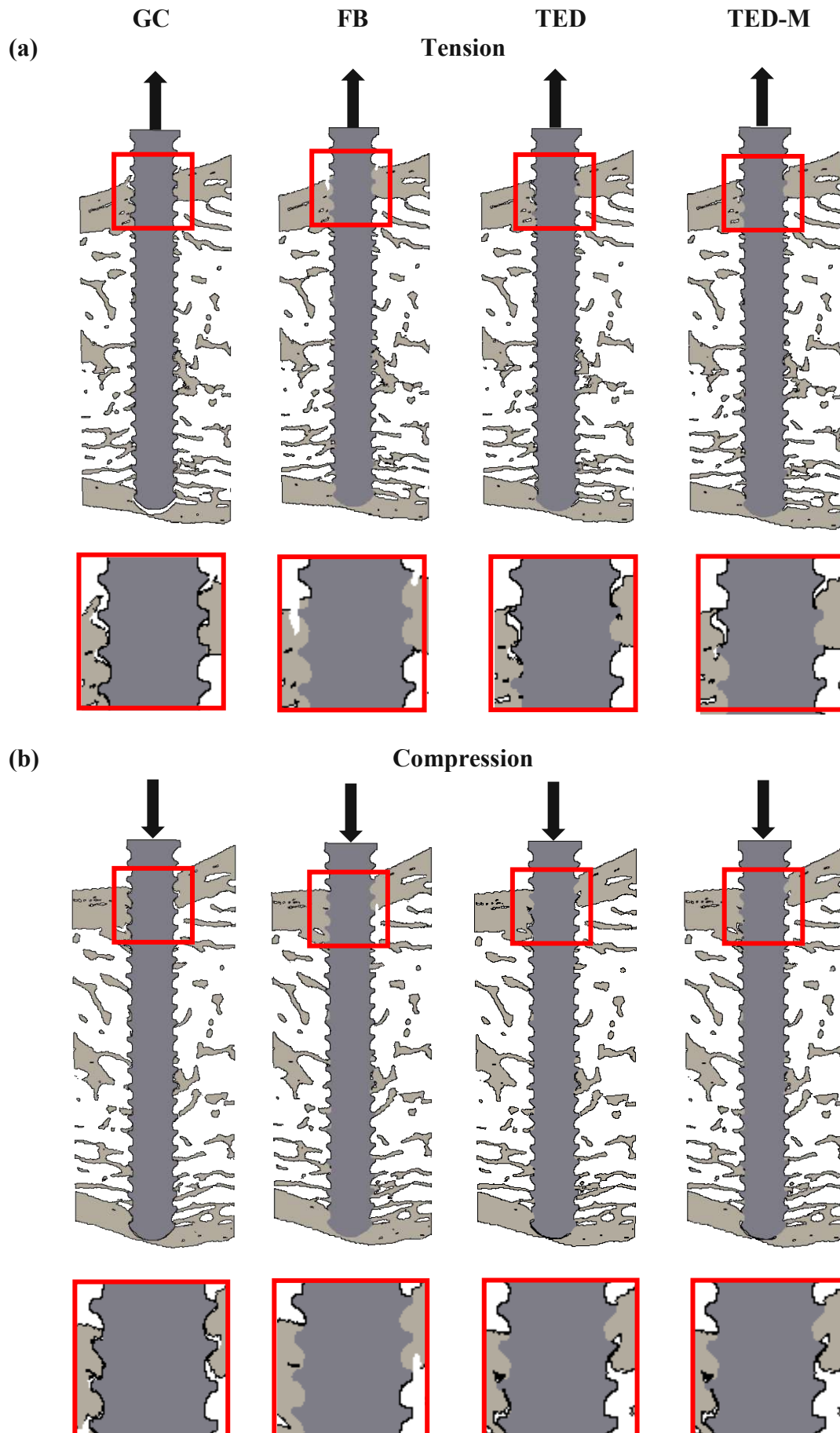### 3.3.1 Reference model evaluation and contact area analysis

Qualitative analysis of the deformed specimens at maximum force revealed that the general contact interface caused an opening of the bone-screw interface at the dorsal and volar cortex in the tension load case (see Fig. 3.2(a) GC). In the compression load case, bone-screw interface openings were harder to detect but could be observed especially at the volar cortex (see Fig. 3.2(b) GC). Similarly, in the shear case, an interface opening was detected at the volar cortex on the proximal side of the screw (see Fig. 3.2(c) GC).
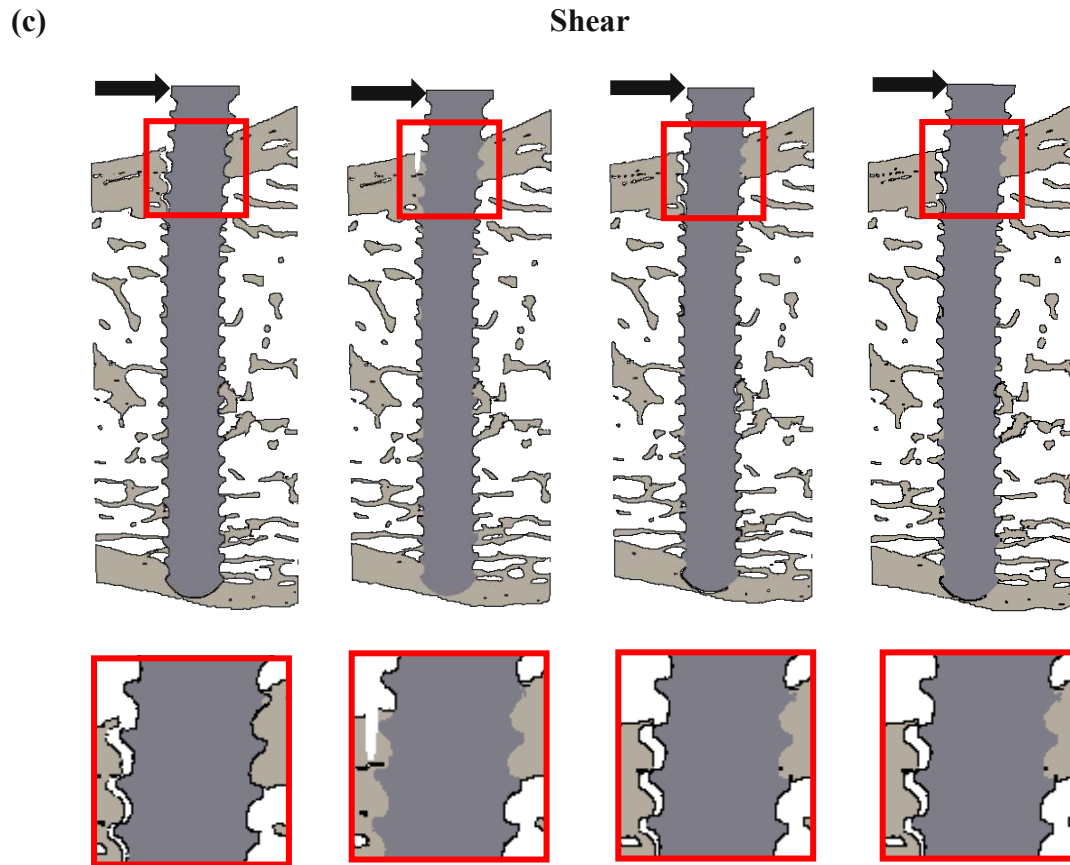
At the starting point of the quasi-static regime, contact area analysis showed that between 38% and 48% of interface nodes were recognized as contact nodes for all specimens and loading cases (see Fig. 3.3 and supplementary material). As the simulation progressed, the number of contact nodes increased between 3% and 12% so that on average 52% of interface nodes contributed to the contact area. Then, the contact area stayed rather constant until a slight drop between 1% and 6% was found just before reaching maximum force.

The cumulative number of identified contact nodes ranged between 42% and 50% for all specimens and loading cases at the beginning of the quasi-static regime (see Fig. 3.3 and supplementary material). Subsequently, it exhibited a rapid increase followed by a slower ascent until it reached final values ranging between 52% and 72% for all specimens.

The number of permanent contact nodes ranged between 42% and 69% for all specimens and loading cases (see Table 3.2). The lowest constancy of contact area was observed in the shear case, the highest in the compression load case. The change in contact area over the simulation time is also shown in Fig. 3.4. Qualitative analysis revealed that the temporary contact nodes were mostly located around the permanent contact nodes.

GC **FB** **TED** **TED-M**

(a)
Tension

(b)
Compression
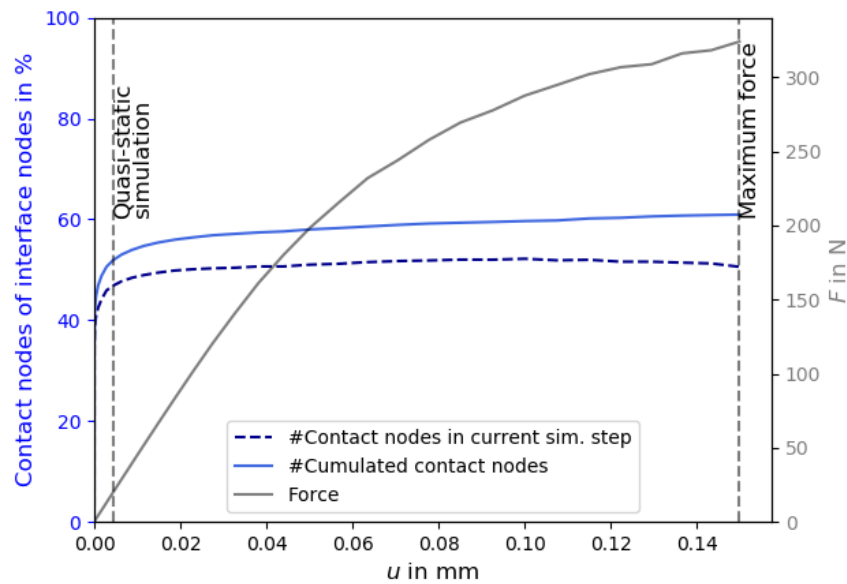
Fig. 3.3 Contact area analysis for one representative specimen (LD_50) in compression. Interface nodes belonged to elements that were included both in the bone and in the screw element set. Contact nodes were defined as interface nodes, when CPRESS > 0. The number of contact nodes in each simulation step is shown over the whole simulation process until maximum force is reached. Furthermore, cumulated contact nodes are illustrated from the beginning of the simulation up to maximum force. They were measured by summing up all identified contact nodes and hence report changes in the contact area.
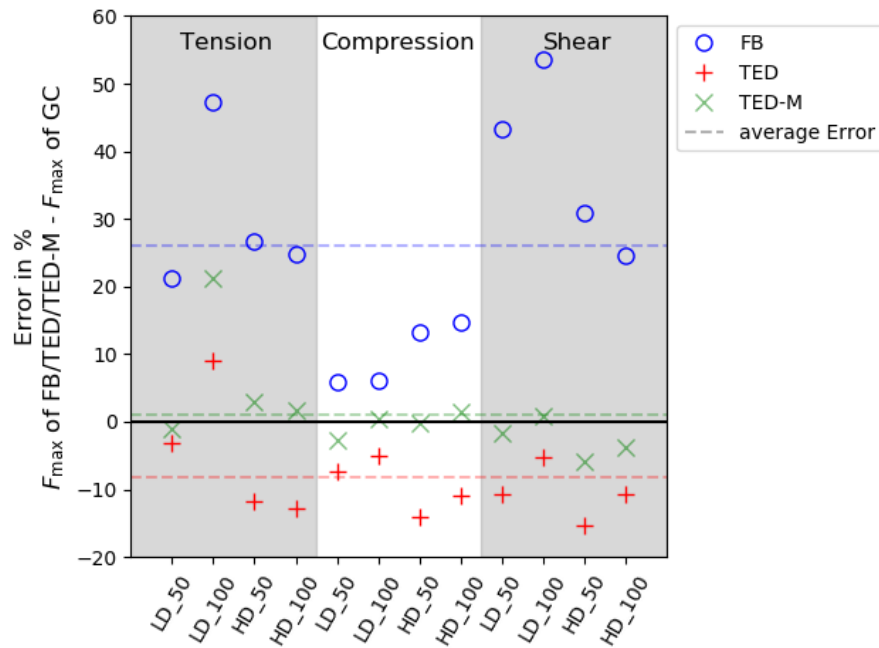
Note: low-density specimen (LD), high-density specimen (HD), 50% screw insertion depth (50), 100% screw insertion depth (100).

Table 3.2
Permanent contact nodes in % of all contact nodes that contributed to the contact area in at least one simulation step from quasi-static conditions to maximum force. Contact nodes were stated as permanent, if they were contact nodes in each reported simulation step from quasi-static conditions to maximum force.

	LD_50	LD_100	HD_50	HD_100
Permanent		**Tension**		
contact	64	55	62	64
nodes in % of all		**Compression**		
contact nodes	69	66	66	66
		Shear		
	43	42	55	54
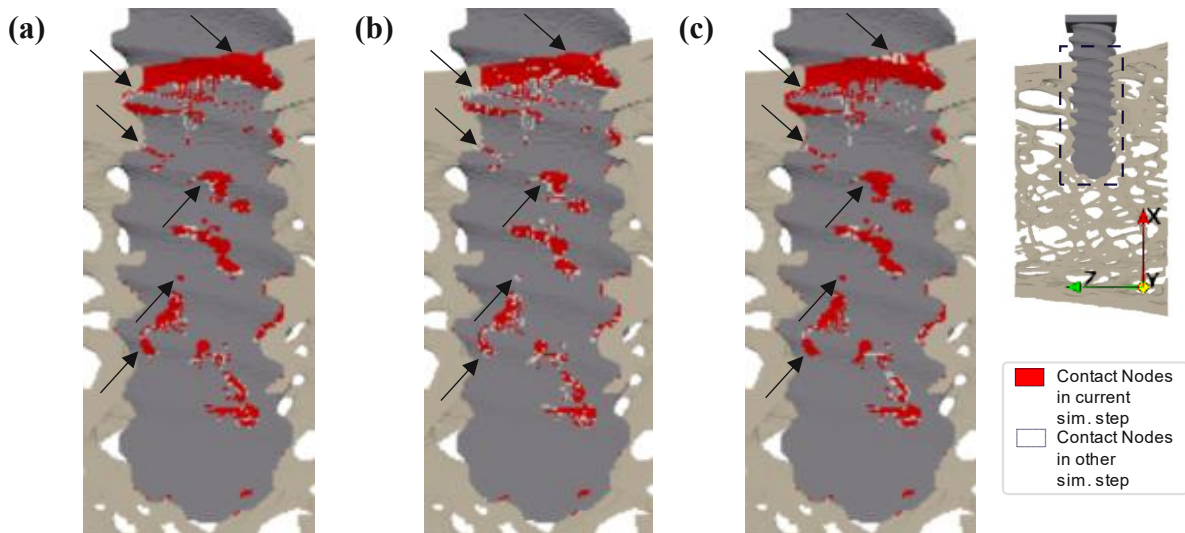
Fig. 3.4 Contact nodes for one representative specimen (LD_50) in compression at the start of the quasi-static simulation (a), in the middle of the simulation (b) and at maximum force (c). Interface nodes were defined as contact nodes, if CPRESS > 0. Contact nodes, that contributed to the contact area in the current simulation step, were marked red while those, that were contact nodes in any other simulation step from quasi-static regime to maximum force, were marked white. The arrows point at regions which did not contribute to the contact area in all presented simulation steps, indicating a change in the contact area over the simulation time.

3.3.2 Deformation

The differences in the deformation between the interface models were particularly evident in the dorsal and volar cortex (see Fig. 3.2 (a-c)). At maximum force in tension, all simplified contact models (FB, TED, TED-M) stayed completely (see Fig. 3.2(a) FB) or mainly (Fig. 3.2(a) TED, TED-M) bonded at the dorsal cortex. At the volar cortex, the FB interface stayed completely bonded, while TED and TED-M mostly replicated the interface opening of the general contact interface. In the compression and shear load case, interface openings were hardly detectable at the dorsal cortex. At the volar cortex, the FB interface stayed bonded while TED and TED-M again replicated the GC interface (see Fig. 3.2(b) and (c) FB, TED, TED-M).

3.3.3 Whole-construct stiffness
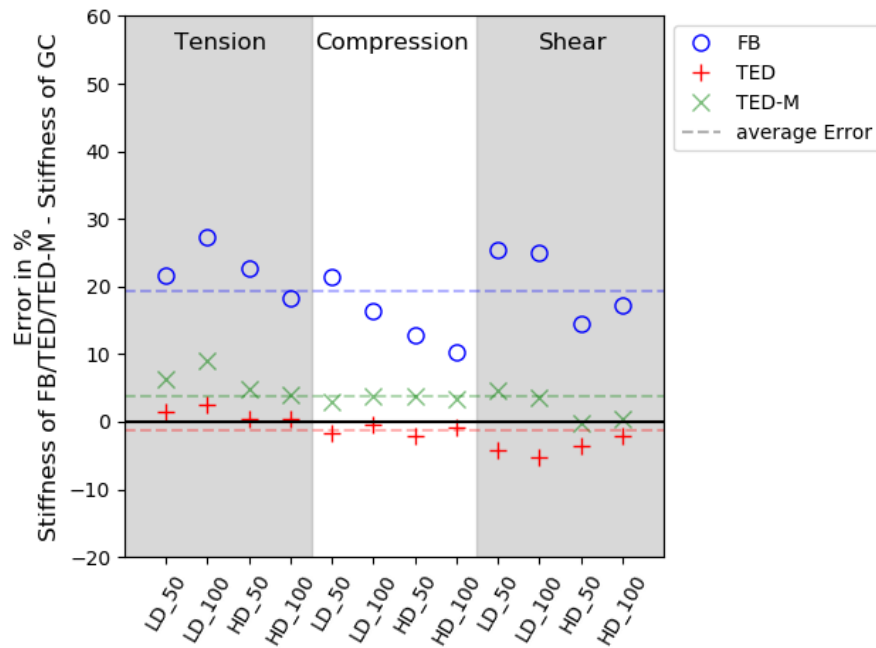
Fig. 3.5 Error of whole-construct stiffness results of FB, TED and TED-M interface simulations in comparison to reference simulation with interface GC in %.

Note: low-density specimen (LD), high-density specimen (HD), 50% screw insertion depth (50), 100% screw insertion depth (100)

(a)

(b)

(c)
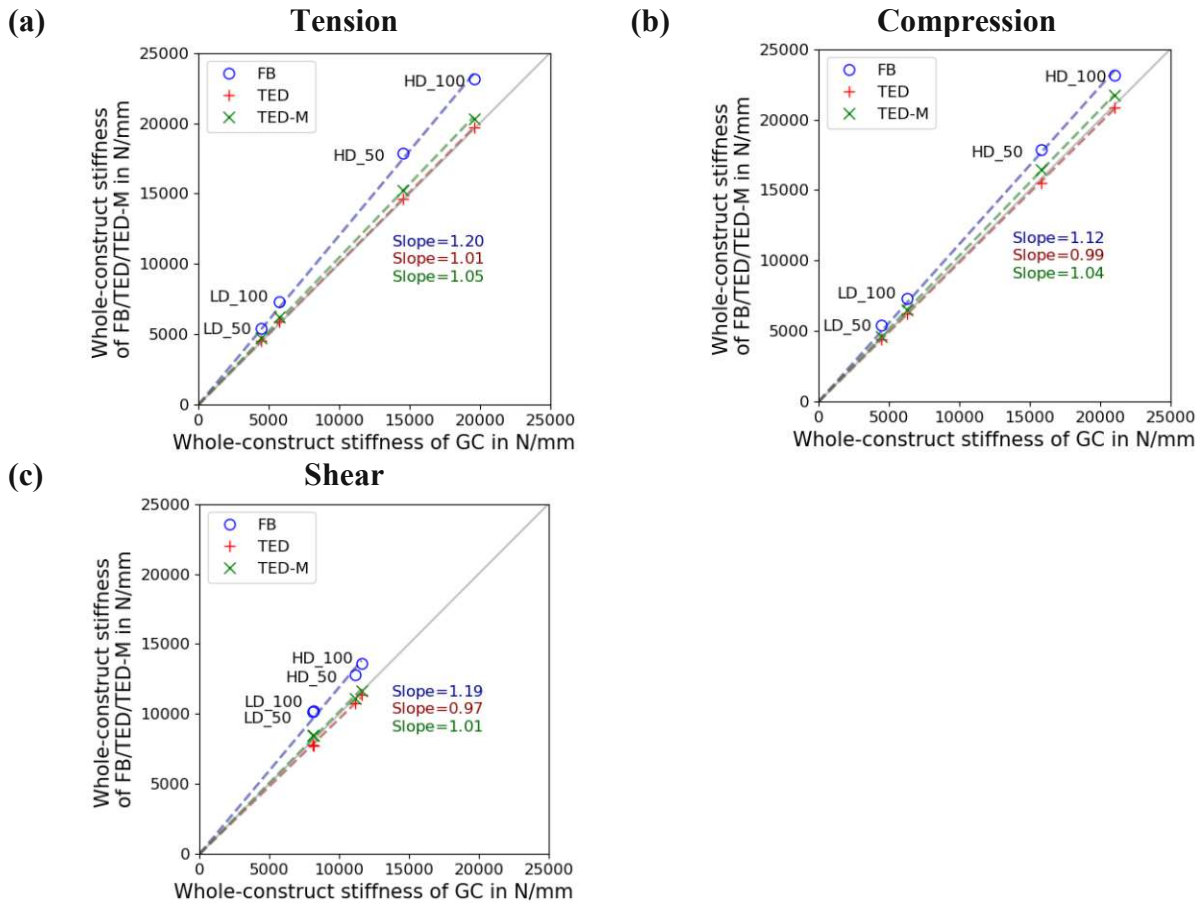
Fig. 3.6 Comparison of whole-construct stiffness results of FB, TED and TED-M interface simulations to stiffness of GC interface for all specimens in tension (a), compression (b) and shear (c).

Note: low-density specimen (LD), high-density specimen (HD), 50% screw insertion depth (50), 100% screw insertion depth (100)

The FB interface simulations of all specimens overestimated the whole-construct stiffness between 10% and 27% with an average error of 19% in comparison to the GC interface (see Fig. 3.5). The overestimation was lowest in compression (12%) and highest in tension (20%) (see Fig. 3.6).

TED achieved the most accurate replication of whole-construct stiffness results among all interface models, with an average underestimation error of only 1%. The error ranged between -5% to 2% over all specimens, meaning that for some the whole-construct stiffness was underestimated, while it was overestimated for others (see Fig. 3.5). Underestimation was highest in the shear case (3%), reduced in compression (1%) and turned into an overestimation in the tension case (1%) (see Fig. 3.6).

TED-M interface simulations demonstrated enhanced whole-construct stiffness replication compared to the FB interface, with an average error of 4% across all specimens and loading cases (see Fig. 3.5). The overestimation in tension (5%) and compression (4%) was higher than in shear (1%) (see Fig. 3.6).

3.3.4 Maximum force

Fig. 3.7 Error of maximum force results of FB, TED and TED-M interface simulations in comparison to reference simulation with interface GC in %.

Note: low-density specimen (LD), high-density specimen (HD), 50% screw insertion depth (50), 100% screw insertion depth (100).

(a)

(b)

(c)
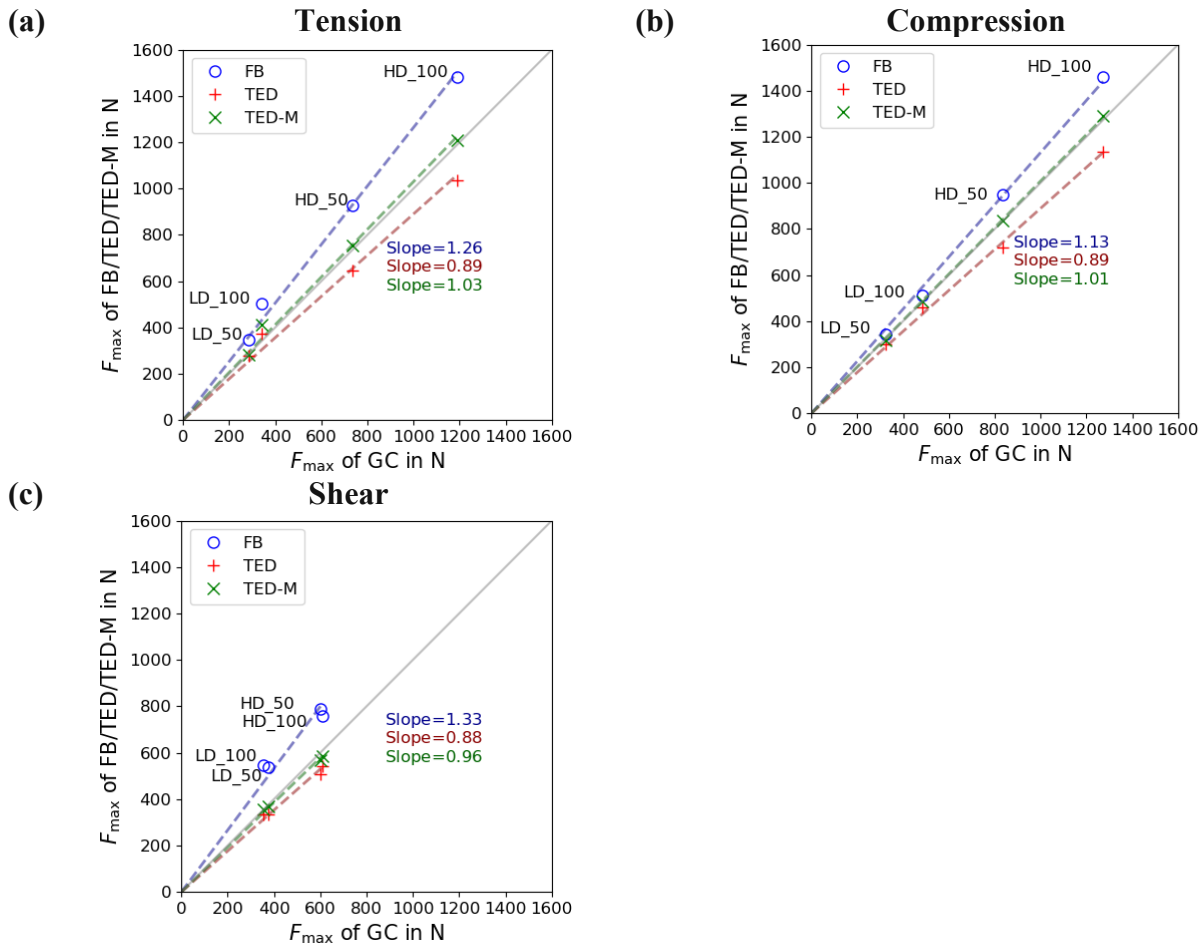
Fig. 3.8 Comparison of maximum force results of FB, TED and TED-M interface simulations to maximum force of GC interface for all specimens in tension (a), compression (b) and shear (c).

Note: low-density specimen (LD), high-density specimen (HD), 50% screw insertion depth (50), 100% screw insertion depth (100)

Simulations with the FB interface led to an overestimation of maximum force for all specimens and all loading cases with an average error of 26% in comparison to the GC interface. Especially in the tension and shear loading cases high errors between 21% and 54% were found. With an average error of 13%, errors were much lower in the compression case (see Fig. 3.7).

TED was able to reduce the maximum force error in comparison the FB interface, but turned the maximum force overestimation into an underestimation. All specimens and all loading cases, except for the low-density specimen with 100% screw insertion depth (LD_100) in tension, showed an underestimation of maximum force ranging between 5% and 15% with the TED interface (see Fig. 3.7).

TED-M improved the maximum force replication in comparison to TED and FB and reduced the average error of all specimens and loading cases to 1%. Except for specimen LD_100 in tension, the maximum force error was by 6% at most. For specimen LD_100 a large overestimation of 21% was observed (see Fig. 3.7). Separation of the loading cases showed that the shear loading case leads to an underestimation of 4% on average, while tension and compression overestimated the maximum force for up to 3% on average (see Fig. 3.8).

3.3.5 Damage distribution

Qualitative analysis of damage showed that the simulation with the FB interface resulted in a different damage pattern in comparison to the simulation with GC for all loading cases and for all specimens (see Fig. 3.9 and 3.10). The amount and the magnitude of damage were higher with the FB interface. Especially the shear load case showed that FB was not able to qualitatively replicate the damage of the GC interface simulation (see Fig. 3.9c and 3.10c). The volar cortex was damaged on both sides of the screw, which was not the case with the GC interface.

TED and TED-M both led to damage patterns that resembled GC better than FB. TED-M showed slightly more damaged regions and also the magnitude of damage was higher. Therefore, TED-M replicated the damage pattern of GC slightly better than TED. The improved damage replication in comparison to FB can be observed in the shear case where the damage was reduced to the distal side of the volar cortex similar to the result of GC. However, the damage distribution still showed differences to GC, particularly in the tension simulation of the high-density specimen with 100% screw insertion depth (HD_100) (see Fig. 3.10a). Damage at the dorsal cortex was observed in both TED and TED-M, despite its absence in GC.
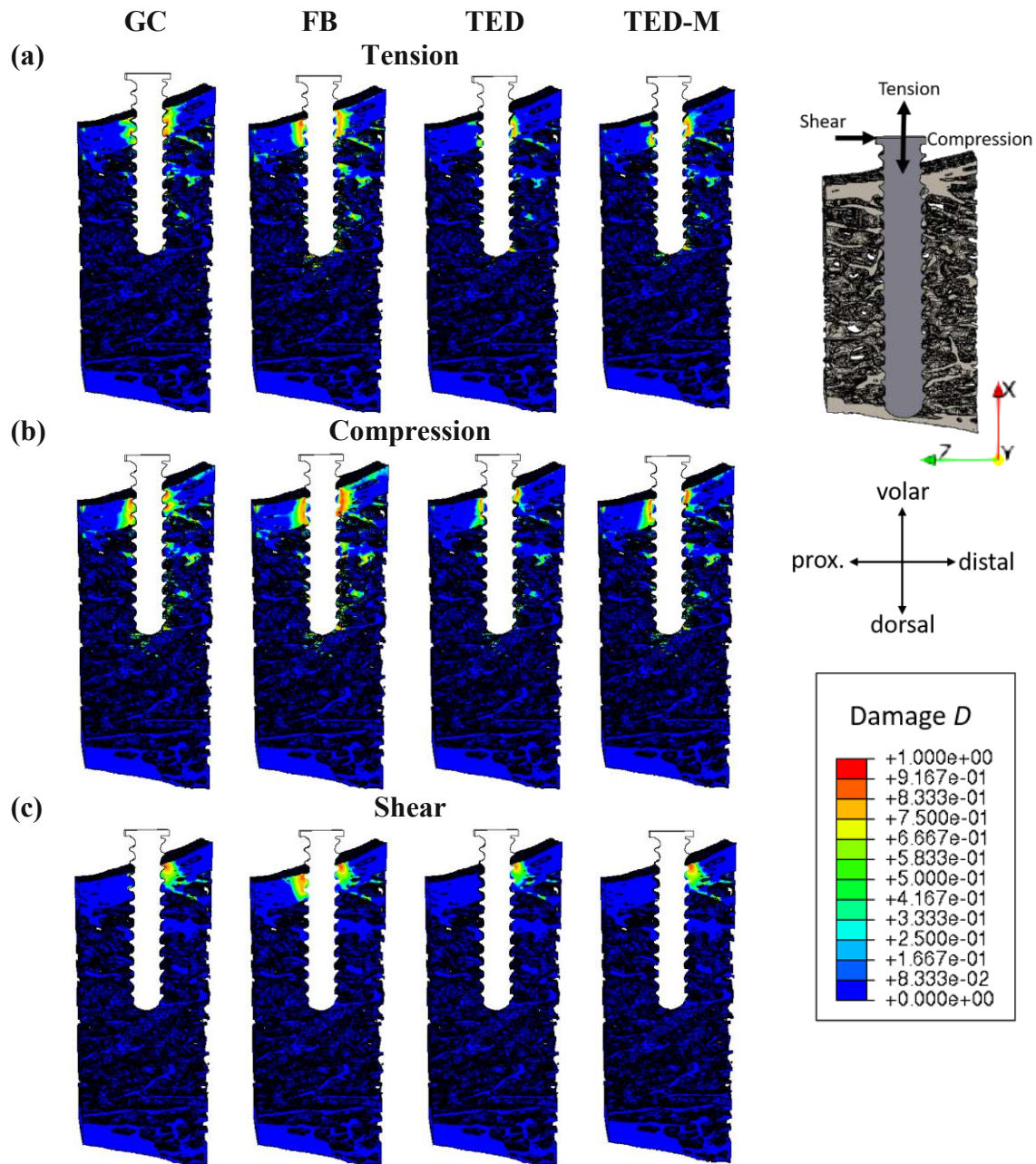
Fig. 3. 9 Damage distribution at maximum force for the high-density specimen with screw insertion depth of 50% for all loading cases tension (a), compression (b), and shear (c).
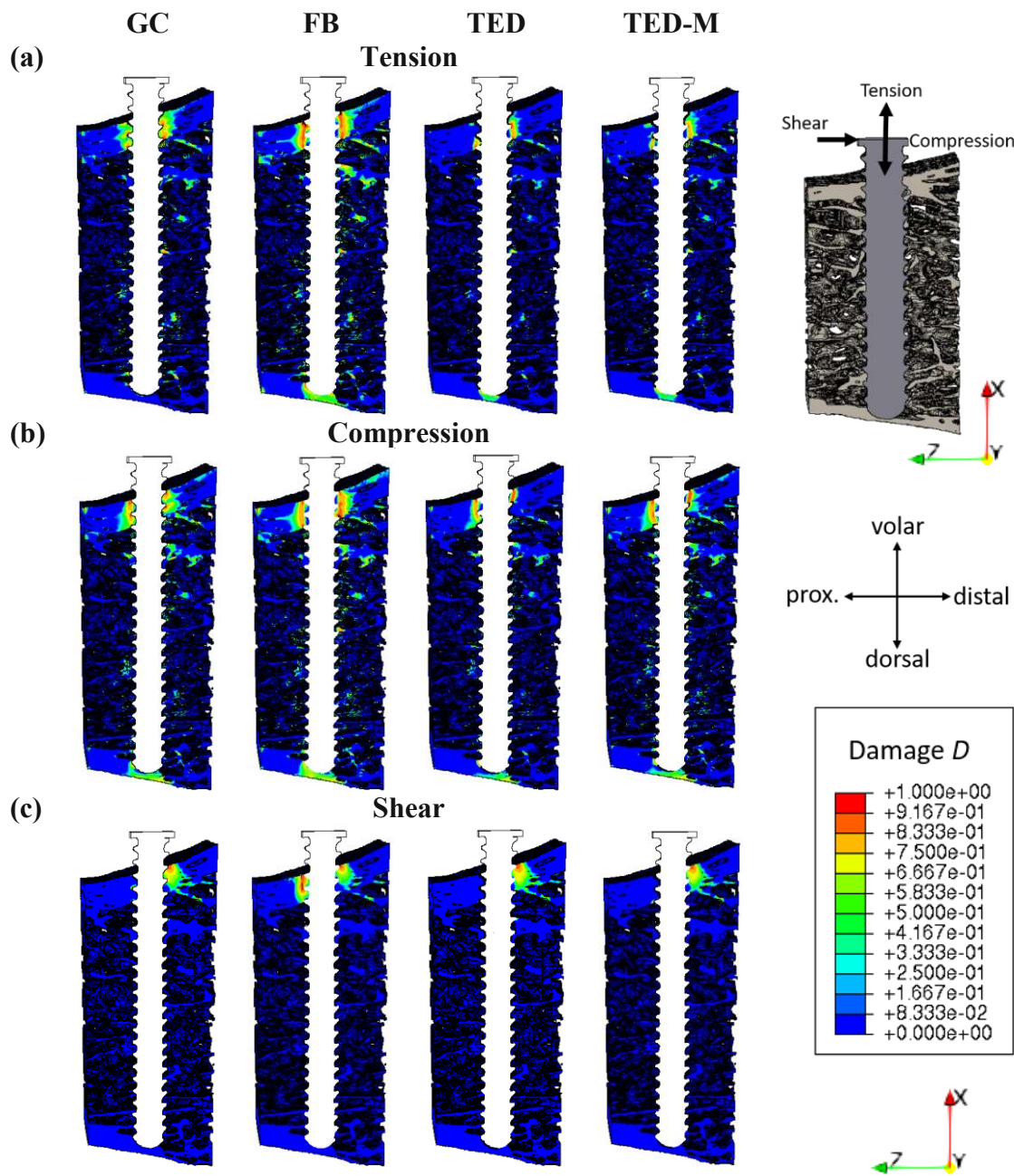
Fig. 3. 10 Damage distribution at maximum force for the high-density specimen with screw insertion depth of 100% for all loading cases tension (a), compression (b) and shear (c).

Note: general contact (GC), fully-bonded (FB), tensionally-strained element deletion (TED), modified tensionally-strained element deletion (TED-M)

3.4 Discussion

This numerical study aimed to compare different simplified interface approaches regarding deformations, whole-construct stiffness, maximum force, and damage using materially-nonlinear µFE simulations of bone-screw systems. General contact in Abaqus Explicit was defined as gold-standard and reference model. The first objective was to evaluate the impact of physical contact modeling, achieved through a comparison between the fully-bonded approach and the general contact model. All specimens and loading cases showed whole-construct stiffness and maximum force overestimations, as well as differing damage patterns. However,

the average error of 19% for whole-construct stiffness and 26% for maximum force of the fully-bonded approach may be acceptable for many applications. The computationally efficient "element deletion" models TED, as presented by Steiner et al. [120], and the novel TED-M model, both enhanced the predictions of the fully-bonded approach and hence enabled efficient and even more accurate predictions of deformations, whole-construct stiffness, maximum force and especially damage patterns.

While the maximum force results of the general contact interface model were generally in line with the µFE results reported in literature [121,122], the whole-construct stiffness results reported by Ovesy et al. [145] were lower than the values of this study (max. 4kN/mm vs. max. 21kN/mm). This mismatch can be explained by several factors, e.g. Ovesy et al. [145] used trabecular bone specimens and inserted a dental implant, while in this study locking screws were implanted into specimens consisting of trabecular bone with cortex.

The whole-construct stiffness predicted with the fully-bonded approach matched the results of Steiner et al. [120] and Wirth et al. [117]. When comparing the whole-construct stiffness results of the fully-bonded model to the general contact model, whole-construct stiffness overestimations up to 27% were reported in this study, while Steiner et al. [120] and Wirth et al. [117] measured whole-construct stiffness overestimations of more than 300% on average when comparing their results to experiments. This mismatch likely results from the peri-implant bone damage occurring from the implantation process, which is included in experiments, but not modelled in this study. Peri-implant bone damage due to screw insertion has already been proven to cause whole-construct stiffness reduction [138–140], hence explaining the large overestimations reported by Steiner et al. [120] and Wirth et al. [117]. These results indicate that physical contact modelling only plays a minor role for predicting whole-construct stiffness in comparison to the reduced mechanical competence caused by peri-implant bone damage.

The relevance of physical contact modelling differs between the load cases. The lowest average errors in whole-construct stiffness and especially in maximum force were measured in the compression load case, where all interface elements at the screw tip retain the screw movement regardless of whether they are bonded or in contact. In contrast, in the fully-bonded tension and shear simulations, the interface elements are bonded to the screw and hence oppose the tension and shear movement, which is not the case in the general contact simulation. In conclusion, physical contact modelling showed importance, as we saw overestimation errors and different damage pattern patterns for all specimens and loading cases. Nonetheless, the overestimations of whole-construct stiffness and maximum force may be acceptable for many applications. For instance, the fully-bonded approach may be appropriate for predicting whole-construct stiffness in the presence of peri-implant bone-damage, considering that peri-implant bone damage likely exerts a larger influence on the results than interface modelling. However, fully-bonded models should be avoided when the aim is to investigate damage patterns.

Although both TED and TED-M enhanced the predictive accuracy of deformations, whole-construct stiffness, maximum force and damage patterns in comparison to the fully-bonded approach, they exhibited performance differences. The interface model TED discriminates between interface elements strained in tension and compression only in a single simulation step in the elastic regime and hence fails to account for the occurring contact area changes. This seems to be sufficient to replicate whole-construct stiffness (average error of 1%) but not maximum force (average error of 8%). Consequently, TED was enhanced to TED-M by expanding the contact area to account for the contact area changes. Since contact analysis revealed that non-permanent contact nodes predominantly surrounded permanent ones, the contact area increase was achieved by including neighboring interface elements of contact

elements to the contact area. TED-M was able to improve the force predictions to an error of 1% on average, but led to slight whole-construct stiffness overestimations (average error of 4%). Nevertheless, neither TED not TED-M could perfectly replicate the general contact model, as evidenced in the damage pattern of the tension load case of the specimens with 100% screw insertion depth. Both TED and TED-M did not delete all elements below the screw tip inducing an incorrect damage prediction. This incorrect damage replication later resulted in an overestimation of maximum force, particularly notable in the low-density sample (LD_100), where the sparse trabecular bone only minimally contributes to the maximum force result. These results indicate that in order to replicate the general contact model more accurately, an interface model that includes a change in the contact elements throughout the simulation is required. Nonetheless, increasing the complexity of the interface model by including repeated contact element deletion comes with the drawback of reduced model efficiency.

The study faces several limitations. Firstly, the study was conducted solely numerical and specified general contact as gold standard. Although the general contact algorithm still remains to be validated to clarify its capability of physical contact replication, its application is common practice in the majority of research studies that implement bone-screw contact [145,203]. The virtual screw insertion process did not consider peri-implant bone damage which might have a large effect on the interface and was found to have high influence at least on the whole-construct stiffness results [120]. Nonetheless, we decided to isolate the contact effects in order to avoid the overlapping of interface modelling and peri-implant damage influences in the results. Furthermore, all μFE models were based on hexahedral voxel elements, which might not be able to perfectly display the bone and screw geometry and hence the contact surfaces. Despite this limitation being inherent to all μFE simulations, the used voxel size was comparable or even smaller than in many similar studies [121,122,145]. The analyses were restricted to small bone regions in order to achieve feasible solving times for the nonlinear simulations. It was ensured that the cropped regions were large enough the capture the effects of the compared interface models [121,145]. Next, the study results are based on the used nonlinear material model, the selected material parameters and resolution proposed by Stipsitz et al. [24] and a commonly used friction coefficient taken from Ovesy et al. [145]. Although the main study outcomes could be replicated for lower resolutions (see Appendix B), the influence of other parameters still needs to be investigated. Lastly, the study was limited to a single screw, two bone specimens with varying densities and two insertion depths.

3.5 Conclusion

This study compared three different simplified interface modelling approaches in materially nonlinear μFE simulations of bone-screw systems regarding deformations, whole-construct stiffness, maximum force and damage distribution using general contact as gold-standard. Overestimations in whole-construct stiffness and maximum force, along with differing damage patterns between the fully-bonded and general contact interfaces, showed the relevance of physical contact modeling. However, the errors of the fully-bonded approach may be acceptable for many applications, particularly if the damage pattern is of minor relevance. The simplified interface models TED and TED-M effectively reduced errors and improved damage pattern predictions, with TED outperforming in whole-construct stiffness prediction and TED-M exhibiting the lowest errors in maximum force. These interface models offer computational efficiency and straightforward implementation in μFE solvers like ParOSol-NL. Consequently, this research study serves as an initial step towards enabling simulations of complete bone-screw implant systems with enhanced accuracy and efficiency beyond the current capabilities.

CRediT authorship contribution statement

Pia Stefanek: Writing – original draft, Visualization, Project administration, Methodology, Investigation.
Dieter H. Pahr: Writing –review & editing, Supervision, Resources, Conceptualization.
Alexander Synek: Writing – review & editing, Supervision, Methodology, Investigation, Conceptualization.

Declaration of generative AI and AI-assisted technologies in the writing process

During the preparation of this work the authors used ChatGPT in order to improve readability and language. After using this tool, the authors reviewed and edited the content as needed and take full responsibility for the content of the publication.

Declaration of competing interest

The authors declare the following financial interests/personal relationships which may be considered as potential competing interests: DP is CEO of Dr. Pahr Ingenieurs e.U. which develops and distributes the software Medtool. PS and AS have no conflicts of interest to declare.

Data availability

Data will be made available on request.

Acknowledgments

Appendix A

Both, TED and TED-M are "element deletion" interface models that represent contact in a simplified way.

In a first step, TED performs a single preliminary simulation ("pre-simulation") with the fully-bonded interface (see Fig. 3.11(a) Step 1). Volumetric strain is evaluated in the linear-elastic regime and interface elements are discriminated based on their volumetric strain value (see Fig. 3.11(a) Step 2). Interface elements, that experience positive volumetric strain, are identified as being strained in tension, while interface elements, undergoing negative volumetric strain, are considered to be strained in compression. Under the assumption that only elements strained in compression contribute to the stress transfer between bone and screw, interface elements, strained in tension, are deleted (see Fig. 3.11(a) Step 3). Only interface elements strained in compression remain in the updated interface. After the removal of newly appeared disconnected elements resulting from the deletion process, the simulation is performed again with the updated interface.

The first two steps of TED-M are equivalent to TED. A single "pre-simulation" is conducted and the interface elements are discriminated based on their volumetric strain value (see Fig. 3.11(b) Step 1 and 2). Conversely to TED, not all elements that were identified to be strained in tension get deleted, but TED-M reincludes some of them back into the contact interface. In step 3, TED-M finds interface elements identified to be strained into tension that have a shared node with interface elements considered to be strained in compression. Those so-called

neighbor-elements of the interface elements strained in compression are reincluded into the updated interface. Only interface elements, that are strained in tension and have no shared node with interface elements strained in compression, get deleted (see Fig. 3.11(b) Step 4). Similar to TED, newly appeared disconnected elements, resulting from the deletion process, get deleted and the simulation with the updated interface is performed again.

a) **TED**
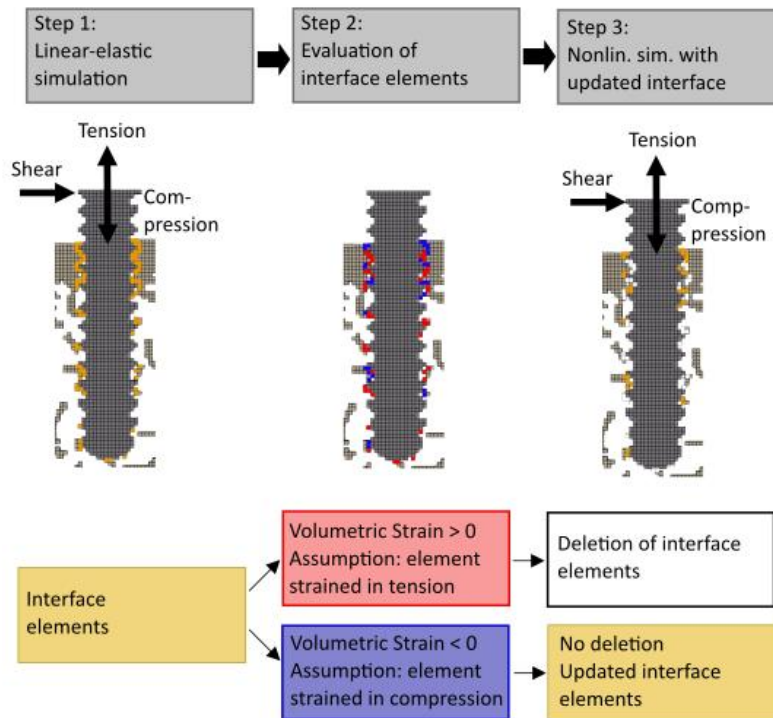
b) **TED-M**
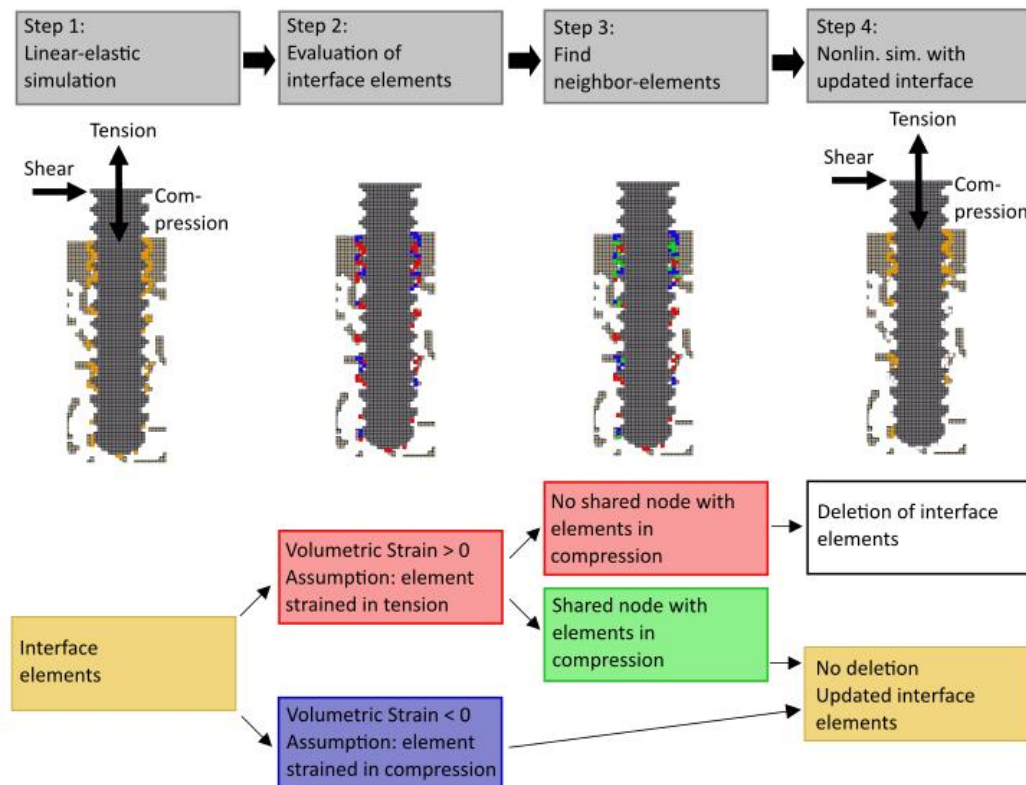
Fig. 3.11 Workflow of TED (a) and TED-M (b). This figure shows the interface models with lower resolution in order to schematically illustrate the differences at the interface. TED deletes interface elements based on their volumetric strain value (volumetric strain > 0 → deletion) in a linear-elastic preliminary simulation and performs the actual simulation with the updated interface. TED-M increases the contact area of TED by reincluding neighboring interface elements of the updated interface.

Appendix B

The influence of the voxel size (32.8μm and 72μm) on the main outcomes of this study was investigated in tension for the low-density and high-density specimen with 50% screw insertion depth (LD_50 and HD_50) (see Fig. 3.12). TED was best in replicating whole-construct stiffness (see Fig. 3.12 (a)), while TED-M showed lowest errors in maximum force (see Fig. 3.12 (b)) for all resolutions and sample sizes. The influence of the specimen size (7.5mm and 9mm) was explored in tension on the high-density specimen with 50% screw insertion depth (HD_50) (see Fig. 3.13). Again, TED exhibited lowest errors in whole-construct stiffness replication (see Fig. 3.13(a)), while TED-M mostly enhanced the maximum force predictions (see Fig. 3.13(b)). These results suggest that both voxel and specimen size variations only had negligible influence the main study outcomes.
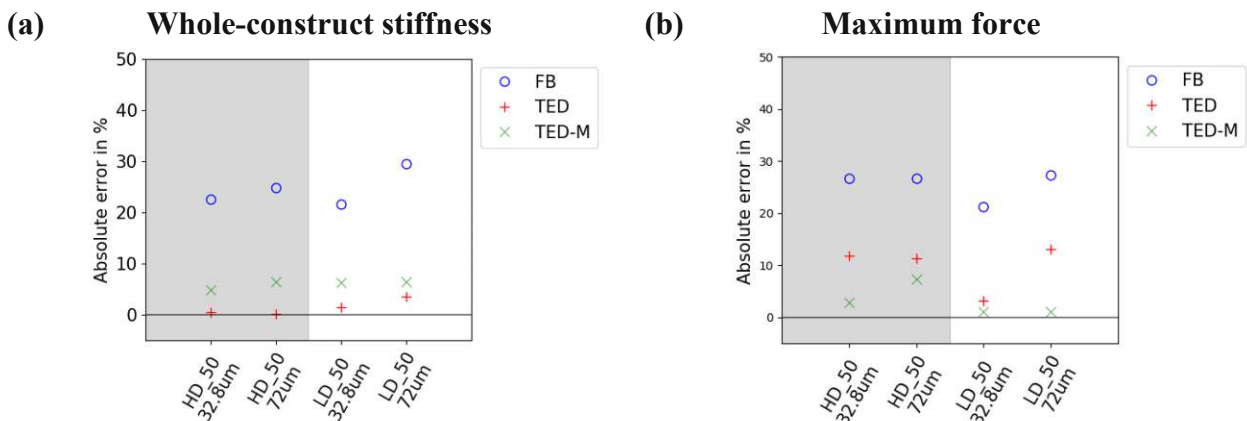
Fig. 3. 12 Absolute error in whole-construct stiffness (a) and maximum force (b) when comparing the simplified interface models fully-bonded (FB), tensionally strained element deletion (TED) and modified TED (TED-M) to the general contact model (GC) for two different resolutions (32.8um and 72um) for the high-density specimen with 50% screw insertion depth (HD_50) and the low-density specimen with 50% screw insertion depth (LD_50) in tension.
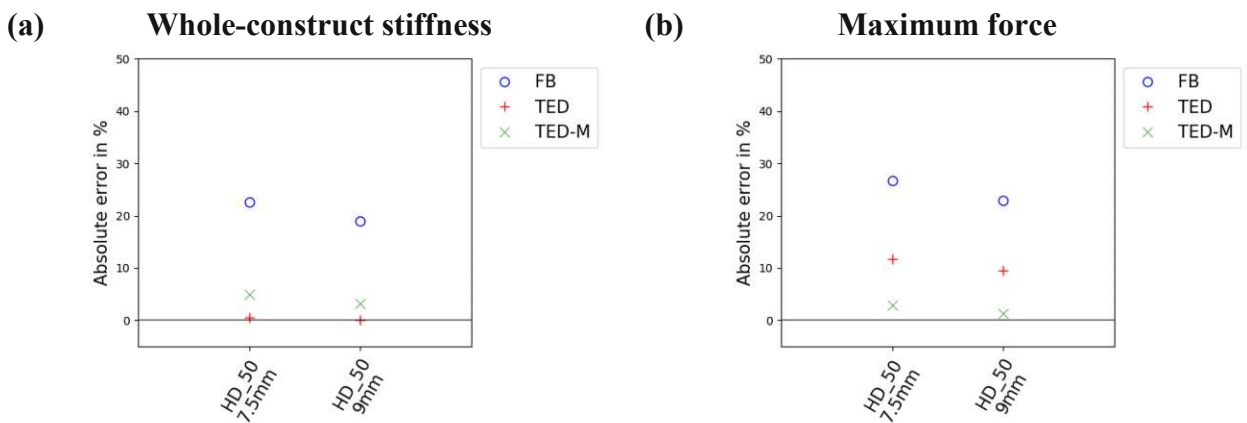
Fig. 3.13 Absolute error in whole-construct stiffness (a) and maximum force (b) when comparing the simplified interface models fully-bonded (FB), tensionally strained element deletion (TED) and modified TED (TED-M) to the general contact model (GC) for two different sample sizes (7.5mm and 9mm) for the high-density specimen with 50% screw insertion depth (HD_50) in tension.

Appendix C. Supplementary data

Supplementary data to this article can be found online at https://doi.org/10.1016/j.jmbbm.2024.106634.

Chapter **4**

Paper 3

Screw pull-out force predictions in porcine radii using efficient nonlinear µFE models including contact and pre-damage

Pia Stefanek, J. D. Silva-Henao, Victoria Fiedler, A. G. Reisinger, Dieter H. Pahr and Alexander Synek

Abstract

Nonlinear micro finite element (µFE) models have become the gold-standard for accurate numerical modeling of bone-screw systems. However, the detailed representation of bone microstructure, along with the inclusion of nonlinear material and contact, and pre-damage due to pre-drilling and screw-insertion, constitute significant computational demands and restrict model sizes. The goal of this study was to evaluate the agreement of screw pull-out predictions of computationally efficient, materially nonlinear µFE models with experimental measurements, taking both contact interface and pre-damage into account in a simplified way. Screw pull-out force was experimentally measured in ten porcine radius biopsies, and specimen-specific, voxel-based µFE models were created mimicking the experimental setup. µFE models with three levels of modeling details were compared: Fully bonded interface without pre-damage (FB), simplified contact interface without pre-damage (TED-M), and simplified contact interface with pre-damage (TED-M+P). In the TED-M+P models, the influence of pre-damage parameters (damage zone radial thickness and amount of damage) was assessed and optimal parameters were identified. The results revealed that pre-damage parameters highly impact the pull-out force predictions, and that the optimal parameters are ambiguous and dependent on the chosen bone material properties. Although all µFE models demonstrated high correlations with experimental data ($R^2 > 0.85$), they differed in their 1:1 correspondence. The FB and TED-M models overestimated maximum force predictions (mean absolute percentage error (MAPE) > 52%), while the TED-M+P model with optimized pre-damage parameters improved the predictions (MAPE < 17%). In conclusion, screw pull-out forces predicted with computationally efficient, materially nonlinear µFE models showed strong correlations with experimental measurements. To achieve quantitatively accurate results, precise coordination of contact modeling, pre-damage representation, and material properties is essential.

Keywords: micro finite element modeling, bone-screw systems, bone-screw contact,

predamage due to screw insertion, efficient materially-nonlinear simulations

4.1 Introduction

While experimental testing with cadaver bones remains the gold standard in bone-implant research, finite element (FE) analysis offers significant advantages. Experiments are time-consuming, costly, and require scarce human or animal tissue. In contrast, once an FE model is created and validated, parameters can be easily modified, allowing for efficient testing of various implant configurations on the same subject. This makes FE analysis ideal for systematic optimization studies. FE models provide a deeper understanding of local stress and strain, helping to identify potential weaknesses and failure points [12,13,63]. Micro-FE (µFE) models, based on high-resolution CT images, are currently considered the benchmark for bone-screw modeling. They capture the local bone microstructure, including trabecular networks and screw geometry, which is crucial for accurately predicting mechanical behavior and anchorage quality [19–21]. Nonetheless, the detailed representation of microstructure increases µFE model sizes and computational demands. Moreover, recent studies highlight the need to incorporate nonlinearities in bone-screw simulations, as both bone failure and bone-screw contact interactions are nonlinear processes [121,122,146]. However, including these nonlinearities, increases model complexity and computational requirements even more.

One possibility to deal with high computational demands in µFE are specialized solvers developed to solve large-scale problems with several millions of elements (e.g. FEAP [201], Faim (Numerics88 Solutions Ltd, https://bonelab.github.io/n88/index.html), ParOSol [25], ParOSol-NL [24]). These solvers are highly efficient for solving large-scale problems, but in turn often only support linear-elastic or simplified nonlinear material laws. As they generally lack the ability to include nonlinear contact mechanics, some studies have proposed simplified contact models to overcome these limitations, while maintaining computational efficiency [120,204]. While the relevance of interface modeling in bone-screw µFE simulations has already been demonstrated [204], modeling of peri-implant bone damage due to pre-drilling and screw insertion may be even more critical for accurate predictions [120,146]. Various studies have reported that the screw insertion causes damage in the surrounding bone [138–141]. Steiner et al. [139] localized and quantified the screw insertion related pre-damage by comparing µCT scans of human femoral bone before and after screw insertion. They found that the damaged region depends on the screw thread depth and can extend up to a radial distance of 0.9mm, with the most significant damage occurring within a distance of 0.3mm.

However, in general it remains unclear how to define the radial thickness of the damage zone in a µFE simulation and how to model the compromised mechanical properties inside the damage zone. Consequently, literature research reveals a variety of pre-damage modeling approaches. Ovesy et al. [145] and Zhou et al. [146] conducted nonlinear simulations incorporating the screw insertion process, but this method is computationally intensive and feasible only for small models. To maintain computational efficiency, other studies used linear simulations and defined damage zones around the screw with a uniformly reduced elastic modulus [115,120,137]. Damage zones were selected with radial thicknesses between 0.16mm [137] and 0.9mm [120] around the screws. Inside these zones, the bone elastic modulus was reduced between 17% [115] and 99.5% [137]. As all studies used bones from different species (human, rat) and anatomical locations (spine, femur, hind limb), they selected different elastic moduli for undamaged bone. Hence, this wide range of damage estimation could also result from variations in the selection of material properties. To the author's knowledge, no study has yet tried to implement this simplified pre-damage modeling approach in computationally efficient µFE simulations with nonlinear material.

The objective of this study was to assess the correlation between screw pull-out predictions from computationally efficient, materially nonlinear µFE models and experimental measurements, while considering both contact interface and pre-damage. In a first step, the parameters of a simplified pre-damage model were identified dependent on the elastic modulus selection. In a second step, the predicted maximum force of different computationally efficient µFE models was compared to experiments and damage distributions were evaluated.

4.2 Material and methods

Figure 1 provides an overview of this study. The experimental part was conducted by Silva-Henao et al. [78]. Screws were inserted into porcine distal radius biopsies after pre-drilling, and experiments were conducted to assess maximum pull-out force. µCT scans of the pre-drilled samples were cropped and used to generate nonlinear µFE models that replicated the experiments. After determining optimal pre-damage parameters for different elastic moduli, three different interface and pre-damage modeling combinations were implemented, and the predicted maximum force was compared to experimental measurements. Additionally, damage distributions at maximum force were evaluated.

4.2.1 Experimental data

The study is based on the experimental data of Silva-Henao et al. [78], where ten porcine distal radii were selected for pull-out experiments (see Fig. 1). A conventional drill-press with a modified core driller was used to extract a cylindrical sample (20mm in diameter and height) with a centered 2mm pilot hole from each bone. Following the implantation procedure described in Ovesy et al. [121], a universal mechanical testing machine (ZwickiLine Z2.5, ZwickRoell GmbH & Co. KG, Ulm, Germany) was used to implant a locking screw (outer diameter: 2.5mm; titanium alloy TiAl6V4; A-5750, Medartis Inc., Basel, Switzerland). The screw was inserted mono-cortically to a depth of 15mm. Tensile force-controlled loading (loading rate: 50N/s) was applied using a custom-designed testing apparatus. The samples were laterally fixed in a sample holder, while cyclic loading was applied to the screw via a clamp positioned in 2mm distance to the bone. The loading started with a pre-conditioning phase including 20 loading cycles between 0N and 15N which was followed by a pause of 1s. Afterwards, a cyclic overloading phase followed, where the load amplitude was increased by 1N per cycle while maintaining a minimum load of 15N. The loading was applied until the screw was entirely pulled out of the bone samples.
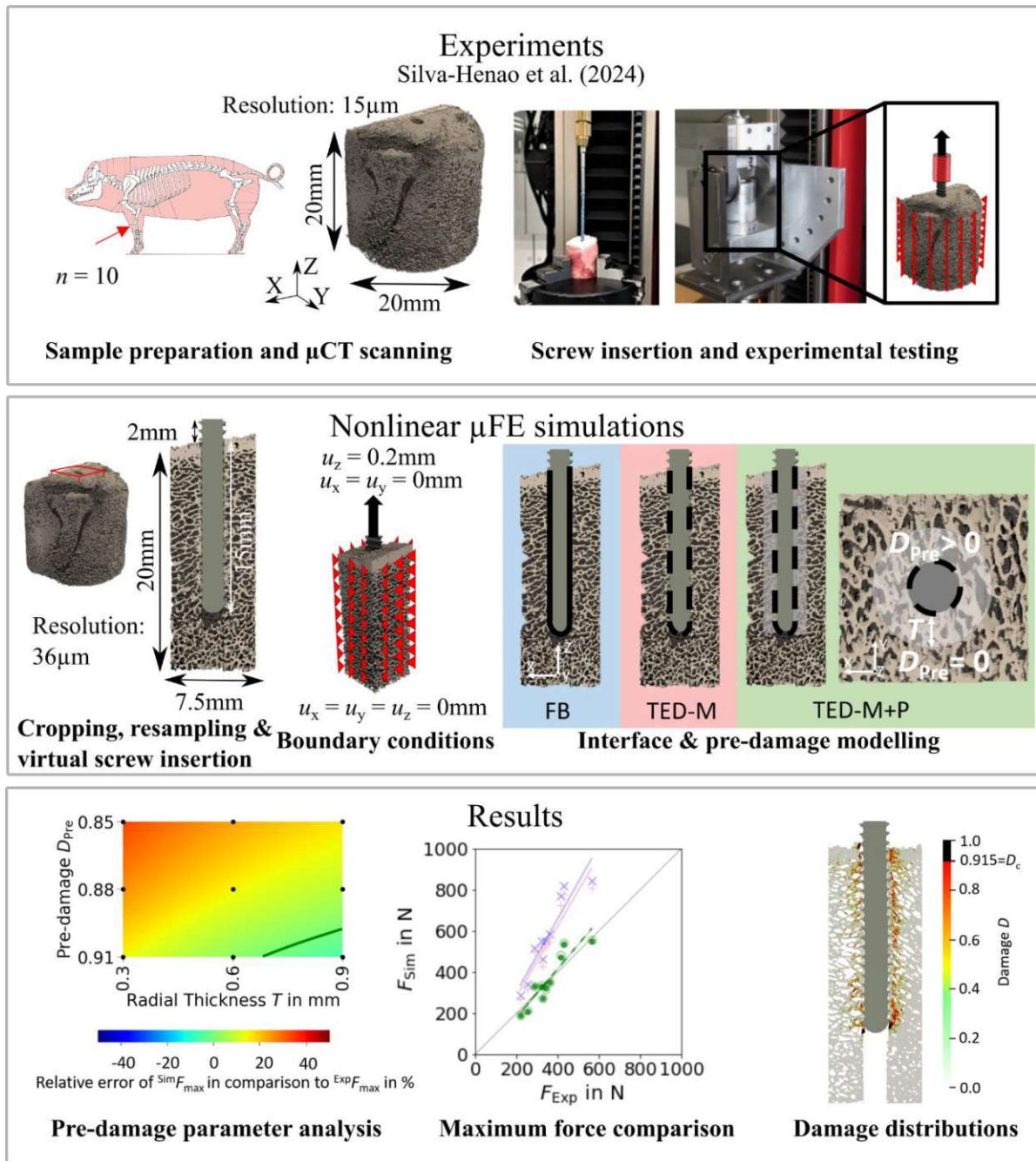
Fig. 4.1 Study outline. Predicted pull-out force of nonlinear µFE simulations of bone-screw models was compared to experiments. The simulations included both a simplified contact interface and a simplified pre-damage model. The photographs from the experimental procedure were taken from Silva-Henao et al. [78].

4.2.2 Image processing

µCT images with a resolution of 15µm were acquired from the unloaded, pre-drilled bone samples using a SkyScan1173 µCT scanner (Bruker, Bilerica, USA) (90kV source voltage, 60µA source current, 1250ms exposure time, 1mm aluminum filter). In order to reduce image noise, the µCT images were smoothed using a Gaussian filter (σ=1; kernel size=2x2x2). The samples were aligned along the pre-drilled screw axis, and cuboids with a square cross section (7.5mm side length) were cropped from the bone center (see Fig. 1). The cuboid size was determined following Ovesy et al. [121,145] to minimize simulation times while ensuring to fully capture bone damage around the screw. Single-level thresholding was applied to binarize the images. A µCT image (resolution: 14.8µm; SkyScan1173, Bruker, Bilerica, USA) of the

same locking screw that was used for the pull-out experiments, described in section 2.1, was taken from a previous study [155] and cropped to a length of 17mm. Bone and screw images were resampled to a resolution of 36µm, as the later applied material model of Stipsitz et al. [24] (see section 2.3) was developed for resolutions of this magnitude. The screw was virtually inserted to a depth of 15mm into the center of the segmented bone images to mimic the experimental conditions. The samples had a bone volume fraction range of 18.2% to 38.3% and their mean cortical thickness varied between 237µm and 1124µm. All image processing steps and morphometric evaluations were performed with Medtool 4.5 (Dr. Pahr Ingenieurs e.U., Pfaffstätten, Austria).

4.2.3 Mesh, material and boundary conditions

The segmented bone images with the virtually inserted screw were used as geometrical input to generate µFE models. Each voxel was converted into eight-noded hexahedral elements (side length: 36µm). The number of elements varied between 5.8 and 10.3 million. Material properties were assumed to be homogeneous and isotropic. For the bone material, a nonlinear damage-based material model [24,123] especially developed for efficient nonlinear µFE analysis was selected. The model consists of a linear-elastic region, a damaged region, and a failure region. In the linear-elastic region, an elastic modulus $E = 4.6$GPa and a Poisson's ratio of $\nu = 0.3$ were selected. As material parameters proposed by Stipsitz et al. [24,123] ($E = 10$GPa) were identified for human rather than porcine bone, the elastic modulus was taken from Costa et al. [119], who found the best fit between µFE predicted and experimental axial forces on a porcine bone sample using $E = 4.6$GPa. The transition from the linear to the nonlinear, damaged regime was modeled using an isotropic, quadric damage onset surface (shape parameter $\zeta = 0.3$) which differentiates between tension and compression. Since Morgan and Keaveny [205] showed that yield strains remain relatively constant across species, damage onset strains in tension and compression were taken from Stipsitz et al. [24,123] and kept constant (damage onset strain in tension $\varepsilon^+ = 0.0068$; damage onset strain in compression $\varepsilon^- = 0.0089$), while damage onset stresses were scaled according to the selected elastic modulus [122,145]. In the damaged region, isotropic material hardening ($E_H = 0.05 E_0$) [24,123] was included, and material degradation, found by back-projection of the current stress state on the damage onset surface, was modeled via local stiffness reduction according to observed damage levels. When the critical damage threshold $D_c = 0.915$ [24,123] was exceeded, local failure was modeled by reducing the elastic modulus to a residual value close to zero. For the titanium alloy screw, linear-elastic material properties, with an elastic modulus of $E = 115$GPa and a Poisson's ratio of $\nu = 0.3$ [155] were assumed.

The boundary conditions were selected to mimic the experimental conditions (see Fig. 1). The nodes located on the four lateral sides of the bone were fully constrained. At the screw top, a displacement of 0.2mm was applied along the screw axis, while the nodes were constrained in all other directions. The displacement value of 0.2mm was selected since it was enough to observe a drop in the force-displacement curve in all simulations. The displacements obtained from the simulations could not be directly compared to the experimentally measured displacements, as only crosshead displacements were measured in the experiments. Additionally, cropping the specimen geometry in the µFE models influenced the displacement results.

All µFE models were generated with the software Medtool 4.5 (Dr. Pahr Ingenieurs e.U., Pfaffstätten, Austria).

4.2.4 Interface modeling

Three types of µFE models with different interface and pre-damage combinations (see Table 1) were compared: a fully-bonded interface without pre-damage (FB), a modified tensionally-strained element deletion (TED-M) [120,204] interface without pre-damage, and a TED-M interface with pre-damage (TED-M+P). The fully-bonded interface assumes perfect bonding at the bone-screw interface nodes. TED-M represents a modification of the tensionally-strained element deletion (TED) interface model introduced by Steiner et al. [120], which imitates contact in a simplified way. It is based on a preliminary linear-elastic simulation ("pre"-simulation) with a fully-bonded bone-screw interface. Interface elements under positive (tensional) volumetric strain are removed, assuming no tensile stress transfer at the bone-screw interface. Elements under negative (compressional) volumetric strain are retained, as they contribute to stress transfer between bone and screw. Finally, the actual simulation with the updated interface is conducted. Stefanek et al. [204] extended the model of Steiner et al. [120] to TED-M which enhances the accuracy of maximum force predictions. In an attempt to better account for occurring contact area changes throughout the simulation process, TED-M slightly expands the contact area found with TED by reincluding neighboring interface elements of contact elements in the contact area.

4.2.5 Pre-damage modeling

Pre-damage was modeled by defining a cylindrical damage zone with a radial thickness T, where a pre-damage value of bone D_{Pre} ($0 < D_{Pre} < D_c$) was set (see Fig. 1). This approach is slightly different to other simplified pre-damage models reported so far, where the pre-damage was defined as elastic modulus reduction in linear elastic µFE models. Bone-screw research done so far could not provide conclusive guidelines on how to set the pre-damage value (D_{Pre}) and the thickness of the pre-damage zone. Hence, the influence of these parameters on the maximum force was investigated. As we hypothesized that the selection of material properties also affects maximum pull-out force, the influence of reducing and increasing the elastic modulus was also investigated.

To test the influence of pre-damage parameters on maximum pull-out force, 27 different combinations of pre-damage value (D_{Pre}= 0.85, 0.88, 0.91), radial thickness (T = 0.3mm, 0.6mm, 0.9mm) and elastic modulus (E_{red}=3.6GPa, E=4.6GPa, E_{inc}=5.6GPa) were evaluated for each specimen. The parameter ranges of D_{Pre} and T were set following observations in literature [120] and considering the requirements of the used material law ($D_{Pre} < D_c$).

To visualize the error in the µFE predicted maximum pull-out force for each parameter combination, heat maps (cubic interpolation) were generated, covering the parameter space. The error between µFE models and experiments was defined as ($^{Sim}F_{max} - {^{Exp}F_{max}}$)/ $^{Exp}F_{max}$. Isolines were evaluated to indicate parameter combinations with a relative error of zero. In cases where no parameter combination led to an error of zero, the parameter combination with lowest relative error was indicated.

To identify optimal per-damage parameters for all specimens, a mean heat map was created by calculating the mean relative error of all specimens for the nine parameter combinations and each elastic modulus. From the isoline of the mean heat map, two parameter sets were extracted for each elastic modulus: one with minimal radial thickness (Min. T) and one with minimal damage (Min. D_{Pre}). These parameter combinations were then used to perform µFE simulations for all specimens, and to compare the µFE predictions with the experimental measurements.

Table 4.1
Description of all three compared interface and pre-damage combinations.

Name	FB	TED-M	TED-M+P
Schematic illustration			
Interface	Fully-bonded	Modified tensionally-strained element deletion[a]	Modified tensionally-strained element deletion[a]
Pre-damage	None	None	Pre-damage value $D_{Pre} > 0$ in cylindrical zone around screw with radial thickness T

[a] [120,204]

The fully-bonded (FB) interface assumes bonding between bone and screw, while the modified tensionally-strained element deletion (TED-M) interface deletes selected elements at the interface to better replicate bone-screw contact. The TED-M interface is combined with a simplified pre-damage model. A cylindrical region with a radial thickness T is selected, where a pre-damage value $D_{Pre} > 0$ is assigned.

4.2.6 Simulation

All µFE models were solved with ParOSol-NL [24,25] using up to 126 cores on a dual AMD EPYC 7763 64-core processor with 1TB RAM. Simulations were performed until a drop of force of at least 15N was observed.

4.2.7 Comparison between µFE and experiments

Maximum force values of all µFE simulations (FB, TED-M, and TED-M+P) were compared to experimental results using linear regressions. The following parameters were computed: slope, intercept, coefficient of determination (R^2), concordance correlation coefficient (CCC), mean absolute percentage error (MAPE), and root mean squared error (RMSE). Damage distributions were evaluated, visualized, and compared for all µFE simulations at maximum force.

All statistical evaluations were conducted with Python 3.8 (https://www.python.org/) and the included library SciPy [194]. The figures showing the damage distribution were generated with the software ParaView (https://www.paraview.org/).

4.3 Results
4.3.1 Influence of radial thickness, pre-damage value and elastic modulus

As expected, µFE simulations with lower elastic modulus led to lower maximum force predictions, and vice versa (see Fig. 2 (B) and supplementary material). Both higher pre-damage and larger radial thickness of the pre-damage zone led to lower maximum force predictions. The results differed for each specimen (see supplementary material), but tendentially an elastic

modulus of E_{red}=3.6GPa led to underestimation of experimental maximum force, whereas an elastic modulus of E_{inc}=5.6 GPa led to overestimations.

The influence of the chosen elastic modulus and pre-damage parameters on the relative error is also visualized in the heat maps (see Fig. 2 (C) and supplementary material). The isolines in the heatmap indicated a variety of parameter combinations leading to a relative error of zero percent, depending on the selected elastic modulus (see Fig. 2 (C)) and specimen (supplementary material). All zero-error isolines showed a similar relation of pre-damage value and radial thickness of the pre-damage zone. Setting the pre-damage to a higher value required smaller radial thickness to achieve zero maximum force error and vice versa.

Mean heat maps (see Fig. 3 (A)) showed isolines for E_{red}=3.6GPa and E=4.6GPa, while for E_{inc}=5.6GPa none of the investigated pre-damage parameter combinations led to a mean error of zero. Hence, the optimal pre-damage parameter combination included both the highest evaluated pre-damage value 0.91 and the highest evaluated radial thickness 0.9mm. The optimal radial thickness as well as the optimal pre-damage value were lower for E_{red}=3.6GPa than for E=4.6GPa for both evaluated criteria Min. D_{Pre} and Min. T (see Fig. 3 (B)). While the optimal pre-damage value ranged between 0.85 and 0.88 for E_{red}=3.6GPa, it needed to be increased between 0.904 and 0.91 to reach best outcomes for E=4.6GPa. Radial thickness was evaluated to be ideal between 0.3 and 0.628mm for E_{red}=3.6GPa and between 0.741 and 0.9mm for E=4.6GPa.
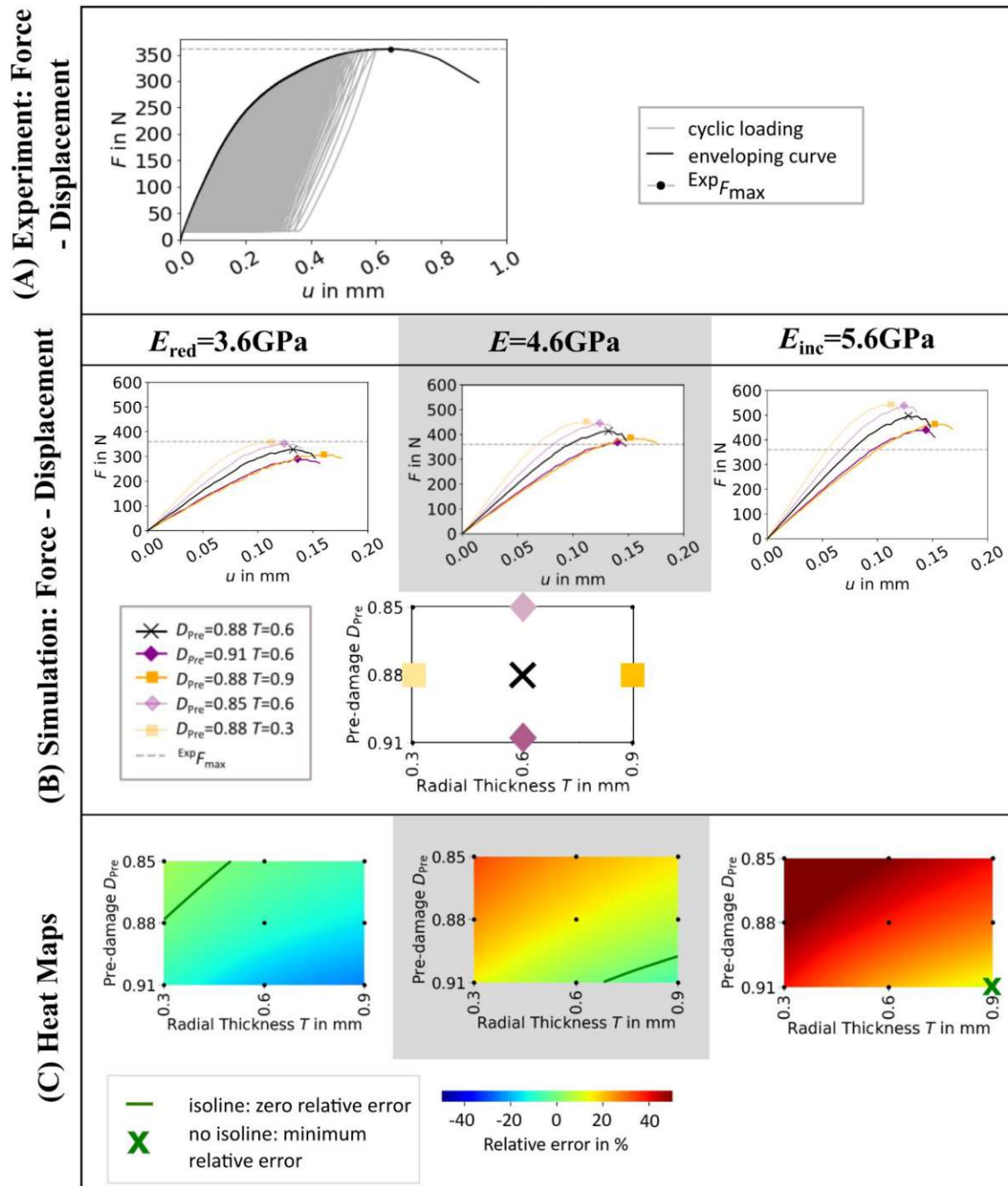
Fig. 4.2 Experimental force-displacement curve (**A**), simulated force displacement curves for different values of radial thickness T and pre-damage value D_{Pre} (**B**) and heat maps showing the relative error in maximum force (**C**) of one representative specimen (S10). Simulated force-displacement curves and heat maps are shown for three different elastic moduli of bone material E_{red}=3.6GPa, E=4.6GPa, and E_{inc}=5.6GPa. The simulated force-displacement curves (**B**) show a selection of five parameter combinations of T and D_{Pre}. In the heat maps (**C**), green isolines mark the parameter combinations of pre-damage D_{Pre} and radial thickness of damage zone T, where the relative error in maximum force between simulation and experiment is zero. In case that no parameter combination can be found that leads to zero relative error, the parameter combination where the relative error is minimal is marked by a green cross.
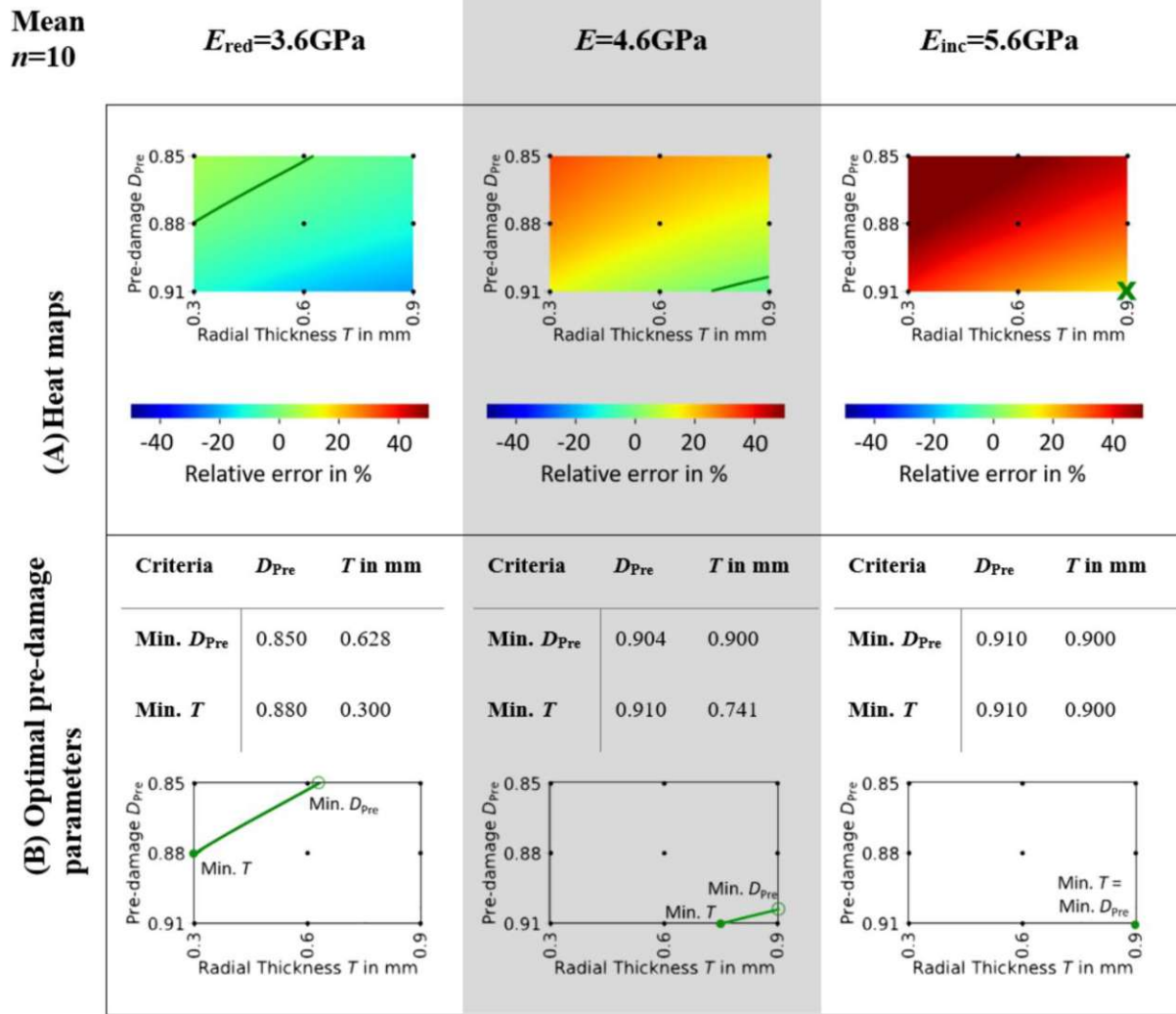
Fig. 4.3 Mean heat maps (**A**) and optimal pre-damage parameters (**B**). The heat maps (**A**) illustrate the mean relative error across all specimens for three different elastic moduli of bone material: E_{red}=3.6GPa, E=4.6GPa, and E_{inc} =5.6GPa. Isolines indicate the parameter combinations of pre-damage D_{Pre} and radial thickness of damage zone T where the relative error in maximum force between simulation and experiment is zero. The optimal pre-damage parameters based on the minimal pre-damage (Min. D_{Pre}) and the minimal radial thickness criteria (Min. T) are summarized in (**B**). The unfilled green markers 'o' denote the points where the isoline parameters are evaluated based on the minimum pre-damage criteria, whereas the filled green markers '●' denote the points where the isoline parameters are evaluated based on the minimum radial thickness criteria.

4.3.2 Comparison of maximum force

Both models without pre-damage implementation (FB, TED-M) showed high correlations (R^2>0.86) to experiments but failed to predict a good 1:1 fit, as confirmed by high RMSE (>211N) and MAPE (>51%) and low CCC (<0.43) (see Fig. 4 and Table 2). Models with optimal pre-damage implementations (TED-M+P) according to Fig. 3(B), achieved comparable R^2 correlations (>0.85) but improved the 1:1 fit to experiments for E_{red}=3.6GPa and E=4.6GPa (RMSE<50N; MAPE<12%; CCC>0.89). Only minor differences were observed between E_{red}=3.6GPa and E=4.6GPa as well as between different criteria for optimal pre-damage parameter selection (Min. T or Min. D_{Pre}). For E_{inc}=5.6GPa, TED-M+P improved the maximum force predictions in comparison to the models without pre-damage. However, TED-M+P with E_{inc}=5.6GPa showed inferior results in comparison to the TED-M+P models with E_{red}=3.6GPa and E=4.6GPa.
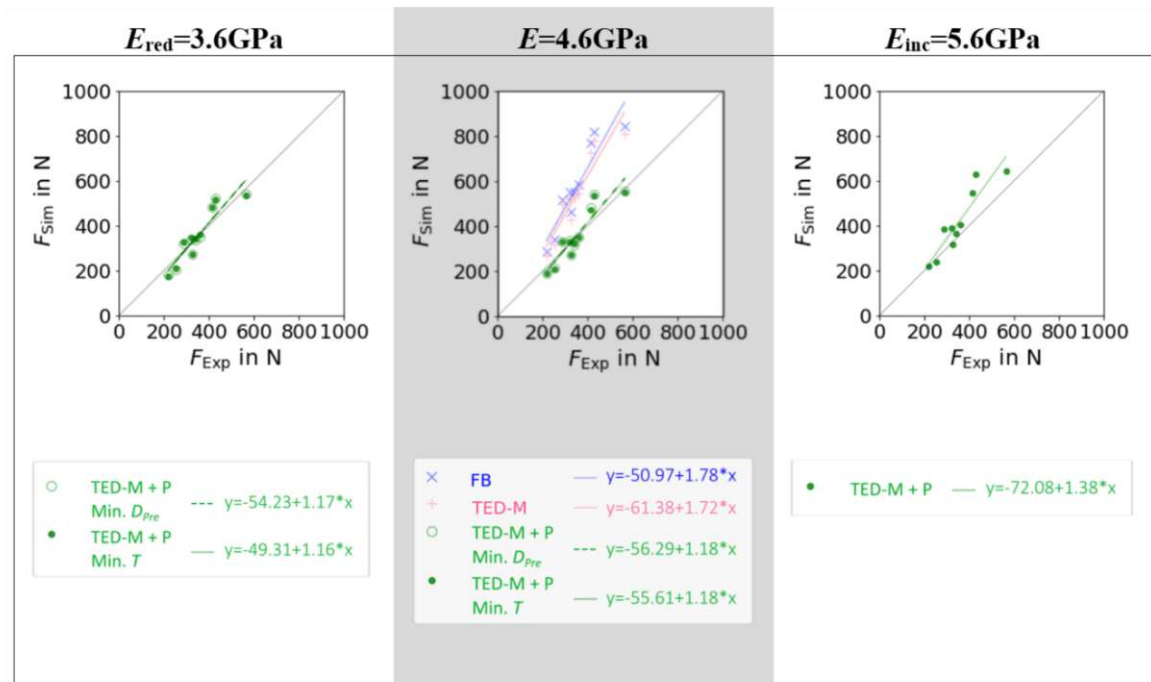
Fig. 4.4 Linear regressions between µFE predicted (F$_{Sim}$) and experimentally measured (F$_{Exp}$) maximum force for three different elastic moduli of bone material E$_{red}$=3.6GPa, E=4.6GPa, and E$_{inc}$ =5.6GPa and three different pre-damage and interface combinations: a fully-bonded interface without pre-damage (FB), a simplified contact model [120,204] without pre-damage (TED-M), and the same contact model with pre-damage (TED-M+P). Optimal pre-damage parameters were selected based on two criteria defined in Fig. 3: minimal pre-damage (Min. D$_{Pre}$) and minimal radial thickness criteria (Min. T).

Table 4.2

Comparison of linear regressions from Fig. 4 using different error metrics to evaluate the goodness of fit.

		RMSE in N	MAPE in %	CCC	R^2
E_{red}=3.6GPa	TED-M+P Min. D_{Pre}	46.74	11.55	0.905	0.864
	TED-M+P Min. T	**46.27**	11.60	**0.906**	0.863
E=4.6GPa	FB	242.58	61.20	0.371	**0.866**
	TED-M	211.18	51.93	0.429	0.865
	TED-M+P Min. D_{Pre}	49.91	11.68	0.895	0.855
	TED-M+P Min. T	47.26	**11.17**	0.904	0.865
E_{inc}=5.6GPa	TED-M+P	89.26	17.37	0.7658	0.860

Note: root mean squared error (RMSE), mean absolute percentage error (MAPE), concordance correlation coefficient (CCC) and coefficient of determination (R^2).

For each metric, the model showing the best results (lowest error or highest correlation) was formatted as bold text.

4.3.3 Comparison of damage distributions

Overall, the models FB and TED-M exhibited similar damage distributions (see Fig. 5). Most damage could be observed in bone material close to the screw but not directly attaching the screw core. The extent of damage reduced gradually from the screw axis towards the outer surface. However, a more detailed comparison revealed that the FB model displayed slightly higher damage and differences in the regions of critical damage. In contrast, the TED-M+P models all showed the implemented pre-damage zone close to the screw, with a radial thickness depending on the optimal pre-damage parameters (see Fig. 5 and 6). For TED-M+P models

with E_{red}=3.6GPa, screw pull-out led to a visible formation of additional damage around the predefined damage zone. In contrast, for TED-M+P models with E=4.6GPa and E_{inc}=5.6GPa, the screw pull-out did not cause any additional damage outside the pre-damage zone.
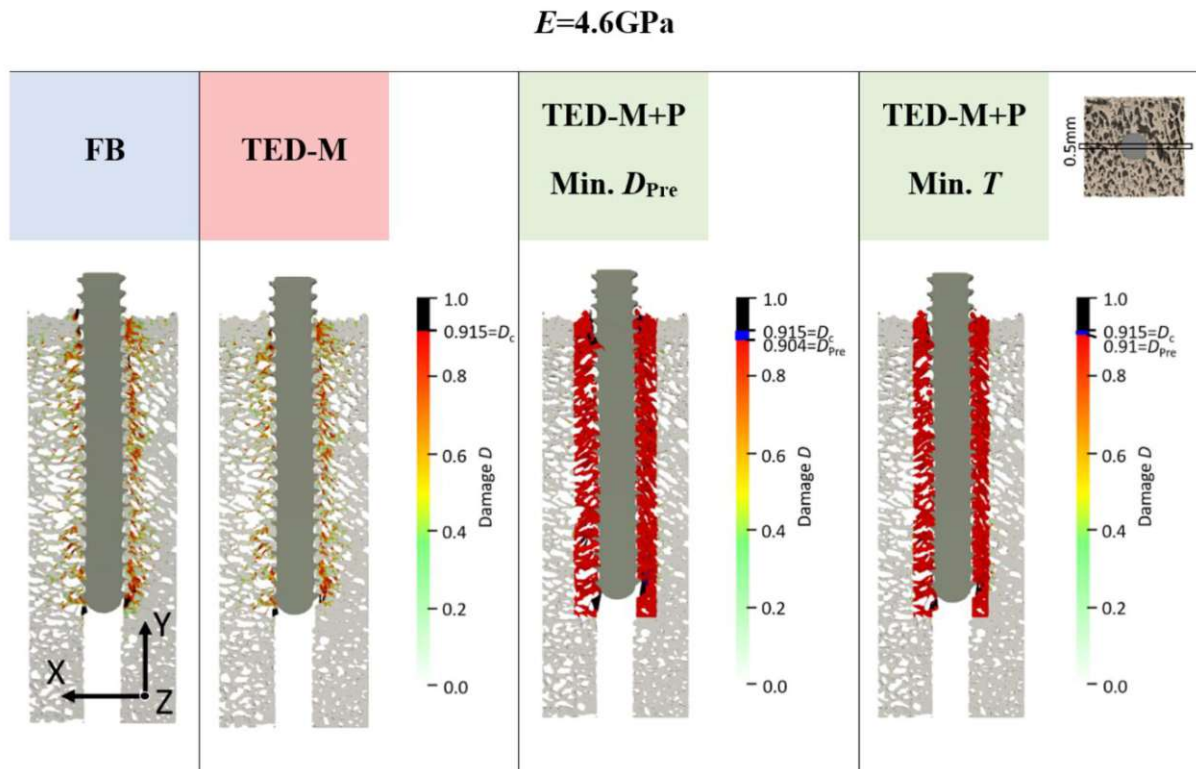
Fig. 4.5 Damage at maximum force of one representative specimen (S10) for E=4.6GPa and for all interface and pre-damage combinations: a fully-bonded interface without pre-damage (FB) and a simplified interface method [120,204] without pre-damage (TED-M) and with pre-damage (TED-M+P). A displacement scaling factor of 5 was used, and optimal pre-damage parameters were selected based on two criteria defined in Fig. 3: minimal pre-damage (Min. D_Pre) and minimal radial thickness criteria (Min. T). For the TED-M+P, the color bar includes blue regions between the pre-damage value D_Pre in the damage zone and the critical damage D_c.
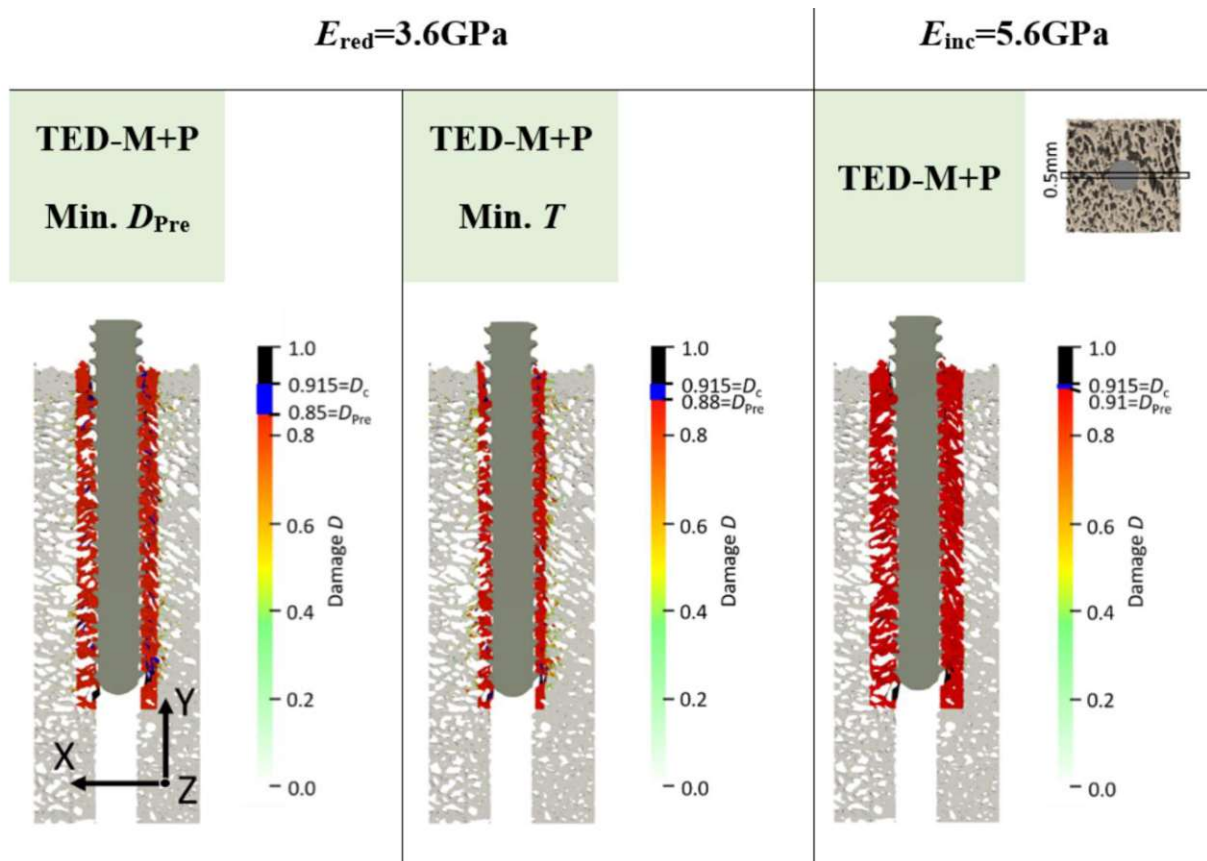
Fig. 4.6 Damage at maximum force of one representative specimen (S10) for the two elastic moduli E_{red}=3.6GPa and E_{inc}=5.6GPa. All models included a simplified interface method [120,204] with pre-damage (TED-M+P). A displacement scaling factor of 5 was used, and optimal pre-damage parameters were selected based on two criteria defined in Fig. 3: minimal pre-damage (Min. D_{Pre}) and minimal radial thickness criteria (Min. T). For the TED-M+P, the color bar includes blue regions between the pre-damage value D_{Pre} in the damage zone and the critical damage D_c.

4.4 Discussion

The goal of this study was to evaluate the agreement of screw pull-out force predictions of computationally efficient, materially nonlinear µFE models with experimental measurements, taking both contact interface and pre-damage into account. Across all µFE model variations - whether pre-damage or contact interface was implemented or not - the predicted maximum forces showed a strong correlation with experimental data. However, the selection of pre-damage parameters emerged as particularly critical for achieving quantitatively accurate predictions.

The optimal pre-damage parameters identified via evaluation of the mean heat map isolines generally aligned with previous studies. For an elastic modulus of 3.6GPa and the investigated parameter range, the evaluated ideal radial thickness was between 0.3mm and 0.63mm, while for 4.6GPa and 5.6GPa, it was between 0.74mm and 0.9mm, which is similar to the radial thickness values selected from Steiner et al. [120] (0.6mm – 0.9mm) and Chevalier et al. [115] (0.4mm). Torcasio et al. [137] and Steiner et al. [120] selected higher damage values (>0.98) than the pre-damage values evaluated in this study (0.85 to 0.91). However, all compared studies differed from this study in various aspects (material law, contact implementations, predicted mechanical parameters). Furthermore, the pre-damage value in this study was restricted by the critical damage D_c= 0.915 of the used material law. The heat maps revealed that radial thickness of the pre-damage zone, pre-damage value, and elastic modulus selection all influenced maximum force screw pull-out predictions. A higher radial thickness reduces the

need for a high pre-damage value, and vice versa. In a similar manner, a lower modulus decreases the maximum force and allows for lower pre-damage parameters, while a higher modulus has the opposite effect. Hence, optimal pre-damage parameters are not unique and cannot be chosen independently. Accurate modeling of pre-damage requires identification of the correct, specimen-specific material properties as well as experimental determination of at least one pre-damage parameter (radial thickness or pre-damage value). In addition, it must be kept in mind that multiple other parameters of the µFE model (e.g. voxel size, contact model) and pre-processing steps (e.g. segmentation) can quantitatively affect maximum force predictions. Pre-damage parameters must therefore always be considered as specific for a given µFE modeling and workflow, rather than generally applicable.

All different interface and pre-damage combinations showed similar correlations (R^2>0.85) consistent with comparable studies by Ovesy et al. [121] (R^2>0.91), Panagiotopoulou et al. [122] (R^2>0.93) and Zhou et al. [146] (R^2=0.79) using fully nonlinear models and standard commercial FE solvers. However, the models differed in their 1:1 fit to experimental maximum force results. The fully-bonded interface without pre-damage highly overestimated the maximum force predictions (MAPE=61%), and the TED-M model only slightly improved the predictions (MAPE=52%). In contrast, the TED-M+P models were able to improve the predictions and enabled a good 1:1 fit to experimental results, especially for E_{red}=3.6GPa and E=4.6GPa (MAPE<12%). The TED-M+P model for 5.6GPa showed slightly higher errors (MAPE=17%), likely due to a suboptimal elastic modulus selection. Although this study results suggest a strong impact of pre-damage modeling on screw pull-out force prediction, other studies still reached accurate results with good 1:1 correspondence without accounting for pre-damage at all [121,122,146]. Hence, simple nonlinear models without pre-damage implementations can still yield good correlations and 1:1 correspondence with experimental measurements on a structural level. This is in line with the results of this study, which showed that various modeling aspects (contact interaction, elastic modulus, pre-damage value and radial thickness) can be used to tune the 1:1 agreement of the models on a structural level (here: maximum pull-out force). However, especially for an in-depth analysis of bone-screw mechanical behavior beyond the structural level, these modeling aspects must be separated and correctly implemented.

Despite similar screw pull-out force predictions with various combinations of pre-damage parameters, differences between the models were evident in the damage distributions. FB and TED-M showed only slightly different damage distributions with damage gradually decreasing with larger distance from the screw. The pre-drilling reduced the influence of the contact interface on the damage distribution, as any potential contact at the screw tip was removed. Without pre-drilling, contact between the bone and the tip of the screw could cause large differences between fully bonded and contact models in a pull-out scenario [204]. In contrast to FB and TED-M, TED-M+P models only predicted small amounts of damage outside the damage zone. This suggests that TED-M+P may overestimate damage within the damage zone while underestimating it outside. This error could be caused by the simple geometric representation of the cylindrical pre-damage zone with sharp boundaries, and should be further evaluated by comparison to experimentally measured pre-damage distributions. However, experimental methods for accurate measurement of pre-damage are not yet available and novel methods must be developed in order to validate µFE models at this level of detail. To guide researchers conducting similar studies, it is suggested to first perform a material parameter identification to establish these parameters as fixed. Subsequently, investigations into pre-damage formation caused by pre-drilling and screw insertion should be carried out. Using µCT scanning before and after screw insertion, the radial thickness of the pre-damage zone can be estimated [139]. The pre-damage value may be estimated using digital volume correlation,

which provides detailed 3D displacement and strain measurements, helping to detect deformations beyond the yield limit [206–209]. Additionally, staining techniques can highlight crack formation, enabling to assess the extent of damage [210,211]. Furthermore, extensive calibration studies involving multiple loading cases, specimens, and screws could be conducted to back-calculate the pre-damage parameters [120].

The study has several limitations. To begin with, the elastic modulus was taken from literature and was not experimentally determined for the used specimens. Furthermore, the applied nonlinear material properties were based on human bones and only adapted to porcine bones [24]. As the pre-damage parameters as well as the maximum force predictions depend on the selected material properties, this study cannot provide optimal parameters for future studies, but can only show the effect and ambiguity of the pre-damage parameters. Additionally, the study outcomes were restricted to pre-drilled bone samples. The drilling process leads to reduced strength and stability of the bone-screw construct [67] and leaves bone debris in the pilot-holes, which might be interpreted as intact bone in the µFE models. Furthermore, all results were limited to a single loading case, a single screw with one insertion depth, and the nonlinear material model of Stipsitz et al. [24], developed for efficient µFE simulations.

In conclusion, screw pull-out forces predicted by computationally efficient, materially nonlinear µFE are highly correlated with experimental measurements, even with a fully bonded interface and without considering pre-damage. However, to obtain quantitatively accurate results, careful orchestration of contact modeling, material properties and pre-damage parameters is required. The selection of these parameters is ambiguous and experimental assessment of pre-damage distributions is necessary to further refine and validate the µFE models. µCT scanning before and after screw insertion could be valuable in providing more accurate pre-damage distributions while methods like digital volume correlation and staining may help to estimate the pre-damage value. Until such experimental data become available, optimal parameters of a simplified pre-damage model must be identified as proposed in this study using comparison to experimental results.

Data availability statement

The raw data supporting the conclusions of this article will be made available by the authors, without undue reservation.

Ethics statement

Ethical approval was not required for the study involving animals in accordance with the local legislation and institutional requirements because the study only included the experimental data of a previous study from Silva-Henao et al. [78]. Ethical approval was not necessary as the used porcine bone samples were extracted from leftovers of a local abattoir.

Author contributions

PS: Data curation, Formal Analysis, Investigation, Methodology, Project administration, Visualization, Writing–original draft.
JS-H: Data curation, Investigation, Writing–review and editing.
VF: Data curation, Investigation, Writing–review and editing.
AR: Methodology, Supervision, Writing–review and editing.
DP: Methodology, Resources, Supervision, Writing–review and editing.
AS: Conceptualization, Methodology, Supervision, Writing–review and editing.

Funding

Conflict of interest

The authors declare that the research was conducted in the absence of any commercial or financial relationships that could be construed as a potential conflict of interest.

Generative AI statement

The author(s) declare that Generative AI was used in the creation of this manuscript. During the preparation of this work the authors used ChatGPT (GPT-4 Turbo) in order to improve readability and language. After using this tool, the authors reviewed and edited the content as needed and take full responsibility for the content of the publication.

Publisher's note

All claims expressed in this article are solely those of the authors and do not necessarily represent those of their affiliated organizations, or those of the publisher, the editors and the reviewers. Any product that may be evaluated in this article, or claim that may be made by its manufacturer, is not guaranteed or endorsed by the publisher.

Supplementary material

The Supplementary Material for this article can be found online at: https://www.frontiersin.org/articles/10.3389/fbioe.2025.1524235/full#supplementary-material

List of Figures

List of Tables

Image Credits

Bibliography

[1] C.M. Court-Brown, B. Caesar, Epidemiology of adult fractures: A review, Injury 37 (2006) 691–697. https://doi.org/10.1016/j.injury.2006.04.130.

[2] S. Polinder, J. Haagsma, M. Panneman, A. Scholten, M. Brugmans, E. Van Beeck, The economic burden of injury: Health care and productivity costs of injuries in the Netherlands, Accid Anal Prev 93 (2016) 92–100. https://doi.org/10.1016/j.aap.2016.04.003.

[3] A.-M. Wu, C. Bisignano, S.L. James, G.G. Abady, A. Abedi, E. Abu-Gharbieh, R.K. Alhassan, V. Alipour, J. Arabloo, M. Asaad, W.N. Asmare, A.F. Awedew, M. Banach, S.K. Banerjee, A. Bijani, T.T.M. Birhanu, S.R. Bolla, L.A. Cámera, J.-C. Chang, D.Y. Cho, M.T. Chung, R.A.S. Couto, X. Dai, L. Dandona, R. Dandona, F. Farzadfar, I. Filip, F. Fischer, A.A. Fomenkov, T.K. Gill, B. Gupta, J.A. Haagsma, A. Haj-Mirzaian, S. Hamidi, S.I. Hay, I.M. Ilic, M.D. Ilic, R.Q. Ivers, M. Jürisson, R. Kalhor, T. Kanchan, T. Kavetskyy, R. Khalilov, E.A. Khan, M. Khan, C.J. Kneib, V. Krishnamoorthy, G.A. Kumar, N. Kumar, R. Lalloo, S. Lasrado, S.S. Lim, Z. Liu, A. Manafi, N. Manafi, R.G. Menezes, T.J. Meretoja, B. Miazgowski, T.R. Miller, Y. Mohammad, A. Mohammadian-Hafshejani, A.H. Mokdad, C.J.L. Murray, M. Naderi, M.D. Naimzada, V.C. Nayak, C.T. Nguyen, R. Nikbakhsh, A.T. Olagunju, N. Otstavnov, S.S. Otstavnov, J.R. Padubidri, J. Pereira, H.Q. Pham, M. Pinheiro, S. Polinder, H. Pourchamani, N. Rabiee, A. Radfar, M.H.U. Rahman, D.L. Rawaf, S. Rawaf, M.R. Saeb, A.M. Samy, L. Sanchez Riera, D.C. Schwebel, S. Shahabi, M.A. Shaikh, A. Soheili, R. Tabarés-Seisdedos, M.R. Tovani-Palone, B.X. Tran, R.S. Travillian, P.R. Valdez, T.J. Vasankari, D.Z. Velazquez, N. Venketasubramanian, G.T. Vu, Z.-J. Zhang, T. Vos, Global, regional, and national burden of bone fractures in 204 countries and territories, 1990–2019: a systematic analysis from the Global Burden of Disease Study 2019, Lancet Healthy Longev 2 (2021) e580–e592. https://doi.org/10.1016/S2666-7568(21)00172-0.

[4] E. Hernlund, A. Svedbom, M. Ivergård, J. Compston, C. Cooper, J. Stenmark, E. V. McCloskey, B. Jönsson, J.A. Kanis, Osteoporosis in the European Union: medical management, epidemiology and economic burden, Arch Osteoporos 8 (2013) 136. https://doi.org/10.1007/s11657-013-0136-1.

[5] W. Jin, P.K. Chu, Orthopedic Implants, in: R. Narayan (Ed.), Encyclopedia of Biomedical Engineering, Elsevier, 2019: pp. 425–439. https://doi.org/10.1016/B978-0-12-801238-3.10999-7.

[6] T. Kim, C.W. See, X. Li, D. Zhu, Orthopedic implants and devices for bone fractures and defects: Past, present and perspective, Engineered Regeneration 1 (2020) 6–18. https://doi.org/10.1016/j.engreg.2020.05.003.

[7] C. Sommer, R. Babst, M. Müller, B. Hanson, Locking Compression Plate Loosening and Plate Breakage, J Orthop Trauma 18 (2004) 571–577. https://doi.org/10.1097/00005131-200409000-00016.

[8] T.-L. Foo, A.W. Gan, T. Soh, W.Y. Chew, Mechanical Failure of the Distal Radius Volar Locking Plate, Journal of Orthopaedic Surgery 21 (2013) 332–336. https://doi.org/10.1177/230949901302100314.

[9] A. Bigham-Sadegh, A. Oryan, Basic concepts regarding fracture healing and the current options and future directions in managing bone fractures, Int Wound J 12 (2015) 238–247. https://doi.org/10.1111/iwj.12231.

[10] F. Bayata, C. Yildiz, The effects of design parameters on mechanical failure of Ti-6Al-

4V implants using finite element analysis, Eng Fail Anal 110 (2020) 104445. https://doi.org/10.1016/j.engfailanal.2020.104445.

[11] W. Aljuhani, Y. Sayyad, Orthopedic Research Funding: Assessing the Relationship between Investments and Breakthroughs., Orthop Rev (Pavia) 16 (2024). https://doi.org/10.52965/001c.120368.

[12] G.S. Lewis, D. Mischler, H. Wee, J.S. Reid, P. Varga, Finite Element Analysis of Fracture Fixation, Curr Osteoporos Rep 19 (2021) 403–416. https://doi.org/10.1007/s11914-021-00690-y.

[13] M. Taylor, P.J. Prendergast, Four decades of finite element analysis of orthopaedic devices: Where are we now and what are the opportunities?, J Biomech 48 (2015) 767–778. https://doi.org/10.1016/j.jbiomech.2014.12.019.

[14] S.K. Parashar, J.K. Sharma, A review on application of finite element modelling in bone biomechanics, Perspect Sci (Neth) 8 (2016) 696–698. https://doi.org/10.1016/j.pisc.2016.06.062.

[15] K.-J. Bathe, Finite Element Procedures, Prentice Hall, 2006.

[16] G.H. van Lenthe, R. Müller, Prediction of failure load using micro-finite element analysis models: Toward in vivo strength assessment, Drug Discov Today Technol 3 (2006) 221–229. https://doi.org/10.1016/j.ddtec.2006.06.001.

[17] B. van Rietbergen, Micro-FE Analyses of Bone: State of the Art, Adv Exp Med Biol 496 (2001) 21–30. https://doi.org/10.1007/978-1-4615-0651-5_3.

[18] B. van Rietbergen, K. Ito, A survey of micro-finite element analysis for clinical assessment of bone strength: The first decade, J Biomech 48 (2015) 832–841. https://doi.org/10.1016/j.jbiomech.2014.12.024.

[19] P. Marcián, L. Borák, T. Zikmund, L. Horáčková, J. Kaiser, M. Joukal, J. Wolff, On the limits of finite element models created from (micro)CT datasets and used in studies of bone-implant-related biomechanical problems, J Mech Behav Biomed Mater 117 (2021). https://doi.org/10.1016/j.jmbbm.2021.104393.

[20] A.J. Wirth, R. Müller, G. Harry van Lenthe, The discrete nature of trabecular bone microarchitecture affects implant stability, J Biomech 45 (2012) 1060–1067. https://doi.org/10.1016/j.jbiomech.2011.12.024.

[21] A.J. Wirth, J. Goldhahn, C. Flaig, P. Arbenz, R. Müller, G.H. Van Lenthe, Implant stability is affected by local bone microstructural quality, Bone 49 (2011) 473–478. https://doi.org/10.1016/j.bone.2011.05.001.

[22] S. Nawathe, H. Akhlaghpour, M.L. Bouxsein, T.M. Keaveny, Microstructural Failure Mechanisms in the Human Proximal Femur for Sideways Fall Loading, Journal of Bone and Mineral Research 29 (2014) 507–515. https://doi.org/10.1002/jbmr.2033.

[23] R.L. Taylor, FEAP - Finite Element Analysis Program, (2020). http://projects.ce.berkeley.edu/feap/manual_86.pdf (accessed November 8, 2024).

[24] M. Stipsitz, P.K. Zysset, D.H. Pahr, Efficient materially nonlinear μFE solver for simulations of trabecular bone failure, Biomech Model Mechanobiol 19 (2020) 861–874. https://doi.org/10.1007/s10237-019-01254-x.

[25] C. Flaig, P. Arbenz, A highly scalable matrix-free multigrid solver for μFE analysis based on a pointer-less octree, Large-Scale Scientific Computing (2012) 498–506.

[26] M. Stipsitz, Development of a nonlinear micro finite element framework for image-based simulations in bone biomechanics, Doctoral Thesis, TU Wien, 2020. https://permalink.obvsg.at/AC15606542 (accessed March 27, 2025).

[27] J.-Y. Rho, L. Kuhn-Spearing, P. Zioupos, Mechanical properties and the hierarchical structure of bone, Med Eng Phys 20 (1998) 92–102. https://doi.org/10.1016/S1350-4533(98)00007-1.

[28] R. Ben Kahla, A. Barkaoui, Bone multiscale mechanics, in: Bone Remodeling Process: Mechanics, Biology, and Numerical Modeling, Academic Press, 2021: pp. 1–47.

https://doi.org/10.1016/b978-0-323-88467-9.00005-9.

[29] F.A. Sabet, A.R. Najafi, E. Hamed, I. Jasiuk, Modelling of bone fracture and strength at different length scales: A review, Interface Focus 6 (2016) 20–30. https://doi.org/10.1098/rsfs.2015.0055.

[30] J. Wolff, The Law of Bone Remodelling, Springer Berlin Heidelberg, 1986. https://doi.org/10.1007/978-3-642-71031-5.

[31] K.T. Patton, G.A. Thibodeau, Anthony's textbook of anatomy & physiology, 21st ed., Elsevier Health Sciences, St. Louis, 2019.

[32] B. Abernethy, V. Kippers, S.J. Hanrahan, M.G. Pandy, A.M. McManus, L. Mackinnon, Biophysical Foundations of Human Movement, 3rd ed., Human Kinetics, 2013.

[33] J. Fan, K. Abedi-Dorcheh, A. Sadat Vaziri, F. Kazemi-Aghdam, S. Rafieyan, M. Sohrabinejad, M. Ghorbani, F. Rastegar Adib, Z. Ghasemi, K. Klavins, V. Jahed, A Review of Recent Advances in Natural Polymer-Based Scaffolds for Musculoskeletal Tissue Engineering, Polymers (Basel) 14 (2022) 2097. https://doi.org/10.3390/polym14102097.

[34] R. Oftadeh, M. Perez-Viloria, J.C. Villa-Camacho, A. Vaziri, A. Nazarian, Biomechanics and Mechanobiology of Trabecular Bone: A Review, J Biomech Eng 137 (2015). https://doi.org/10.1115/1.4029176.

[35] J.S. Nyman, M. Granke, R.C. Singleton, G.M. Pharr, Tissue-Level Mechanical Properties of Bone Contributing to Fracture Risk, Curr Osteoporos Rep 14 (2016) 138–150. https://doi.org/10.1007/s11914-016-0314-3.

[36] H.H. Bayraktar, E.F. Morgan, G.L. Niebur, G.E. Morris, E.K. Wong, T.M. Keaveny, Comparison of the elastic and yield properties of human femoral trabecular and cortical bone tissue, J Biomech 37 (2004) 27–35. https://doi.org/10.1016/S0021-9290(03)00257-4.

[37] R. Jungmann, M.E. Szabo, G. Schitter, R. Yue-Sing Tang, D. Vashishth, P.K. Hansma, P.J. Thurner, Local strain and damage mapping in single trabeculae during three-point bending tests, J Mech Behav Biomed Mater 4 (2011) 523–534. https://doi.org/10.1016/j.jmbbm.2010.12.009.

[38] R. Carretta, S. Lorenzetti, R. Müller, Towards patient-specific material modeling of trabecular bonepost-yield behavior, Int J Numer Method Biomed Eng 29 (2013) 250–272. https://doi.org/10.1002/cnm.2516.

[39] D. Vashishth, J.C. Behiri, W. Bonfield, Crack growth resistance in cortical bone: Concept of microcrack toughening, J Biomech 30 (1997) 763–769. https://doi.org/10.1016/S0021-9290(97)00029-8.

[40] E.F. Wachtel, T.M. Keaveny, Dependence of trabecular damage on mechanical strain, Journal of Orthopaedic Research 15 (1997) 781–787. https://doi.org/10.1002/jor.1100150522.

[41] E.A. Zimmermann, E. Schaible, H. Bale, H.D. Barth, S.Y. Tang, P. Reichert, B. Busse, T. Alliston, J.W. Ager, R.O. Ritchie, Age-related changes in the plasticity and toughness of human cortical bone at multiple length scales, Proceedings of the National Academy of Sciences 108 (2011) 14416–14421. https://doi.org/10.1073/pnas.1107966108.

[42] D. Casari, J. Michler, P. Zysset, J. Schwiedrzik, Microtensile properties and failure mechanisms of cortical bone at the lamellar level, Acta Biomater 120 (2021) 135–145. https://doi.org/10.1016/j.actbio.2020.04.030.

[43] E.F. Morgan, T.M. Keaveny, Dependence of yield strain of human trabecular bone on anatomic site, J Biomech 34 (2001) 569–577. https://doi.org/10.1016/S0021-9290(01)00011-2.

[44] D.T. Reilly, A.H. Burstein, The elastic and ultimate properties of compact bone tissue, J Biomech 8 (1975) 393–405. https://doi.org/10.1016/0021-9290(75)90075-5.

[45] H. Alsop, the Executive Committee of the Association of Orthopaedic Chartered

Physiotherapists, An introduction to fractures, in: S.B. Porter (Ed.), Tidy's Physiotherapy, 15th ed., Churchill Livingstone, 2013.

[46] S.G. Salvo, Mosby's Pathology for Massage Therapists, 4th ed., Elsevier, St. Louis, 2018.

[47] L.N. McKinnis, Fundamentals of musculuskelatal imaging, 4th ed., F.A. Davis Company, Philadelphia, 2014.

[48] D.L. Hamblen, H.R.W. Simpson, Adams's Outline of Fractures Including Joint Injuries, 12th ed., Churchill Livingstone Elsevier, Philadelphia, 2007.

[49] A.M. Phillips, Overview of the fracture healing cascade, Injury 36 (2005) S5–S7. https://doi.org/10.1016/j.injury.2005.07.027.

[50] E. Ercin, M. Hurmeydan, M. Karahan, Bone Anatomy and the Biologic Healing Process of a Fracture, in: A. Gobbi, J. Espregueira-Mendes, J.G. Lane, M. Karahan (Eds.), Bio-Orthopaedics: A New Approach, Springer Berlin Heidelberg, 2017: pp. 437–449. https://doi.org/10.1007/978-3-662-54181-4.

[51] H. Elhawary, A. Baradaran, J. Abi-Rafeh, J. Vorstenbosch, L. Xu, J.I. Efanov, Bone Healing and Inflammation: Principles of Fracture and Repair, Semin Plast Surg 35 (2021) 198–203. https://doi.org/10.1055/s-0041-1732334.

[52] J.R. Sheen, A. Mabrouk, V. V. Garla, Fracture Healing Overview, in: StatPearls [Internet], StatPearls Publishing, Treasure Island, 2023.

[53] T.P. Rüedi, R.E. Buckley, C.G. Moran, AO Principles of Fracture Management, 2nd ed., AO Publishing, Davos Platz, 2007.

[54] A.S. Boyd, H.J. Benjamin, C. Asplund, Splints and Casts: Indications and Methods, 80 (2009) 491–499. www.aafp.org/afp.

[55] A.J. Thakur, Locking Plates - Concepts and Applications, 2nd ed., Wolters Kluwer, New Delhi, 2018.

[56] M.S. Ghiasi, J. Chen, A. Vaziri, E.K. Rodriguez, A. Nazarian, Bone fracture healing in mechanobiological modeling: A review of principles and methods, Bone Rep 6 (2017) 87–100. https://doi.org/10.1016/j.bonr.2017.03.002.

[57] K.A. Egol, E.N. Kubiak, E. Fulkerson, F.J. Kummer, K.J. Koval, Biomechanics of locked plates and screws., J Orthop Trauma 18 (2004) 488–93. https://doi.org/10.1097/00005131-200409000-00003.

[58] P. Augat, C. von Rüden, Evolution of fracture treatment with bone plates, Injury 49 (2018) S2–S7. https://doi.org/10.1016/S0020-1383(18)30294-8.

[59] C.-L. Tai, P.-Y. Lee, P.-H. Hsieh, Preliminary Biomechanical Study of Different Acetabular Reinforcement Devices for Acetabular Reconstruction, PLoS One 10 (2015) e0121588. https://doi.org/10.1371/journal.pone.0121588.

[60] C.M. Bellini, M.T. Raimondi, R. Accetta, G. V. Mineo, Locked Plating: Biomechanics and Biology, Techniques in Orthopaedics 22 (2007) 167–172. https://doi.org/10.1097/BTO.0b013e31814a6337.

[61] S.L.E. Tan, Z.J. Balogh, Indications and limitations of locked plating, Injury 40 (2009) 683–691. https://doi.org/10.1016/j.injury.2009.01.003.

[62] F. Parmaksizoglu, S. Kilic, O. Cetin, A novel model of locking plate and locking spongious screw: a biomechanical in vitro comparison study with classical locking plate, J Orthop Surg Res 19 (2024) 237. https://doi.org/10.1186/s13018-024-04700-4.

[63] A. Synek, Y. Chevalier, S.F. Baumbach, D.H. Pahr, The influence of bone density and anisotropy in finite element models of distal radius fracture osteosynthesis: Evaluations and comparison to experiments, J Biomech 48 (2015) 4116–4123. https://doi.org/10.1016/j.jbiomech.2015.10.012.

[64] A.J. Thakur, The elements of fracture fixation, 2nd ed., Elsevier, New Delhi, 2007.

[65] R.A. Eriksson, R. Adell, Temperatures during drilling for the placement of implants using the osseointegration technique, Journal of Oral and Maxillofacial Surgery 44

(1986) 4–7. https://doi.org/10.1016/0278-2391(86)90006-6.

[66] G. Augustin, T. Zigman, S. Davila, T. Udilljak, T. Staroveski, D. Brezak, S. Babic, Cortical bone drilling and thermal osteonecrosis, Clinical Biomechanics 27 (2012) 313–325. https://doi.org/10.1016/j.clinbiomech.2011.10.010.

[67] R.K. Pandey, S.S. Panda, Drilling of bone: A comprehensive review., J Clin Orthop Trauma 4 (2013) 15–30. https://doi.org/10.1016/j.jcot.2013.01.002.

[68] K. Alam, Experimental and numerical investigation of cracking behavior of cortical bone in cutting, Technology and Health Care 22 (2014) 741–750. https://doi.org/10.3233/THC-140848.

[69] A.L. Johnson, J.E. Houlton, R. Vannini, Implants: description and application, in: A.L. Johnson, J.E. Houlton, R. Vannini (Eds.), AO Principles of Fracture Management in the Dog and Cat, AO Publishing, Davos Platz, 2007: pp. 27–69.

[70] W. Heidemann, H. Terheyden, K.L. Gerlach, Analysis of the osseous/metal interface of drill free screws and self-tapping screws, J Craniomaxillofac Surg 29 (2001) 69–74. https://doi.org/10.1054/jcms.2000.0179.

[71] W. Heidemann, K.L. Gerlach, K.-H. Gröbel, H.-G. Köllner, Drill Free Screws: a new form of osteosynthesis screw, Journal of Cranio-Maxillofacial Surgery 26 (1998) 163–168. https://doi.org/10.1016/S1010-5182(98)80007-3.

[72] M. Tepedino, F. Masedu, C. Chimenti, Comparative evaluation of insertion torque and mechanical stability for self-tapping and self-drilling orthodontic miniscrews – an in vitro study, Head Face Med 13 (2017) 10. https://doi.org/10.1186/s13005-017-0143-3.

[73] P. Silva, R.C. Rosa, A.C. Shimano, F.J. Albuquerque de Paula, J.B. Volpon, H.L. Aparecido Defino, BIOMECHANICAL EVALUATION OF THE INFLUENCE OF CERVICAL SCREWS TAPPING AND DESIGN, Revista Brasileira de Ortopedia (English Edition) 44 (2009) 415–419. https://doi.org/10.1016/S2255-4971(15)30272-X.

[74] J.U. Umoh, A. V Sampaio, I. Welch, V. Pitelka, H.A. Goldberg, T.M. Underhill, D.W. Holdsworth, In vivo micro-CT analysis of bone remodeling in a rat calvarial defect model, Phys Med Biol 54 (2009) 2147–2161. https://doi.org/10.1088/0031-9155/54/7/020.

[75] E. Gautier, S.M. Perren, J. Cordey, Strain distribution in plated and unplated sheep tibia an in vivo experiment, Injury 31 (2000) 37–93. https://doi.org/10.1016/S0020-1383(00)80030-3.

[76] R. Depprich, H. Zipprich, M. Ommerborn, C. Naujoks, H.-P. Wiesmann, S. Kiattavorncharoen, H.-C. Lauer, U. Meyer, N.R. Kübler, J. Handschel, Osseointegration of zirconia implants compared with titanium: an in vivo study, Head Face Med 4 (2008) 30. https://doi.org/10.1186/1746-160X-4-30.

[77] S.J. Kaplan, W.C. Hayes, J.L. Stone, G.S. Beaupré, Tensile strength of bovine trabecular bone, J Biomech 18 (1985) 723–727. https://doi.org/10.1016/0021-9290(85)90027-2.

[78] J.D. Silva-Henao, S. Schober, D.H. Pahr, A.G. Reisinger, Critical loss of primary implant stability in osteosynthesis locking screws under cyclic overloading, Med Eng Phys 126 (2024) 104143. https://doi.org/10.1016/j.medengphy.2024.104143.

[79] F. Linde, I. Hvid, Stiffness behaviour of trabecular bone specimens, J Biomech 20 (1987) 83–89. https://doi.org/10.1016/0021-9290(87)90270-3.

[80] B. Nowak, Experimental study on the loosening of pedicle screws implanted to synthetic bone vertebra models and under non-pull-out mechanical loads, J Mech Behav Biomed Mater 98 (2019) 200–204. https://doi.org/10.1016/j.jmbbm.2019.06.013.

[81] Y.H. An, R.A. Draughn, Mechanical Properties and Testing Methods of Bone, in: R.J. Freidman, Y.H. An (Eds.), Animal Models in Orthopaedic Research, CRC Press, Boca Raton, 1999.

[82] E. Dall'Ara, V.S. Cheong, Bone Biomechanics, in: B. Innocenti, F. Galbusera (Eds.), Human Orthopaedic Biomechanics. Fundamentals, Devices and Applications, Academic

Press, 2022.

[83]   L. La Barbera, T. Villa, B. Innocenti, F. Galbusera, Experimental orthopedic biomechanics, in: B. Innocenti, F. Galbusera (Eds.), Human Orthopedic Biomechanics. Fundamentals, Devices and Applications, Academic Press, 2022.

[84]   G.A. Battraw, V. Miera, P.L. Anderson, J.A. Szivek, Bilateral symmetry of biomechanical properties in rat femora, J Biomed Mater Res 32 (1996) 285–288. https://doi.org/10.1002/(SICI)1097-4636(199610)32:2<285::AID-JBM19>3.0.CO;2-I.

[85]   A.A. Biewener, In vivo measurement of bone strain and tendon force, in: Biomechanics — Structures and Systems, Oxford University Press, 1992: pp. 123–148. https://doi.org/10.1093/oso/9780199632688.003.0006.

[86]   W.E. Caler, D.R. Carter, W.H. Harris, Techniques for implementing an in vivo bone strain gage system, J Biomech 14 (1981) 503–507. https://doi.org/10.1016/0021-9290(81)90164-0.

[87]   A. Parsa, N. Ibrahim, B. Hassan, P. van der Stelt, D. Wismeijer, Bone quality evaluation at dental implant site using multislice CT, micro-CT, and cone beam CT, Clin Oral Implants Res 26 (2015) e1–e7. https://doi.org/10.1111/clr.12315.

[88]   X. Wang, D.B. Masse, H. Leng, K.P. Hess, R.D. Ross, R.K. Roeder, G.L. Niebur, Detection of trabecular bone microdamage by micro-computed tomography, J Biomech 40 (2007) 3397–3403. https://doi.org/10.1016/j.jbiomech.2007.05.009.

[89]   Y. Lu, Computational modelling of bone microstructure, in: Z. Jin, J. Li, Z. Chen (Eds.), Computational Modelling of Biomechanics and Biotribology in the Musculoskeletal System: Biomaterials and Tissues., 2nd ed., Woodhead Publishing, 2021.

[90]   K. Engelke, B. van Rietbergen, P. Zysset, FEA to Measure Bone Strength: A Review, Clin Rev Bone Miner Metab 14 (2016) 26–37. https://doi.org/10.1007/s12018-015-9201-1.

[91]   E. Verhulp, B. van Rietbergen, R. Huiskes, Comparison of micro-level and continuum-level voxel models of the proximal femur, J Biomech 39 (2006) 2951–2957. https://doi.org/10.1016/j.jbiomech.2005.10.027.

[92]   D.H. Pahr, E. Dall'Ara, P. Varga, P.K. Zysset, HR-pQCT-based homogenised finite element models provide quantitative predictions of experimental vertebral body stiffness and strength with the same accuracy as µFE models, Comput Methods Biomech Biomed Engin 15 (2012) 711–720. https://doi.org/10.1080/10255842.2011.556627.

[93]   E. Dall'Ara, D. Pahr, P. Varga, F. Kainberger, P. Zysset, QCT-based finite element models predict human vertebral strength in vitro significantly better than simulated DEXA, Osteoporosis International 23 (2012) 563–572. https://doi.org/10.1007/s00198-011-1568-3.

[94]   J. Alsayednoor, L. Metcalf, J. Rochester, E. Dall'Ara, E. McCloskey, D. Lacroix, Comparison of HR-pQCT- and microCT-based finite element models for the estimation of the mechanical properties of the calcaneus trabecular bone, Biomech Model Mechanobiol 17 (2018) 1715–1730. https://doi.org/10.1007/s10237-018-1051-6.

[95]   J.N. Reddy, An Introduction to Nonlinear Finite Element Analysis: With Applications to Heat Transfer, Fluid Mechanics, and Solid Mechanics, 2nd ed., Oxford University Press, Oxford, 2015.

[96]   P. Wriggers, Nichtlineare Finite-Element-Methoden, Springer Berlin Heidelberg, 2001. https://doi.org/10.1007/978-3-642-56865-7.

[97]   G. Ramamurty, Applied Finite Element Analysis, I.K. International Publishing House Pvt. Ltd., New Delhi, 2009.

[98]   W. Rust, Nichtlineare Finite-Elemente-Berechnungen: Kontakt, Kinematik, Material, 3rd ed., Springer Fachmedien Wiesbaden, 2016. https://doi.org/10.1007/978-3-658-13378-8.

[99]   T.J. Chung, Computational Fluid Dynamics, 2nd ed., Cambridge University Press, 2010.

[100] B. Van Rietbergen, H. Weinans, R. Huiskes, A. Odgaard, A new method to determine trabecular bone elastic properties and loading using micromechanical finite-element models, J Biomech 28 (1995) 69–81. https://doi.org/10.1016/0021-9290(95)80008-5.

[101] J. Ghaboussi, X.S. Wu, Numerical Methods in Computational Mechanics, CRC Press, Boca Raton, 2016.

[102] M. Okereke, S. Keates, Finite Element Applications: A Practical Guide to the FEM Process, Springer International Publishing, Cham, 2018. https://doi.org/10.1007/978-3-319-67125-3.

[103] A. Hivet, Z. El‑Alami, T. Larquemin, A. Shanwan, Analysis and modeling of forming process at the mesoscale, in: P. Wang, N. Hamila (Eds.), Advanced Structural Textural Composites Forming: Characterization, Modeling, and Simulation, Woodhead Publishing, 2024: pp. 278–291.

[104] F.J. Harewood, P.E. McHugh, Comparison of the implicit and explicit finite element methods using crystal plasticity, Comput Mater Sci 39 (2007) 481–494. https://doi.org/10.1016/j.commatsci.2006.08.002.

[105] Dassault Systems, Abaqus/CAE User's Guide, (2024).

[106] M.O. Heller, Finite element analysis in orthopedic biomechanics, in: B. Innocenti, F. Galbusera (Eds.), Human Orthopaedic Biomechanics: Fundamentals, Devices and Applications, Academic Press, 2022: pp. 637–658. https://doi.org/10.1016/B978-0-12-824481-4.00026-3.

[107] Y. Chen, E. Dall'Ara, E. Sales, K. Manda, R. Wallace, P. Pankaj, M. Viceconti, Micro-CT based finite element models of cancellous bone predict accurately displacement once the boundary condition is well replicated: A validation study, J Mech Behav Biomed Mater 65 (2017) 644–651. https://doi.org/10.1016/j.jmbbm.2016.09.014.

[108] J. Kabel, B. van Rietbergen, M. Dalstra, A. Odgaard, R. Huiskes, The role of an effective isotropic tissue modulus in the elastic properties of cancellous bone, J Biomech 32 (1999) 673–680. https://doi.org/10.1016/S0021-9290(99)00045-7.

[109] P. Frey, B. Sarter, M. Gautherie, Fully automatic mesh generation for 3-D domains based upon voxel sets, Int J Numer Methods Eng 37 (1994) 2735–2753. https://doi.org/10.1002/nme.1620371604.

[110] R. Müller, P. Rüegsegger, Three-dimensional finite element modelling of non-invasively assessed trabecular bone structures, Med Eng Phys 17 (1995) 126–133. https://doi.org/10.1016/1350-4533(95)91884-J.

[111] D. Ruffoni, G.H. Van Lenthe, Finite element analysis in bone research: A computational method relating structure to mechanical function, Comprehensive Biomaterials 3 (2011) 91–111. https://doi.org/10.1016/b978-0-12-803581-8.09798-8.

[112] T. Gross, D.H. Pahr, F. Peyrin, P.K. Zysset, Mineral heterogeneity has a minor influence on the apparent elastic properties of human cancellous bone: a SRµCT-based finite element study, Comput Methods Biomech Biomed Engin 15 (2012) 1137–1144. https://doi.org/10.1080/10255842.2011.581236.

[113] C.H. Turner, J. Rho, Y. Takano, T.Y. Tsui, G.M. Pharr, The elastic properties of trabecular and cortical bone tissues are similar: results from two microscopic measurement techniques, 1999. https://doi.org/10.1016/S0021-9290(98)00177-8.

[114] J.-Y. Rho, T.Y. Tsui, G.M. Pharr, Elastic properties of human cortical and trabecular lamellar bone measured by nanoindentation, Biomaterials 18 (1997) 1325–1330. https://doi.org/10.1016/S0142-9612(97)00073-2.

[115] Y. Chevalier, M. Matsuura, S. Krüger, C. Fleege, M. Rickert, M. Rauschmann, C. Schilling, Micro-CT and micro-FE analysis of pedicle screw fixation under different loading conditions, J Biomech 70 (2018) 204–211. https://doi.org/10.1016/j.jbiomech.2017.12.023.

[116] W. Pistoia, B. Van Rietbergen, E.-M. Lochmüller, C.A. Lill, F. Eckstein, P. Rüegsegger,

Estimation of Distal Radius Failure Load With Micro-Finite Element Analysis Models Based on Three-dimensional Peripheral Quantitative Computed Tomography Images, Bone 30 (2002) 842–848. https://doi.org/10.1016/S8756-3282(02)00736-6.

[117] A.J. Wirth, T.L. Mueller, W. Vereecken, C. Flaig, P. Arbenz, R. Müller, G.H. Van Lenthe, Mechanical competence of bone-implant systems can accurately be determined by image-based micro-finite element analyses, Archive of Applied Mechanics 80 (2010) 513–525. https://doi.org/10.1007/s00419-009-0387-x.

[118] D.H. Pahr, A.G. Reisinger, A Review on Recent Advances in the Constitutive Modeling of Bone Tissue, Curr Osteoporos Rep 18 (2020) 696–704. https://doi.org/10.1007/s11914-020-00631-1.

[119] M.C. Costa, G. Tozzi, L. Cristofolini, V. Danesi, M. Viceconti, E. Dall'Ara, Micro finite element models of the vertebral body: Validation of local displacement predictions, PLoS One 12 (2017) 1–18. https://doi.org/10.1371/journal.pone.0180151.

[120] J.A. Steiner, P. Christen, R. Affentranger, S.J. Ferguson, G.H. van Lenthe, A novel in silico method to quantify primary stability of screws in trabecular bone, Journal of Orthopaedic Research 35 (2017) 2415–2424. https://doi.org/10.1002/jor.23551.

[121] M. Ovesy, J.D. Silva-Henao, J.W.A. Fletcher, B. Gueorguiev, P.K. Zysset, P. Varga, Non-linear explicit micro-FE models accurately predict axial pull-out force of cortical screws in human tibial cortical bone, J Mech Behav Biomed Mater 126 (2022) 105002. https://doi.org/10.1016/j.jmbbm.2021.105002.

[122] V.C. Panagiotopoulou, M. Ovesy, B. Gueorguiev, R.G. Richards, P. Zysset, P. Varga, Experimental and numerical investigation of secondary screw perforation in the human proximal humerus, J Mech Behav Biomed Mater 116 (2021) 104344. https://doi.org/10.1016/j.jmbbm.2021.104344.

[123] M. Stipsitz, P.K. Zysset, D.H. Pahr, Prediction of the Inelastic Behaviour of Radius Segments: Damage-based Nonlinear Micro Finite Element Simulation vs Pistoia Criterion, J Biomech 116 (2021) 110205. https://doi.org/10.1016/j.jbiomech.2020.110205.

[124] S. Oliviero, M. Giorgi, E. Dall'Ara, Validation of finite element models of the mouse tibia using digital volume correlation, J Mech Behav Biomed Mater 86 (2018) 172–184. https://doi.org/10.1016/j.jmbbm.2018.06.022.

[125] S. Oliviero, R. Owen, G.C. Reilly, I. Bellantuono, E. Dall'Ara, Optimization of the failure criterion in micro-Finite Element models of the mouse tibia for the non-invasive prediction of its failure load in preclinical applications, J Mech Behav Biomed Mater 113 (2021) 104190. https://doi.org/10.1016/j.jmbbm.2020.104190.

[126] F.A. Sabet, O. Jin, S. Koric, I. Jasiuk, Nonlinear micro-CT based FE modeling of trabecular bone—Sensitivity of apparent response to tissue constitutive law and bone volume fraction, Int J Numer Method Biomed Eng 34 (2018) e2941. https://doi.org/10.1002/cnm.2941.

[127] B. Werner, M. Ovesy, P.K. Zysset, An explicit micro-FE approach to investigate the post-yield behaviour of trabecular bone under large deformations, Int J Numer Method Biomed Eng 35 (2019) e3188. https://doi.org/10.1002/cnm.3188.

[128] J. Schwiedrzik, T. Gross, M. Bina, M. Pretterklieber, P. Zysset, D. Pahr, Experimental validation of a nonlinear µFE model based on cohesive-frictional plasticity for trabecular bone, Int J Numer Method Biomed Eng 32 (2016) e02739. https://doi.org/10.1002/cnm.2739.

[129] G.L. Niebur, M.J. Feldstein, J.C. Yuen, T.J. Chen, T.M. Keaveny, High-resolution finite element models with tissue strength asymmetry accurately predict failure of trabecular bone, J Biomech 33 (2000) 1575–1583. https://doi.org/10.1016/S0021-9290(00)00149-4.

[130] A.P. Baumann, X. Shi, R.K. Roeder, G.L. Niebur, The sensitivity of nonlinear

computational models of trabecular bone to tissue level constitutive model, Comput Methods Biomech Biomed Engin 19 (2016) 465–73. https://doi.org/10.1080/10255842.2015.1041022.

[131] R. Hambli, Micro-CT finite element model and experimental validation of trabecular bone damage and fracture, Bone 56 (2013) 363–374. https://doi.org/10.1016/j.bone.2013.06.028.

[132] N.M. Harrison, P. McDonnell, L. Mullins, N. Wilson, D. O'Mahoney, P.E. McHugh, Failure modelling of trabecular bone using a non-linear combined damage and fracture voxel finite element approach, Biomech Model Mechanobiol 12 (2013) 225–241. https://doi.org/10.1007/s10237-012-0394-7.

[133] J.D. Thompson, J.B. Benjamin, J.A. Szivek, Pullout strengths of cannulated and noncannulated cancellous bone screws, Clin Orthop Relat Res (1997) 241–9. https://api.semanticscholar.org/CorpusID:22952101 (accessed March 27, 2025).

[134] T. Pore, S.G. Thorat, A.A. Nema, Review of contact modelling in nonlinear finite element analysis, Mater Today Proc 47 (2021) 2436–2440. https://doi.org/10.1016/j.matpr.2021.04.504.

[135] P. Wriggers, Finite element algorithms for contact problems, Archives of Computational Methods in Engineering 2 (1995) 1–49. https://doi.org/10.1007/BF02736195.

[136] A. Soprano, F. Caputo, Simulating the Response of Structures to Impulse Loadings, in: L. Angermann (Ed.), Numerical Simulations: Applications, Examples and Theory, InTech, Rijeka, 2011: pp. 281–311.

[137] A. Torcasio, X. Zhang, H. Van Oosterwyck, J. Duyck, G.H. Van Lenthe, Use of micro-CT-based finite element analysis to accurately quantify peri-implant bone strains: A validation in rat tibiae, Biomech Model Mechanobiol 11 (2012) 743–750. https://doi.org/10.1007/s10237-011-0347-6.

[138] N.K. Lee, S.H. Baek, Effects of the diameter and shape of orthodontic mini-implants on microdamage to the cortical bone, American Journal of Orthodontics and Dentofacial Orthopedics 138 (2010) 8.e1-8.e8. https://doi.org/10.1016/j.ajodo.2010.02.019.

[139] J.A. Steiner, S.J. Ferguson, G.H. van Lenthe, Screw insertion in trabecular bone causes peri-implant bone damage, Med Eng Phys 38 (2016) 417–422. https://doi.org/10.1016/j.medengphy.2016.01.006.

[140] L. Wang, J. Shao, T. Ye, L. Deng, S. Qiu, Three-dimensional morphology of microdamage in peri-screw bone: A scanning electron microscopy of methylmethacrylate cast replica, Microscopy and Microanalysis 18 (2012) 1106–1111. https://doi.org/10.1017/S1431927612001286.

[141] A. Warreth, I. Polyzois, C.T. Lee, N. Claffey, Generation of microdamage around endosseous implants, Clin Oral Implants Res 20 (2009) 1300–1306. https://doi.org/10.1111/j.1600-0501.2009.01808.x.

[142] P. Methawit, M. Uezono, T. Ogasawara, P. Techalertpaisarn, K. Moriyama, Cortical bone microdamage affects primary stability of orthodontic miniscrew, J World Fed Orthod 12 (2023) 229–236. https://doi.org/10.1016/j.ejwf.2023.06.002.

[143] S. Yadav, M. Upadhyay, S. Liu, E. Roberts, W.P. Neace, R. Nanda, Microdamage of the cortical bone during mini-implant insertion with self-drilling and self-tapping techniques: A randomized controlled trial, American Journal of Orthodontics and Dentofacial Orthopedics 141 (2012) 538–546. https://doi.org/10.1016/j.ajodo.2011.12.016.

[144] M. V Nguyen, J. Codrington, L. Fletcher, C.W. Dreyer, W.J. Sampson, The influence of miniscrew insertion torque, Eur J Orthod 40 (2018) 37–44. https://doi.org/10.1093/ejo/cjx026.

[145] M. Ovesy, M. Indermaur, P.K. Zysset, Prediction of insertion torque and stiffness of a dental implant in bovine trabecular bone using explicit micro-finite element analysis, J

Mech Behav Biomed Mater 98 (2019) 301–310. https://doi.org/10.1016/j.jmbbm.2019.06.024.

[146] Y. Zhou, B. Helgason, S.J. Ferguson, C. Persson, Validated, high-resolution, non-linear, explicit finite element models for simulating screw - bone interaction, Biomedical Engineering Advances 7 (2024) 100115. https://doi.org/10.1016/j.bea.2024.100115.

[147] Z. Bi, Finite Element Analysis Applications: A systematic and Practical Approach, Academic Press, 2018. https://doi.org/10.1016/C2016-0-00054-2.

[148] J.H. Kim, C.S. Lee, S.J. Kim, High-performance domainwise parallel direct solver for large-scale structural analysis, AIAA Journal 43 (2005) 662–670. https://doi.org/10.2514/1.11171.

[149] G.R. Liu, S.S. Quek, The Finite Element Method: A Practical Course, Butterworth-Heinemann, 2003.

[150] L. Börgesson, ABAQUS, Developments in Geotechnical Engineering 79 (1996) 565–570. https://doi.org/10.1016/S0165-1250(96)80047-2.

[151] D. Jodlbauer, U. Langer, T. Wick, Parallel Matrix-Free Higher-Order Finite Element Solvers for Phase-Field Fracture Problems, Mathematical and Computational Applications 25 (2020) 40. https://doi.org/10.3390/mca25030040.

[152] P. Wili, G. Maquer, J. Panyasantisuk, P.K. Zysset, Estimation of the effective yield properties of human trabecular bone using nonlinear micro-finite element analyses., Biomech Model Mechanobiol 16 (2017) 1925–1936. https://doi.org/10.1007/s10237-017-0928-0.

[153] J. Panyasantisuk, D.H. Pahr, P.K. Zysset, Effect of boundary conditions on yield properties of human femoral trabecular bone, Biomech Model Mechanobiol 15 (2016) 1043–1053. https://doi.org/10.1007/s10237-015-0741-6.

[154] B. Voumard, P. Stefanek, M. Pretterklieber, D. Pahr, P. Zysset, Influence of aging on mechanical properties of the femoral neck using an inverse method, Bone Rep 17 (2022) 101638. https://doi.org/10.1016/j.bonr.2022.101638.

[155] A. Synek, L. Ortner, D.H. Pahr, Accuracy of osseointegrated screw-bone construct stiffness and peri-implant loading predicted by homogenized FE models relative to micro-FE models, J Mech Behav Biomed Mater 140 (2023). https://doi.org/10.1016/j.jmbbm.2023.105740.

[156] M. Münch, Eine Schnittstelle zwischen den Programmen FEAP (Finite Element Analysis Program) und INGA (INteraktive Graphische Analyse), in: Computer, Software Und Vernetzungen Für Die Lehre, Dette, K., Springer, Berlin, Heidelberg, 1992: pp. 670–675. https://doi.org/10.1007/978-3-642-84703-5_89.

[157] A.J. Fields, S. Nawathe, S.K. Eswaran, M.G. Jekir, M.F. Adams, P. Papadopoulos, T.M. Keaveny, Vertebral fragility and structural redundancy, J Bone Miner Res 27 (2012) 2152–8. https://doi.org/10.1002/jbmr.1664.

[158] M.F. Adams, H.H. Bayraktar, T.M. Keaveny, P. Papadopoulos, Ultrascalable Implicit Finite Element Analyses in Solid Mechanics with over a Half a Billion Degrees of Freedom, in: Proceedings of the 2004 ACM/IEEE Conference on Supercomputing, IEEE, Pittsburgh, 2004: pp. 34–34. https://doi.org/10.1109/SC.2004.62.

[159] C. Flaig, A Highly Scalable Memory Efficient Multigrid Solver for μ-Finite Element Analyses, Doctoral Thesis, ETH Zürich, 2012. https://doi.org/https://doi.org/10.3929/ethz-a-007613965.

[160] B.H. Thacker, S.W. Doebling, F.M. Hemez, M.C. Anderson, J.E. Pepin, E.A. Rodriguez, Los Alamos National Lab., Concepts of Model Verification and Validation, 2004. https://www.osti.gov/servlets/purl/835920-Yl8Ow3/native/ (accessed March 27, 2025).

[161] L.E. Schwer, An Overview of the ASME V&V-10 Guide for Verification and Validation in Computational Solid Mechanics, in: 20th International Conference on Structural Mechanics in Reactor Technology (SMiRT 20), Espoo, 2009.

https://repository.lib.ncsu.edu/server/api/core/bitstreams/a45e16f4-5cce-44f4-b2bd-fa760019c8aa/content (accessed March 26, 2025).

[162] P. Varga, D.H. Pahr, S. Baumbach, P.K. Zysset, HR-pQCT based FE analysis of the most distal radius section provides an improved prediction of Colles' fracture load in vitro, Bone 47 (2010) 982–988. https://doi.org/10.1016/j.bone.2010.08.002.

[163] M. Palanca, G. Cavazzoni, E. Dall'Ara, The role of bone metastases on the mechanical competence of human vertebrae, Bone 173 (2023) 116814. https://doi.org/10.1016/j.bone.2023.116814.

[164] B.K. Bay, T.S. Smith, D.P. Fyhrie, M. Saad, Digital Volume Correlation: Three-dimensional Strain Mapping Using X-ray Tomography, Exp Mech 39 (1999) 217–226. https://doi.org/10.1007/BF02323555.

[165] B.C. Roberts, E. Perilli, K.J. Reynolds, Application of the digital volume correlation technique for the measurement of displacement and strain fields in bone: A literature review, J Biomech 47 (2014) 923–934. https://doi.org/10.1016/j.jbiomech.2014.01.001.

[166] E. Dall'Ara, M. Peña-Fernández, M. Palanca, M. Giorgi, L. Cristofolini, G. Tozzi, Precision of digital volume correlation approaches for strain analysis in bone imaged with micro-computed tomography at different dimensional levels, Front Mater 4 (2017). https://doi.org/10.3389/fmats.2017.00031.

[167] E. Dall'Ara, G. Tozzi, Digital volume correlation for the characterization of musculoskeletal tissues: Current challenges and future developments, Front Bioeng Biotechnol 10 (2022). https://doi.org/10.3389/fbioe.2022.1010056.

[168] E. Dall'Ara, D. Barber, M. Viceconti, About the inevitable compromise between spatial resolution and accuracy of strain measurement for bone tissue: A 3D zero-strain study, J Biomech 47 (2014) 2956–2963. https://doi.org/10.1016/j.jbiomech.2014.07.019.

[169] M. Palanca, S. Oliviero, E. Dall'Ara, MicroFE models of porcine vertebrae with induced bone focal lesions: Validation of predicted displacements with digital volume correlation, J Mech Behav Biomed Mater 125 (2022). https://doi.org/10.1016/j.jmbbm.2021.104872.

[170] R. Zauel, Y.N. Yeni, B.K. Bay, X.N. Dong, D.P. Fyhrie, Comparison of the linear finite element prediction of deformation and strain of human cancellous bone to 3D digital volume correlation measurements, J Biomech Eng 128 (2006) 1–6. https://doi.org/10.1115/1.2146001.

[171] J. Fu, H. Meng, C. Zhang, Y. Liu, D. Chen, A. Wang, R.P. Main, H. Yang, Effects of tissue heterogeneity on trabecular micromechanics examined by microCT-based finite element analysis and digital volume correlation, Med Nov Technol Devices 11 (2021) 100088. https://doi.org/10.1016/j.medntd.2021.100088.

[172] G. Bevill, T.M. Keaveny, Trabecular bone strength predictions using finite element analysis of micro-scale images at limited spatial resolution, Bone 44 (2009) 579–584. https://doi.org/10.1016/j.bone.2008.11.020.

[173] O.C. Yeh, T.M. Keaveny, Relative roles of microdamage and microfracture in the mechanical behavior of trabecular bone, Journal of Orthopaedic Research 19 (2001) 1001–1007. https://doi.org/10.1016/S0736-0266(01)00053-5.

[174] D.D. Cody, G.J. Gross, F.J. Hou, H.J. Spencer, S.A. Goldstein, D.P. Fyhrie, Femoral strength is better predicted by finite element models than QCT and DXA, J Biomech 32 (1999) 1013–1020. https://doi.org/10.1016/s0021-9290(99)00099-8.

[175] S.K. Boyd, Image-Based Finite Element Analysis, in: C.W. Sensen, B. Hallgrimsson (Eds.), Advanced Imaging in Biology and Medicine: Technology, Software Environments, Applications, Springer Berlin Heidelberg, 2009: pp. 301–318.

[176] R. Müller, Hierarchical microimaging of bone structure and function, Nat Rev Rheumatol 5 (2009) 373–381. https://doi.org/10.1038/nrrheum.2009.107.

[177] E. Verhulp, B. van Rietbergen, R. Müller, R. Huiskes, Micro-finite element simulation

of trabecular-bone post-yield behaviour - Effects of material model, element size and type, Comput Methods Biomech Biomed Engin 11 (2008) 389–395. https://doi.org/10.1080/10255840701848756.

[178] H. Ding, Z.A. Zhu, K.R. Dai, M. Ye, C.T. Wang, Research on damage in trabecular bone of the healthy human acetabulum at small strains using nonlinear micro-finite element analysis, J Shanghai Jiaotong Univ Sci 13 (2008) 623–628. https://doi.org/10.1007/s12204-008-0623-5.

[179] M. Stipsitz, D.H. Pahr, AN EFFICIENT SOLVER FOR LARGE-SCALE SIMULATIONS OF VOXEL-BASED STRUCTURES USING A NONLINEAR DAMAGE MATERIAL MODEL, 2018. https://congress.cimne.com/eccm_ecfd2018/admin/files/filePaper/p1159.pdf (accessed March 26, 2025).

[180] U. Wolfram, H.J. Wilke, P.K. Zysset, Valid μ finite element models of vertebral trabecular bone can be obtained using tissue properties measured with nanoindentation under wet conditions, J Biomech 43 (2010) 1731–1737. https://doi.org/10.1016/j.jbiomech.2010.02.026.

[181] D. Christen, L.J. Melton, A. Zwahlen, S. Amin, S. Khosla, R. Müller, Improved fracture risk assessment based on nonlinear micro-finite element simulations from HRpQCT images at the distal radius, Journal of Bone and Mineral Research 28 (2013) 2601–2608. https://doi.org/10.1002/jbmr.1996.

[182] M.K. Ryan, S. Oliviero, M.C. Costa, J. Mark Wilkinson, E. Dall'ara, Heterogeneous strain distribution in the subchondral bone of human osteoarthritic femoral heads, measured with digital volume correlation, Materials 13 (2020) 1–18. https://doi.org/10.3390/ma13204619.

[183] M. Palanca, G. de Donno, E. Dall'Ara, A novel approach to evaluate the effects of artificial bone focal lesion on the three-dimensional strain distributions within the vertebral body, PLoS One 16 (2021). https://doi.org/10.1371/journal.pone.0251873.

[184] T.M. Jackman, A.M. DelMonaco, E.F. Morgan, Accuracy of finite element analyses of CT scans in predictions of vertebral failure patterns under axial compression and anterior flexion, J Biomech 49 (2016) 267–275. https://doi.org/10.1016/j.jbiomech.2015.12.004.

[185] S. Martelli, M. Giorgi, E. Dall' Ara, E. Perilli, Damage tolerance and toughness of elderly human femora, Acta Biomater 123 (2021) 167–177. https://doi.org/10.1016/j.actbio.2021.01.011.

[186] L. Yan, A. Cinar, S. Ma, R. Abel, U. Hansen, T.J. Marrow, A method for fracture toughness measurement in trabecular bone using computed tomography, image correlation and finite element methods, J Mech Behav Biomed Mater 109 (2020) 103838. https://doi.org/10.1016/j.jmbbm.2020.103838.

[187] K. Madi, G. Tozzi, Q.H. Zhang, J. Tong, A. Cossey, A. Au, D. Hollis, F. Hild, Computation of full-field displacements in a scaffold implant using digital volume correlation and finite element analysis, Med Eng Phys 35 (2013) 1298–1312. https://doi.org/10.1016/j.medengphy.2013.02.001.

[188] M. Peña Fernández, A.H. Barber, G.W. Blunn, G. Tozzi, Optimization of digital volume correlation computation in SR-microCT images of trabecular bone and bone-biomaterial systems, J Microsc 272 (2018) 213–228. https://doi.org/10.1111/jmi.12745.

[189] H.S. Hosseini, M. Horák, P.K. Zysset, M. Jirásek, An over-nonlocal implicit gradient-enhanced damage-plastic model for trabecular bone under large compressive strains, Int J Numer Method Biomed Eng 31 (2015) e02728. https://doi.org/10.1002/cnm.2728.

[190] M. Palanca, G. Tozzi, L. Cristofolini, M. Viceconti, E. Dall'Ara, Three-dimensional local measurements of bone strain and displacement: Comparison of three digital volume correlation approaches, J Biomech Eng 137 (2015) 071006. https://doi.org/10.1115/1.4030174.

[191] J. Kusins, N. Knowles, M. Ryan, E. Dall'Ara, L. Ferreira, Performance of QCT-Derived scapula finite element models in predicting local displacements using digital volume correlation, J Mech Behav Biomed Mater 97 (2019) 339–345. https://doi.org/10.1016/j.jmbbm.2019.05.021.

[192] N.K. Knowles, J. Kusins, M. Faieghi, M. Ryan, E. Dall'Ara, L.M. Ferreira, Material Mapping of QCT-Derived Scapular Models: A Comparison with Micro-CT Loaded Specimens Using Digital Volume Correlation, Ann Biomed Eng 47 (2019) 2188–2198. https://doi.org/10.1007/s10439-019-02312-2.

[193] G. Tozzi, E. Dall'Ara, M. Palanca, M. Curto, F. Innocente, L. Cristofolini, Strain uncertainties from two digital volume correlation approaches in prophylactically augmented vertebrae: Local analysis on bone and cement-bone microstructures, J Mech Behav Biomed Mater 67 (2017) 117–126. https://doi.org/10.1016/j.jmbbm.2016.12.006.

[194] P. Virtanen, R. Gommers, T.E. Oliphant, M. Haberland, T. Reddy, D. Cournapeau, E. Burovski, P. Peterson, W. Weckesser, J. Bright, S.J. van der Walt, M. Brett, J. Wilson, K.J. Millman, N. Mayorov, A.R.J. Nelson, E. Jones, R. Kern, E. Larson, C.J. Carey, İ. Polat, Y. Feng, E.W. Moore, J. VanderPlas, D. Laxalde, J. Perktold, R. Cimrman, I. Henriksen, E.A. Quintero, C.R. Harris, A.M. Archibald, A.H. Ribeiro, F. Pedregosa, P. van Mulbregt, A. Vijaykumar, A. Pietro Bardelli, A. Rothberg, A. Hilboll, A. Kloeckner, A. Scopatz, A. Lee, A. Rokem, C.N. Woods, C. Fulton, C. Masson, C. Häggström, C. Fitzgerald, D.A. Nicholson, D.R. Hagen, D. V. Pasechnik, E. Olivetti, E. Martin, E. Wieser, F. Silva, F. Lenders, F. Wilhelm, G. Young, G.A. Price, G.-L. Ingold, G.E. Allen, G.R. Lee, H. Audren, I. Probst, J.P. Dietrich, J. Silterra, J.T. Webber, J. Slavič, J. Nothman, J. Buchner, J. Kulick, J.L. Schönberger, J.V. de Miranda Cardoso, J. Reimer, J. Harrington, J.L.C. Rodríguez, J. Nunez-Iglesias, J. Kuczynski, K. Tritz, M. Thoma, M. Newville, M. Kümmerer, M. Bolingbroke, M. Tartre, M. Pak, N.J. Smith, N. Nowaczyk, N. Shebanov, O. Pavlyk, P.A. Brodtkorb, P. Lee, R.T. McGibbon, R. Feldbauer, S. Lewis, S. Tygier, S. Sievert, S. Vigna, S. Peterson, S. More, T. Pudlik, T. Oshima, T.J. Pingel, T.P. Robitaille, T. Spura, T.R. Jones, T. Cera, T. Leslie, T. Zito, T. Krauss, U. Upadhyay, Y.O. Halchenko, Y. Vázquez-Baeza, SciPy 1.0: fundamental algorithms for scientific computing in Python, Nat Methods 17 (2020) 261–272. https://doi.org/10.1038/s41592-019-0686-2.

[195] G. Tozzi, V. Danesi, M. Palanca, L. Cristofolini, Elastic Full-Field Strain Analysis and Microdamage Progression in the Vertebral Body from Digital Volume Correlation, Strain 52 (2016) 446–455. https://doi.org/10.1111/str.12202.

[196] L. Liu, E.F. Morgan, Accuracy and precision of digital volume correlation in quantifying displacements and strains in trabecular bone, J Biomech 40 (2007) 3516–3520. https://doi.org/10.1016/j.jbiomech.2007.04.019.

[197] M. Palanca, A.J. Bodey, M. Giorgi, M. Viceconti, D. Lacroix, L. Cristofolini, E. Dall'Ara, Local displacement and strain uncertainties in different bone types by digital volume correlation of synchrotron microtomograms, J Biomech 58 (2017) 27–36. https://doi.org/10.1016/j.jbiomech.2017.04.007.

[198] H.D. Barth, M.E. Launey, A.A. MacDowell, J.W. Ager, R.O. Ritchie, On the effect of X-ray irradiation on the deformation and fracture behavior of human cortical bone, Bone 46 (2010) 1475–1485. https://doi.org/10.1016/j.bone.2010.02.025.

[199] H.D. Barth, E.A. Zimmermann, E. Schaible, S.Y. Tang, T. Alliston, R.O. Ritchie, Characterization of the effects of x-ray irradiation on the hierarchical structure and mechanical properties of human cortical bone, Biomaterials 32 (2011) 8892–8904. https://doi.org/10.1016/j.biomaterials.2011.08.013.

[200] A. Singhal, A.C. Deymier-Black, J.D. Almer, D.C. Dunand, Effect of high-energy X-ray doses on bone elastic properties and residual strains, J Mech Behav Biomed Mater 4 (2011) 1774–1786. https://doi.org/10.1016/j.jmbbm.2011.05.035.

[201] R.L. Taylor, FEAP - Finite Element Analysis Program, University of California, Berkeley, 2014.

[202] H.S. Hosseini, A. Dünki, J. Fabech, M. Stauber, N. Vilayphiou, D. Pahr, M. Pretterklieber, J. Wandel, B. van Rietbergen, P.K. Zysset, Fast estimation of Colles' fracture load of the distal section of the radius by homogenized finite element analysis based on HR-pQCT, Bone 97 (2017) 65–75. https://doi.org/10.1016/j.bone.2017.01.003.

[203] P. Akhlaghi, S. Khorshidparast, G. Rouhi, Investigation on primary stability of dental implants through considering peri-implant bone damage, caused by small and large deformations: A validated non-linear micro finite element study, J Mech Behav Biomed Mater 146 (2023) 106062. https://doi.org/10.1016/j.jmbbm.2023.106062.

[204] P. Stefanek, D.H. Pahr, A. Synek, Comparison of simplified bone-screw interface models in materially nonlinear μFE simulations, J Mech Behav Biomed Mater 157 (2024) 106634. https://doi.org/10.1016/j.jmbbm.2024.106634.

[205] E.F. Morgan, T.M. Keaveny, Dependence of yield strain of human trabecular bone on anatomic site, J Biomech 34 (2001) 569–577. https://doi.org/10.1016/S0021-9290(01)00011-2.

[206] A.I. Hussein, P.E. Barbone, E.F. Morgan, Digital volume correlation for study of the mechanics of whole bones, in: Procedia IUTAM, 2012: pp. 116–125. https://doi.org/10.1016/j.piutam.2012.05.013.

[207] M. Peña Fernández, A.P. Kao, F. Witte, H. Arora, G. Tozzi, Low-cycle full-field residual strains in cortical bone and their influence on tissue fracture evaluated via in situ stepwise and continuous X-ray computed tomography, J Biomech 113 (2020) 110105. https://doi.org/10.1016/j.jbiomech.2020.110105.

[208] M. Peña Fernández, A.P. Kao, R. Bonithon, D. Howells, A.J. Bodey, K. Wanelik, F. Witte, R. Johnston, H. Arora, G. Tozzi, Time-resolved in situ synchrotron-microCT: 4D deformation of bone and bone analogues using digital volume correlation, Acta Biomater 131 (2021) 424–439. https://doi.org/10.1016/j.actbio.2021.06.014.

[209] F. Xu, Quantitative characterization of deformation and damage process by digital volume correlation: A review, Theoretical and Applied Mechanics Letters 8 (2018) 83–96. https://doi.org/10.1016/j.taml.2018.02.004.

[210] D.B. Burr, C.H. Turner, P. Naick, M.R. Forwood, W. Ambrosius, M. Sayeed Hasan, R. Pidaparti, Does microdamage accumulation affect the mechanical properties of bone?, J Biomech 31 (1998) 337–345. https://doi.org/10.1016/S0021-9290(98)00016-5.

[211] T.C. Lee, S. Mohsin, D. Taylor, R. Parkesh, T. Gunnlaugsson, F.J. O'Brien, M. Giehl, W. Gowin, Detecting microdamage in bone, J Anat 203 (2003) 161–172. https://doi.org/10.1046/j.1469-7580.2003.00211.x.

[212] P. Stefanek, A. Synek, E. Dall'Ara, D.H. Pahr, Comparison of linear and nonlinear stepwise μFE displacement predictions to digital volume correlation measurements of trabecular bone biopsies, J Mech Behav Biomed Mater 138 (2023) 105631. https://doi.org/10.1016/j.jmbbm.2022.105631.

[213] P. Stefanek, J.D. Silva-Henao, V. Fiedler, A.G. Reisinger, D.H. Pahr, A. Synek, Screw pull-out force predictions in porcine radii using efficient nonlinear μFE models including contact and pre-damage, Front Bioeng Biotechnol 13 (2025). https://doi.org/10.3389/fbioe.2025.1524235.